UNIVERSIDADE DE LISBOA

FACULDADE DE CIÊNCIAS

DEPARTAMENTO DE FÍSICA

Dark Matter, Gravitational Waves and Higgs invisible decays

João Francisco de Veloso e Viana

Mestrado em Física

Especialização em Física Nuclear e Partículas

Dissertação orientada por:

Prof. Dr. Rui Alberto Serra Ribeiro dos Santos

2021

Acknowledgements

Gostava de agradecer ao professor Rui Santos pela ajuda, paciência e compreensão ao longo dos nossos projetos.

Gostava de agradecer à minha familia pela educação e apoio que me deram ao longo da minha existência.

Gostava de agradecer aos meus pais e ao meu irmão pelas maiores amizades que eu tenho.

Gostava de agradecer aos meus cães (Jara e Nero) e papagaio (Einstein) pela melhor companhia que alguém pode ter.

Gostava de agradecer à Maria pelo amor, carinho e paciência que preciso.

Resumo

O Modelo Padrão, apesar de ser uma das teorias mais bem verificadas experimentalmente no mundo da física, tem as sua limitações. Um grande problema que o Modelo Padrão enfrenta é o facto de não dar qualquer explicação para a existência de matéria escura, comprovada apenas por observações provenientes da astronomia e da cosmologia. Por estas razões, propomos uma extensão simples do Modelo Padrão: adicionar um campo complexo escalar que acopla apenas com o dubleto de Higgs. De seguida fazemos a renormalização do setor escalar, usando condições *on-shell* e *process dependent*, calculamos a correção a um loop do decaimento do Higgs para matéria escura e verificamos que a correção é estável. De seguida fazemos uma procura no espaço de parâmetros do modelo para verificar quais os parâmetros que verificam os mais relevantes constrangimentos teóricos e experimentais. A comparação com o valor medido experimentalmente no Large Hadron Collider dá-nos informação sobre o sector escuro do modelo. A adição do campo complexo tem outra vantagem, a de permitir a existência de uma transição electro-fraca de primeira ordem (algo que não é possível no Modelo Padrão). Esta transição poderá dar origem a ondas gravitacionais primordiais que poderão ser detetadas em experiências futuras, tal como LISA. Verificámos que é possível, por extensão do modelo, obter ondas gravitacionais fortes o suficientes para serem detetadas e que existe também uma dependência no valor dos parâmetros do Modelo Padrão, em particular na massa do Higgs do quark top. Verificámos também uma forte dependência nos parâmetros do setor escuro e, por fim, que a configuração do vácuo a temperatura zero afeta a força do sinal das ondas gravitacionais.

Palavras Chave: Extensão do modelo padrão, renormalização, correções a 1-loop, ondas gravitationais primordiais, LISA.

Abstract

It is well known that, although the Standard Model of particle physics can make many accurate predictions about the physical world around us, it is still incomplete in many regards. One of the most noticeable areas where the Standard Model fails us to give some reasonable explanation is the absence of dark matter, that one can infer from astronomy/cosmology. For that reason, we propose a simple model: a complex scalar extension of the Standard Model, where the new field only couples with the Higgs doublet. We then renormalize the scalar sector, using on-shell renormalization conditions and process dependent conditions to calculate the 1-loop correction of the Higgs decay into dark matter. We have verified that the corrections are stable. After that, we performed scans to find the allowed parameter space that fulfils not only theoretical constraints but also the most relevant experimental ones. We have then compared with the experimentally measured value at the Large Hadron Collider to have access to the dark sector of the theory. The addition of the complex scalar field has another advantage. It allows for a first-order electroweak phase transition (which is not possible in the Standard Model) that could produce gravitational waves that could be detected in upcoming experiments, such as LISA. We see that strong enough gravitational waves are indeed possible. We have also verified their dependence on the Standard Model parameters inside their experimental uncertainty, in particular the Higgs and top quark mass, which can be important. We have also showed that the dark sector parameters play a huge role in the gravitational wave profile and, lastly, verify that the vacuum configuration at zero temperature affects the strength of gravitational waves.

Keywords: Standard model extension, renormalization, 1-loop corrections, primordial gravitational waves, LISA

Resumo Alargado

Esta tese está dividida em dois temas distintos relacionados pelo mesmo modelo de física. O modelo é a extensão do Modelo Padrão por um campo escalar complexo com todos os números quânticos iguais a zero (CxSM). O novo campo acopla apenas com o dubleto de Higgs e, por isso, apenas o setor escalar do Modelo Padrão vai ser alterado. Este novo campo pode ou não ganhar um valor de expectação do vácuo (VEV). Caso o VEV seja zero, estaremos no cenário em que há duas partículas de matéria escura com massas distintas que interagem com o Modelo Padrão apenas através da partícula de Higgs. Caso o VEV seja real e diferente de zero (podemos sempre tornar o VEV real multiplicando o campo por uma fase por isso não há perda de generalidade) passamos a ter uma mistura entre a componente real do novo campo e a partícula de Higgs do Modelo Padrão, neste cenário a componente imaginária irá ser a partícula de matéria escura.

Na primeira parte da tese vamos tratar da renormalização do setor escalar da extensão complexa com VEV escalar não nulo. O nosso objetivo é calcular a correção em segunda ordem (1-loop) ao decaimento do Higgs para duas partículas de matéria escura. Esta correção não pode apenas ser retirada a partir dos diagramas de segunda ordem porque irão aparecer divergências provenientes da integração do momento interno. Para renormalizar o decaimento vamos supor que todos os campos e parâmetros são promovidos a *bare* que são a soma das componentes renormalizadas e dos contra-termos. O objetivo da renormalização é encontrar os contra-termos tais que a correção a 1-loop seja finita. Para isso vamos utilizar o chamado esquema de renormalização *on-shell* que consiste em impor que o propagador renormalizado verifique as mesmas condições que o propagador a nível árvore. Este esquema não é suficiente para determinar todos os contra termos e por isso utilizamos o esquema de tadpoles Fleischer e Jegerlehner para assegurar que não há termos lineares nos campos no Lagrangiano, o que valida a utilização de teoria de perturbações. Usando o esquema de Kanemura *et. al* para o contra-termo do ângulo de mistura e o esquema de renormalização com processo auxiliar para o VEV escalar podemos encontrar os contra termos restantes e assim calcular a correção a 1-loop. Dadas as circunstâncias, temos a liberdade de escolher entre quatro esquemas de renormalização. Dois são provenientes do contra termo do ângulo, que pode ser definido on-shell ou então na média dos quadrados das massas. Os outros dois são proveniente do contra termo do VEV, que pode ser calculado *on-shell* ou na aproximação de momento externo igual a zero (ZEM) (este último troca um pouco da estabilidade da renormalização por um maior espaço disponível de parâmetros de massas). A conclusão geral é que este procedimento de renormalização é extremamente estável (isto é, a correção é pequena comparada com o valor de primeira ordem) com a correção sempre menor que 10% do valor a primeira ordem, excepto no caso dos pontos que estão abaixo de *threshold* de massa que nos permite usar o esquema *on-shell*. Nesse caso apenas o método ZEM pode ser usado e a correção pode chegar até aos 50% mas apenas no caso em que a largura em primeira ordem seja próxima de zero. Uma conclusão curiosa é que as condições experimentais de matéria escura tornam o ângulo de mistura igual a zero extremamente indesejável. Esse constrangimento está relacionado com o valor experimental da densidade de relíquia.

Na segunda parte da tese vamos falar sobre ondas gravitacionais criadas a partir de ondas de choque induzidas por uma forte transição de fase electrofraca, algo que não é verificado no Modelo Padrão e é visto como umas das condições necessárias para a bariogénese (condições de Sakharov). A transição de fase acontece porque, à medida que o Universo arrefece com a expansão, o potencial do modelo irá alterar a sua forma que poderá dar origem a múltiplos mínimos locais. É possível que num dado momento nos encontremos num mínimo que deixe de ser energeticamente vantajoso e que leve o Universo a transitar, por tunelamento quântico, para outro mínimo. Esta transição, se for brusca o suficiente, irá dar origem a fontes de ondas gravitacionais tais como ondas de som, colisão de bolhas de vácuo ou turbulência. Nesta tese, apenas vamos tomar em conta as ondas gravitacionais com origem em ondas de som. Se a transição de fase for rápida o suficiente e houver muita libertação de energia, as ondas gravitacionais podem ser fortes o suficiente para serem detetadas em experiências futuras, tais como LISA, DECIGO ou BBO. As ondas gravitacionais dependem fortemente do modelo físico em questão e dos parâmetros do potencial a temperatura zero. O nosso objetivo é saber se a variação do valor dos parâmetros do Modelo Padrão, dentro da sua incerteza experimental, gera algum impacto no perfil de ondas gravitacionais. Concluímos que de facto há uma forte dependência na massa do Higgs mas também embora mais fraca na massa do quark top. Verificámos também que há uma forte dependência nos parâmetros do setor escuro, como seria de esperar. A existência ou não de ondas gravitacionais intensas é também dependente da configuração do vácuo a temperatura zero.

Verificámos que, tanto no caso em que temos duas partículas de matéria escura (VEV escalar zero) como no caso em que temos apenas uma (VEV escalar não zero) e em que há mistura entre o Higgs e a parte real não há ondas gravitacionais detetáveis em LISA. No entanto, os pontos do caso com VEV escalar não zero parecem produzir ondas gravitacionais com sinais muito mais fortes que o caso do VEV escalar zero, e por isso não é descartada a hipótese de serem encontrados pontos no futuro. Curiosamente, se adicionarmos neutrinos de quiralidade direita num mecanismo de *inverse seesaw* encontramos ondas gravitacionais detetáveis por LISA. Por haver uma ligeira instabilidade numérica no cálculo do β/H (o inverso do tempo da transição de fase dividido pela constante de Hubble), criámos um método que nos permite suavizar a ação num dado intervalo e usar essa interpolação para calcular não só o β/H mas também as temperaturas de nucleação e percolação com grande precisão. Ao aplicar este método da interpolação a quatro amostras de pontos temos uma noção da incerteza associada ao nosso método.

Contents

1 **Introduction** **1**

2 **Complex Singlet Extension** **3**

2.1 Motivation . . . 3
2.2 Scalar Potential . . . 4
2.2.1 Zero Scalar VEV $v_\sigma = 0$ . . . 5
2.2.2 Non-Zero Scalar VEV $v_\sigma \neq 0$ . . . 6
2.3 Scalar Lagrangian . . . 8
2.4 Lagrangian . . . 9
2.4.1 Gauge Lagrangian . . . 9
2.4.2 Fermionic Lagrangian . . . 9
2.4.3 Yukawa Lagrangian . . . 11
2.4.4 Gauge Fixing Lagrangian . . . 11
2.4.5 Ghost Lagrangian . . . 12

3 **Renormalization** **15**

3.1 Introduction . . . 15
3.2 Leading Order Amplitude . . . 16
3.3 Next-to-leading Order Amplitude . . . 16
3.4 Decay Width . . . 18
3.5 Regularization . . . 18
3.6 Renormalization . . . 21
3.7 On-shell Renormalization . . . 22
3.7.1 Single Field . . . 24
3.7.2 Two Mixing Fields . . . 25
3.8 Fleischer-Jegerlehner Tadpole Scheme . . . 26
3.9 Leg Corrections and Leg counterterms . . . 31
3.10 Renormalization of α in the KOSY Scheme . . . 32
3.11 Renormalization of v_σ scalar VEV . . . 35

4 Results and Discussion 39
4.1 Decay widths of $h_1 \to \sigma_I \sigma_I$ at NLO 39
4.2 Conclusions on the NLO corrections to Higgs Invisible Width 46

5 Primordial Gravitational Waves 47
5.1 Introduction 47
5.2 Scenarios 48
5.3 Finite Temperature Potential 49
5.4 Gravitational Waves from FOPT 51
5.5 Analysis of Scenario 1 55
5.6 Analysis of Scenario 2 56
  5.6.1 Gravitational Waves Detection 56
  5.6.2 The dependence on the SM parameters 59
5.7 Signal-to-Noise Ratio 63
5.8 Conclusions on Gravitational Waves 65

A Pinch technique 67
A.1 Squares 71
A.2 External Legs 72
A.3 Triangles 72
A.4 Additional Diagrams - from $\xi_i = 1$ part of the propagators 74
A.5 Pinched self-energy 75

B Right-Handed Neutrinos 77

C Smoothing the action 79

References 81

List of Figures

3.1 Leading order amplitude $i\mathcal{A}^{\text{LO}}_{h_1\sigma_I\sigma_I}$ of the Higgs decay into dark matter particles. 16

3.2 1-loop corrections to the leading order amplitude. $\mathcal{A}^{\text{VC}}$ is vertex correction, $\mathcal{A}^{\text{CT}}$ is the vertex counterterm, $\mathcal{A}^{\text{leg},i}$ is the leg correction for the leg i and $\mathcal{A}^{\text{leg CT},i}$ is the vertex counterterm for the leg i. The gray circles indicates the 1-loop corrections while the crossed circles indicate diagrams coming from the counterterm Lagrangian. 17

3.3 Example of a tadpole diagram that contains divergences. This contribution belongs to the $\mathcal{A}^{\text{VC}}$ diagrams in Fig. 3.2 19

3.4 One-particle irreducible diagrams, also called self-energies. Set of diagrams that cannot be split into two by cutting an internal line. Although the self-energies are defined to all order of perturbation theory we only show, and use in our calculations, up to the leading order contribution. 23

3.5 Self-energies for two mixing fields. In the case for mixing fields the incoming particle and outgoing particle is not always the same. 25

3.6 One-particle irreducible diagrams, also called self-energies. On this definition of self-energy we include the tadpoles. 30

4.1 Scatter plot of the dark particle mass m_{σ_I} compared to the seconds Higgs mass m_{h_2}. In blue are the points above mass threshold and in orange are the point below mass threshold. 41

4.2 Left: histogram for the mixing angle α. Right: histogram of $h^2\Omega_{cdm}$ 41

4.3 Scatter plot of the scalar VEV v_σ as a function of mixing angle α. Scatter plot of the scalar VEV v_σ as a function of the DM particle mass m_{σ_I}. 42

4.4 Plot of the next-to-leading order amplitude Γ^{NLO} as a function of Γ^{LO}. The different colours identify the different renormalization schemes that we can chose. 42

4.5 Relative difference of the next to leading order decay width. The different colours identify the different renormalization schemes that we can chose. The marker × identifies point below the mass threshold, with $m_{h_2} < 2m_{\sigma_I}$, and therefore can only be calculated using the ZEM scheme. The marker • identifies any other point. 43

4.6 Relative difference of the next to leading order decay width for point below the mass threshold, $m_{h_2} < 2m_{\sigma_I}$. The two different colour identify the possible renormalization scheme for $\delta\alpha$. 44

4.7 Relative difference of the width as a function of m_{h_2} (left) and as a function of DM particle mass m_{σ_I} (right). We started with a point, that verified all theoretical and experimental constraints, and varied the mass m_{h_2} in the interval [30, 1000] GeV (left) and varied the DM particle mass m_{σ_I} in the interval [10, 62.55] GeV. 45

4.8 Relative difference of the width as a function of the mixing angle α (left) and as a function of v_σ (right). We started with a point, that verified all theoretical and experimental, constraints and varied α in the interval $\left[-\frac{\pi}{2}, \frac{\pi}{2}\right]$ (left) and v_σ in the interval [10, 1000] GeV (right). 45

4.9 Branching ratio for $h_1 \to \sigma_I \sigma_I$ at NLO as a function of the one at LO for the four renormalization schemes. 46

5.1 The peak-amplitude of the GW signal $h^2\Omega_{\mathrm{GW}}^{\mathrm{peak}}$ as a function of the peak frequency f_{peak} in logarithmic scale for scenario 1 in both vacuum configurations, the left panel corresponds to the zero scalar VEV v_σ while the right panel is the non-zero scalar VEV v_σ. The colour bar indicates the strength of the phase transition α. The PISCs for LISA BBO and DECIGO are represented with dashed, dot-dashed and dotted lines respectively. 56

5.2 The peak-amplitude of the GW signal $h^2\Omega_{\mathrm{GW}}^{\mathrm{peak}}$ as a function of the peak frequency f_{peak} in logarithmic scale. The colour bar indicates the strength of the phase transition α (left panel) and the inverse time-scale of the phase transition in units of the Hubble parameter H, β/H (right panel). The PISCs for LISA BBO and DECIGO are represented with dashed, dot-dashed and dotted lines respectively. 57

5.3 Peak-amplitude of the GW signal $h^2\Omega_{\mathrm{GW}}^{\mathrm{peak}}$ as a function of the peak frequency f_{peak} in logarithmic scale. The scatter plots present, in the colour bar, $\Delta v_h/T_*$ (left panel) and $\Delta v_\sigma/T_*$ (right panel). 58

5.4 Scatter plot showing $\Delta v_h/T_*$ vs. $\Delta v_\sigma/T_*$ with the strength of the GW signal $h^2\Omega_{\mathrm{GW}}^{\mathrm{peak}}$ given by the colour bar. 58

5.5 The peak-amplitude of the GW signal $h^2\Omega_{\mathrm{GW}}^{\mathrm{peak}}$ as a function of the peak frequency f_{peak} in logarithmic scale. The colour bar indicates the difference between the nucleation temperature and percolation temperature in GeV. The PISCs for LISA BBO and DECIGO are represented with dashed, dot-dashed and dotted lines respectively. 59

5.6 The dependence of $h^2\Omega_{\mathrm{GW}}^{\mathrm{peak}}$ on the peak-frequency f_{peak} and the Higgs boson mass m_{h_1} for fixed dark sector parameters, $m_{h_2} = 994.0$ GeV, $m_{\sigma_I} = 599.9$ GeV, $v_\sigma = 275.6$ GeV, $\alpha = -0.52$, $M_\nu = 254.1$ GeV and $\tilde{\mu} = 3.0$ is shown on the left panel, since the variation is very small we show a zoomed in version in the right panel. The chosen original FOPT (before parameters' variation) is characterised by $T_c = 80.7$ GeV, $T_n = 57.5$ GeV, $T_* = 54.2$ GeV, $\left(v_h^i, v_\sigma^i\right) \to \left(v_h^f, v_\sigma^f\right) = (0.0, 185.3) \to (236.2, 269.4)$, $\alpha = 0.26$, $\beta/H = 253$, $\Delta v_h/T_* = 4.4$ and $\Delta v_\sigma/T_* = 1.6$. The Higgs mass is varied within the experimental uncertainty, i.e. between 124.96 GeV and 125.24 GeV. The remaining SM parameters are fixed to their central values. Only the points for which a FOPT took place are shown. 60

5.7 The dependence of $h^2\Omega_{\text{GW}}^{\text{peak}}$ on the peak-frequency f_{peak} and the Higgs mass m_{h_1}. The Higgs mass is varied by 1σ around the central value keeping all other parameters fixed. In the left plot, the original (before variation of any parameters) phase transition was found for the central values of the SM parameters and for the fixed parameters of the dark sector: $m_{h_2} = 994.0$ GeV, $m_{\sigma_I} = 599.9$ GeV, $v_\sigma = 275.6$ GeV, $\alpha = -0.52$, $M_\nu = 254.1$ GeV and $\tilde{\mu} = 3.0$. The original FOPT is characterised by $T_c = 80.7$ GeV, $T_n = 57.5$ GeV, $T_* = 54.2$ GeV, $\left(v_h^i, v_\sigma^i\right) \to \left(v_h^f, v_\sigma^f\right) = (0.0, 185.3) \to (236.2, 269.4)$, $\alpha = 0.26$, $\beta/H = 253$, $\Delta v_h/T_* = 4.4$ and $\Delta v_\sigma/T_* = 1.6$. In the right plot, the same quantities is shown but for $m_{h_2} = 955.3$ GeV, $m_{\sigma_I} = 858,6$ GeV, $v_\sigma = 267.1$ GeV, $\alpha = 0.11$, $M_\nu = 198.3$ GeV and $\tilde{\mu} = 0.03$ yielding the original FOPT characterised by $T_c = 103.0$ GeV, $T_n = 71.6$ GeV, $T_* = 67.1$ GeV, $\left(v_h^i, v_\sigma^i\right) \to \left(v_h^f, v_\sigma^f\right) = (0.0, 170.7) \to (239.8, 263.3)$, $\alpha = 0.11$, $\beta/H = 202$, $\Delta v_h/T_* = 3.6$ and $\Delta v_\sigma/T_* = 1.4$. 61

5.8 The dependence of $h^2\Omega_{\text{GW}}^{\text{peak}}$ on the peak-frequency f_{peak} and the top quark mass m_t. The top quark mass is varied by 1σ around the central value keeping all other parameters fixed. In the left plot, the original (before parameters' variation) phase transition was found for the central values of the SM parameters and for the fixed parameters of the dark sector: $m_{h_2} = 994.0$ GeV, $m_{\sigma_I} = 599.9$ GeV, $v_\sigma = 275.6$ GeV, $\alpha = -0.52$, $M_\nu = 254.1$ GeV and $\tilde{\mu} = 3.0$. The original FOPT is characterised by $T_c = 80.7$ GeV, $T_n = 57.5$ GeV, $T_* = 54.2$ GeV, $\left(v_h^i, v_\sigma^i\right) \to \left(v_h^f, v_\sigma^f\right) = (0.0, 185.3) \to (236.2, 269.4)$, $\alpha = 0.26$, $\beta/H = 253$, $\Delta v_h/T_* = 4.4$ and $\Delta v_\sigma/T_* = 1.6$. In the right plot, the same quantities is shown but for $m_{h_2} = 955.3$ GeV, $m_{\sigma_I} = 858,6$ GeV, $v_\sigma = 267.1$ GeV, $\alpha = 0.11$, $M_\nu = 198.3$ GeV and $\tilde{\mu} = 0.03$ yielding the original FOPT characterised by $T_c = 103.0$ GeV, $T_n = 71.6$ GeV, $T_* = 67.1$ GeV, $\left(v_h^i, v_\sigma^i\right) \to \left(v_h^f, v_\sigma^f\right) = (0.0, 170.7) \to (239.8, 263.3)$, $\alpha = 0.11$, $\beta/H = 202$, $\Delta v_h/T_* = 3.6$ and $\Delta v_\sigma/T_* = 1.4$. 62

5.9 Scatter plots showing the strength of the phase transitions $\Delta v_h/T_*$ in the colour scale for scenario 1 with zero scalar VEV v_σ. On the left panel we show the position of the GW peak as a function of the peak frequency while, on the right, we show the corresponding SNR for a mission profile of three years. The colored lines show the SNR that depends on T_*, $g_*(T_*)$ and v_{b}. The dotted curves are contour lines representing the shock formation time τ_{sh} as defined in (5.34). The grey shaded region corresponds to an acoustic period lasting longer than a Hubble time and it is where the sound waves treatment is most reliable. 63

5.10 Scatter plots showing the typical strength of the phase transitions $\Delta v_h/T_*$ and SNR for scenario 1 with non-zero scalar VEV v_σ. 64

5.11 Scatter plots showing the typical strength of the phase transitions $\Delta v_h/T_*$ and SNR for scenario 2. 65

A.1 Set of diagrams that contribute to the general $h_i \to h_j$ self-energy, in the Fleischer and Jegerlehner tadpole scheme. 68

A.2 Triangle diagrams with pinch contributions initially not proportional to λ_i (that can be restored later by the B_0 function). 74

C.1 The peak-amplitude for the GW signal $h^2\Omega_{\mathrm{GW}}^{\mathrm{peak}}$ as a function of the peak frequency f_{peak} in logarithmic scale. The scatter plots present, in the colour bar, the strength of the phase transition α. In the left plot, there are no restrictions related to the calculation of β/H, in the middle plot only points with $\Delta(\beta/H) < 0.25$ are accepted, and in the right panel only points with $\Delta(\beta/H) < 0.1$ are accepted. 80

List of Tables

2.1 Quantum numbers of the SM fermions. 11

4.1 The four possible choices of renormalization schemes: two for the δv_σ and two for $\delta\alpha$. . 39
4.2 Experimental values for the Higgs VEV v_h and particle masses of the SM. Due to their low mass we neglected the contribution of light quarks and light fermions. This set of experimental values is complete in the sense that one can derive the electric coupling, the $SU(2)_L$ coupling, Weinberg angle, etc, can be extrapolated from them using the expressions found in section 2.3. 40
4.3 Allowed parameter space of the model in the $m_{\sigma_I} - \quad m_{h_2}$ plane. In the left panel $m_{h_1} < m_{h_2}$ and in the right panel $m_{h_1} > m_{h_2}$. The upper bound of m_{σ_I} is 62.55 GeV because is required that $m_{h_1} > 2m_{\sigma_I}$ for the process $h_1 \to \sigma_I\sigma_I$ to be kinetimatically allowed. 40
4.4 Input values for the parameters the point used to scan the dependence of each parameter on the NLO decay width. 44

A.1 Pinch contributions from the square diagrams with Z bosons and η goldstone. 71
A.2 Pinch contributions from the square diagrams with W bosons and G goldstone. 71
A.3 Pinch contributions from the leg diagrams with Z bosons and η goldstone. 72
A.4 Pinch contributions from the leg diagrams with W bosons and G goldstone. 72
A.5 Pinch contributions from the triangle diagrams with Z bosons and η goldstone. 73
A.6 Pinch contributions from the triangle diagrams with W bosons and G goldstone. 74

Abbreviations

1-loop	One loop
1PI	One Particle Irreducible
2HDM	Two Higgs Doublet Model
BSM	Beyound Standard Model
CKM	Cabibbo–Kobayashi–Maskawa Matrix
CM	Centre of Mass
$\mathcal{CP}$	Charge-Parity Conjugatation
CT	Counter Term
CxSM	Complex Scalar Extension of the Standard Model
DM	Dark Matter
DQM	Difference Quotient Method
EW	Electroweak
EWPT	Electroweak Phase Transition
FCNC	Flavour Changing Neutral Currents
FJTS	Fleischer-Jegerlehner Tadpole Scheme
FOPT	First Order Phase Transition
FTQFT	Finite Temperature Quantum Field Theory
GW	Gravitational Wave
h.c.	Hermitian Conjugate
KOSY	Kanemura, Okada, Senaha and Yuan
LISA	Laser Interferometer Space Antenna
LO	Leading Order
$\overline{\textbf{MS}}$	Modified Minimal Subtraction
NLO	Next to Leading Order
OS	On-shell
PDG	Particle Data Group
PISC	Peak Integrated Sensitivity Curves
PV	Passarino-Veltmann
SM	Standard Model
SNR	Signal-to-noise ratio
SW	Shock Waves/Sound Waves
VC	Vertex Correction
VEV	Vacuum Expectation Value
ZEM	Zero External Momentum

Chapter 1

Introduction

The Standard Model (SM) of particle physics has been very successful at describing most of the experimental data but, like all models in physics, it has its limitations and there are many physical phenomena for which the SM provides no explanation. One of the unexplained phenomena is the mass of neutrinos. The SM predicts that neutrinos are massless particles but we know that they oscillate between three flavours (electron, muon and tau) [1, 2]. That fact indicates that neutrinos have mass and it is even possible to measure their mass squared differences $m_{\nu_i}^2 - m_{\nu_j}^2 \; (i, j = e, \mu, \tau)$ (see [3] for up-to-date values of these measurements). Although neutrino mass differences are now established and measured, the actual masses and the hierarchy between them is still an open question [3]. The SM also fails to explain why there is more matter than antimatter in the Universe. The conditions for baryogenesis were put forward by Sakharov [4] and comprise Baryon number violation, C-symmetry and CP-symmetry violation and the existence of an epoch where interactions were out of thermal equilibrium, during the early history of the Universe. A strong candidate for such a transition is the electroweak (EW) epoch and, for this reason, it is highly preferred that a strong first-order phase transition (FOPH) should have occurred during the EW transition epoch. It is known that the SM does not provide enough CP-violation and also that it fails to give us that type of transition [5].

Another missing ingredient of the SM is dark matter. DM particles are stable or at least they live longer than the age of the Universe and interact very weakly with the SM particles. It started to be the mysterious particle(s) that causes the increased gravity pull seen on the rotation curves of galaxies, i.e. the angular velocity is higher than predicted farther from the centre of the galaxy which indicates that there is matter missing [6, 7] according to classical mechanics. Another example is the bullet cluster [8], where two clusters of galaxies collided and it was possible to determine, with gravitational lensing, that the centre of the gravity pull is at the centre of the matter which did not interact in the collision and not at the centre of the visible matter. This indicates that dark matter is influenced by gravity but couples very weakly with visible matter. A review on the other astronomical evidence of DM can be found in [9] .

In this work, we propose a BSM (Beyond Standard Model) model which solves one of this issues by including a dark matter candidate. We will build an extension of the SM where one complex scalar field is added to the SM field content that only couples with the the Higgs field. We start with a detailed description of the model and of the renormalization scheme used. We then use it to calculate the decay width of the Higgs particle into two dark matter particles. The most relevant and up-to-date theoretical and experimental constraints are applied to select the points used to calculate the decay width. The results are finally compared with the present experimental values.

Adding a complex scalar field to the theory has another benefit, it allows for a first-order phase transition (FOPT) to occur during the electroweak epoch, one of the Sakharov conditions for baryogenesis [4]. Under certain conditions, the EWFOPT can produce primordial gravitational waves, from sound waves (SW), strong enough to be detected in upcoming spatial interferometers such as LISA [10], DECIGO [11] or BBO [12]. Our goal is to explore the parameter space of the model to see if strong enough GWs are indeed possible and understand the impact of the SM parameters on the GW profile and strength.

Chapter 2

Complex Singlet Extension

2.1 Motivation

The SM is invariant under gauge transformations of the group $SU(2)_L \times U(1)_Y \times SU(3)_C$, where the subscript L indicates that only left-handed fields have non-zero weak isospin (denoted by T), Y is the hypercharge and C is the colour symmetry of quarks[1]. We are going to add a new complex scalar field σ that only couples to the Higgs doublet Φ, which is a spin zero field with hypercharge and weak isospin equal to zero

$$T_\sigma = 0 \quad \text{and} \quad Y_\sigma = 0\,, \tag{2.1}$$

where T_σ and Y_σ are the $SU(2)_L$ and $U(1)_Y$ quantum number of σ, respectively. This ρ parameter is defined as the ratio

$$\rho \equiv \frac{m_W^2}{m_Z^2 c_w^2} = \frac{\sum_{i=1}^{n} v_i \left[4T_i\left(T_i+1\right) - Y_i^2\right]}{\sum_{i=1}^{n} 2Y_i^2 v_i}\,, \tag{2.2}$$

where m_W is the W bosons mass, m_Z is the Z boson mass and c_w is the cosine of the Weinberg angle, and where the last equality is the expression for a generic n scalar extension of the SM, see Ref.[13]. The ρ parameter has a very precise measured value [7]

$$\rho_{\text{exp}} = 1.00038 \pm 0.00020\,, \tag{2.3}$$

which is in agreement with our model since we have the same ρ parameter as the SM, which at tree-level is

$$\rho_{\text{CxSM}} = \rho_{\text{SM}} = 1\,, \tag{2.4}$$

in both models. The same is true for any extensions with only doublets and singlets.

---

[1] Colour will be omitted from now on because it will not relevant for the calculations.

2.2 Scalar Potential

The scalar potential of the theory is composed of the scalar particle, introduced in the previous section, and the usual Higgs doublet Φ also present in the SM. The doublet has quantum numbers:

$$Y_\Phi = \frac{1}{2} \quad \text{and} \quad T_\Phi = \frac{1}{2} \, . \tag{2.5}$$

The scalar potential describes the masses of particles as well as their interactions, and is given by

$$\begin{aligned} \mathcal{V}_0(\Phi, \sigma) =& \mu_\Phi^2 \Phi^\dagger \Phi + \lambda_\Phi \left(\Phi^\dagger \Phi\right)^2 + \mu_\sigma^2 \sigma^\dagger \sigma + \lambda_\sigma \left(\sigma^\dagger \sigma\right)^2 \\ & + \lambda_{\Phi\sigma} \Phi^\dagger \Phi \sigma^\dagger \sigma + \left(\frac{1}{2}\mu_b^2 \sigma^2 + \text{ h.c.}\right) \, , \end{aligned} \tag{2.6}$$

with Φ and σ given by

$$\Phi = \frac{1}{\sqrt{2}} \begin{pmatrix} G + iG' \\ \phi_h + h + i\eta \end{pmatrix} \, , \qquad \sigma = \frac{1}{\sqrt{2}} (\phi_\sigma + \sigma_R + i\sigma_I) \, , \tag{2.7}$$

where h, η, G, G', σ_R and σ_I are real scalar fields. In the potential we write all the terms with dimension up to four compatible with the symmetries of the gauge group, and we impose an additional $\sigma \to \sigma^*$ symmetry which also forces all the parameters of the potential to be real. The parameters ϕ_h and ϕ_σ are the vacuum expectation values (VEV) of the neutral $\mathcal{CP}$-even component of the Higgs doublet Φ and real part of the new scalar particle, respectively. In quantum field theory, particles are described as quantum fluctuations around their classical mean-fields, the average of the field in the vacuum, denoted by $\langle ... \rangle$, is the vacuum expectation value. We have that

$$\langle \Phi \rangle = \frac{1}{\sqrt{2}} \begin{pmatrix} 0 \\ \phi_h \end{pmatrix} \, , \qquad \langle \sigma \rangle = \frac{1}{\sqrt{2}} \phi_\sigma \, . \tag{2.8}$$

The VEV of the Higgs doublet ϕ_h is measured experimentally to be about 246.22 GeV [3]. The scalar VEV ϕ_σ is a free parameter of the model and can be chosen freely unless it breaks any theoretical or experimental constraints. The vacuum expectation values of the model, at zero temperature, are:

$$\phi_h(T = 0^2) = v_h = 246.22 \text{ GeV}, \quad \phi_\sigma(T = 0^2) = v_\sigma \, . \tag{2.9}$$

The model has two distinct interpretations depending if v_σ is zero or not. The differences will be discussed in the next section.

Just as in the SM, the VEV of the Higgs doublet will break the electroweak symmetry $SU(2)_L \times U(1)_Y$ into the local $U(1)_Q$. For this reason, the conservation of isospin T and hypercharge Y will be

---

[2] $\phi_h = 246.22$ GeV $= v_h$ and $\phi_\sigma = v_\sigma$ is only valid at the cosmic temperature of $T = 0$. In the past the Universe was warmer and the potential had a different shape and different VEVs. This will be explained in more detail on chapter 5. On chapter 3 and on the current we work at present time, i.e. at $T = 0$.

broken but the sum of the two will still be conserved. We define the new conversed quantum number as *electric charge* and it is given by

$$Q \equiv T_3 + Y\,. \tag{2.10}$$

where T_3 is the field eigenvalue of the third generator of weak isospin.

The potential must be stable so we impose the *boundedness from below* conditions, that do not allow the potential to become infinitely negative as fields become infinitely large

$$\lambda_\Phi > 0, \quad \lambda_\sigma > 0, \quad \lambda_{\Phi\sigma} > -2\sqrt{\lambda_\Phi \lambda_\sigma}\,. \tag{2.11}$$

To use perturbative theory we cannot have large couplings because they would violate the *unitarity* conditions. We impose that the eigenvalues of the 2 → 2 scattering matrix $\mathcal{M}_{2\to 2}$ must be smaller, in absolute value, than 8π. For our particular model those constraints are [14, 15]

$$|\lambda_\Phi|, |\lambda_\sigma|, |\lambda_{\Phi\sigma}| < 4\pi\,, \tag{2.12}$$

$$\left|2\lambda_\sigma + 3\lambda_\Phi \pm \sqrt{2\lambda_{\Phi\sigma}^2 + (2\lambda_\sigma - 3\lambda_\Phi)^2}\right| < 8\pi. \tag{2.13}$$

We further need to impose that the minimum of the potential is truly at the VEVs, otherwise perturbative theory cannot be used. That is done by forcing the linear field terms to vanish at the VEVs so that we are at a stationary point

$$\left.\frac{d\mathcal{V}_0(\Phi,\sigma)}{d\Phi}\right|_{\text{vacuum}} \equiv -T_h = 0 \quad \text{and} \quad \left.\frac{d\mathcal{V}_0(\Phi,\sigma)}{d\sigma}\right|_{\text{vacuum}} \equiv -T_\sigma = 0\,, \tag{2.14}$$

where T_h and T_σ are dubbed the *tadpole terms*. The minus sign comes from the definition of the tadpoles terms as the derivative of the Lagrangian instead of the derivative of the potential. In our model the tadpole terms are explicitly given by

$$T_h := -v_h(\mu_\Phi^2 + \frac{1}{2}\lambda_{\Phi\sigma} v_\sigma^2 + \lambda_\Phi v_h^2)\,, \tag{2.15}$$

$$T_\sigma := -v_\sigma(\mu_b^2 + \mu_\sigma^2 + \lambda_\sigma v_\sigma^2 + \frac{1}{2}\lambda_{\Phi\sigma} v_h^2)\,. \tag{2.16}$$

From this moment on we are going to split the analysis into the cases when we have a zero scalar VEV and a non-zero scalar VEV.

2.2.1 Zero Scalar VEV $v_\sigma = 0$

In this scenario we set v_σ to zero, therefore $T_\sigma = 0$ is fulfilled. When we set $T_h = 0$ we get

$$\mu_\Phi^2 = -v_\Phi^2 \lambda_\Phi\,, \tag{2.17}$$

which is the same relation that one gets from the Higgs mechanism in the SM [16]. We can determine the mass m_h of the Higgs particle as

$$m_h^2 = 2\lambda_\Phi v_h^2 \,. \tag{2.18}$$

The mass of σ_R and σ_I are dubbed as m_{D_1} and m_{D_2}, respectively. These are dark matter (DM) particles because at least one of them is stable. It can also be that if they are very close in mass that they are both DM candidates. The masses of these particles are given by

$$m_{D1}^2 = \mu_\sigma^2 + \mu_b^2 + \frac{\lambda_{\Phi\sigma} v_h^2}{2} \,, \tag{2.19}$$

$$m_{D2}^2 = \mu_\sigma^2 - \mu_b^2 + \frac{\lambda_{\Phi\sigma} v_h^2}{2} \,. \tag{2.20}$$

Here we can see the role that the parameter μ_b^2 plays in the model, its sign indicates which particle is the stable and metastable dark matter particle. Noting that

$$m_{D2}^2 - m_{D1}^2 = -2\mu_b^2 \,, \tag{2.21}$$

if $\mu_b^2 > 0$ then D_2 is the lightest particle of the two and is, consequently, the stable particle while D_1 is the metastable particle. If $\mu_b^2 < 0$ then they switch roles. The reason why the heavier DM particle is metastable, and therefore not stable, is because it can decay into the lightest DM particle at next-to-leading order by decaying to the other DM particle together with SM particles. The lighter particle cannot decay since no decay to other DM particles is kinematically allowed, and it is therefore stable.

2.2.2 Non-Zero Scalar VEV $v_\sigma \neq 0$

In this case we have a non zero scalar VEV $v_\sigma \neq 0$. To use perturbation theory we have to impose that the tadpoles vanish (Eqs. 2.16). This allows us to write the μ_σ and μ_Φ parameters as a function of the other parameters in the potential and the VEVs,

$$\mu_\sigma^2 = -\mu_b^2 - \lambda_\sigma v_\sigma^2 - \frac{1}{2}\lambda_{\Phi\sigma} v_h^2 \,, \tag{2.22}$$

$$\mu_\Phi^2 = -\lambda_\sigma v_\sigma^2 - \frac{1}{2}\lambda_{\Phi\sigma} v_h^2 \,. \tag{2.23}$$

In order to compute the mass of the particles, we expand the potential and collect all the bilinear terms. We soon notice the mixing between the h and σ_R fields and therefore we have rotate from the gauge basis into the mass basis. We do that by grouping the scalar fields in a vector and introducing an orthogonal rotation matrix, such that the length of the vector is preserved, to transform the fields. The fields in the two basis are written as

$$\begin{pmatrix} h \\ \sigma_R \end{pmatrix} \quad \text{and} \quad \begin{pmatrix} h_1 \\ h_2 \end{pmatrix} \,, \tag{2.24}$$

where the first vector is in the gauge basis and the second vector is the rotated fields in the mass basis. We define α as the mixing angle and the orthogonal matrix R as the rotation matrix

$$R(\alpha) = \begin{pmatrix} \cos(\alpha) & \sin(\alpha) \\ -\sin(\alpha) & \cos(\alpha) \end{pmatrix} , \tag{2.25}$$

and finally the two basis are related by the following transformation

$$\begin{pmatrix} h_1 \\ h_2 \end{pmatrix} = \begin{pmatrix} \cos(\alpha) & \sin(\alpha) \\ -\sin(\alpha) & \cos(\alpha) \end{pmatrix} \begin{pmatrix} h \\ \sigma_R \end{pmatrix} . \tag{2.26}$$

We can write the bilinear terms of the potential in a compact form, using the mass matrix of h and σ_R

$$\mathcal{V}_0(\Phi, \sigma)\Big|_{\text{bilinear}} = -\frac{1}{2} \begin{pmatrix} h \\ \sigma_R \end{pmatrix} \left[\begin{pmatrix} 2\lambda_\Phi v_h^2 & v_h v_\sigma \lambda_{\Phi\sigma} \\ v_h v_\sigma \lambda_{\Phi\sigma} & 2\lambda_\sigma v_\sigma^2 \end{pmatrix} - \begin{pmatrix} \frac{T_h}{v_h} & 0 \\ 0 & \frac{T_\sigma}{v_\sigma} \end{pmatrix} \right] \begin{pmatrix} h & \sigma_R \end{pmatrix} , \tag{2.27}$$

where we can identify the non-diagonal mass matrix as

$$M^2 = \left[\begin{pmatrix} 2\lambda_\Phi v_h^2 & v_h v_\sigma \lambda_{\Phi\sigma} \\ v_h v_\sigma \lambda_{\Phi\sigma} & 2\lambda_\sigma v_\sigma^2 \end{pmatrix} - \begin{pmatrix} \frac{T_h}{v_h} & 0 \\ 0 & \frac{T_\sigma}{v_\sigma} \end{pmatrix} \right] . \tag{2.28}$$

We left the tadpole terms explicitly because they will be important at higher orders. To determine the diagonal mass matrix we impose the minimum conditions, $T_h = T_\sigma = 0$, and rotate the fields. The result is a diagonal matrix with the masses squared in the diagonal,

$$R(\alpha) M^2 R^{-1}(\alpha) = \begin{pmatrix} m_{h_1}^2 & 0 \\ 0 & m_{h_2}^2 \end{pmatrix} , \tag{2.29}$$

so that the bilinear terms of the potential are written has

$$\mathcal{V}_0(\Phi, \sigma)\Big|_{\text{bilinear}} = -\frac{1}{2} \begin{pmatrix} h_1 & h_2 \end{pmatrix} \begin{pmatrix} m_{h_1}^2 & 0 \\ 0 & m_{h_2}^2 \end{pmatrix} \begin{pmatrix} h_1 \\ h_2 \end{pmatrix} . \tag{2.30}$$

To find the mixing angle α one needs to solve Eq. 2.29. We find the following expression for α

$$\tan(2\alpha) = \frac{\lambda_{\Phi\sigma} v_h v_\sigma}{\lambda_\Phi v_h^2 - \lambda_\sigma v_\sigma^2} , \tag{2.31}$$

as well as expressions for the masses of the $\mathcal{CP}$-even particles, which are easily found since rotations do not change the matrix eigenvalues

$$m_{h_1,h_2}^2 = \lambda_\Phi v_h^2 + \lambda_\sigma v_\sigma^2 \pm \frac{\lambda_\Phi v_h^2 - \lambda_\sigma v_\sigma^2}{\cos(2\alpha)} . \tag{2.32}$$

Finally, the mass for the dark matter candidate is given by

$$m_D^2 \equiv m_{\sigma_I}^2 = -2\mu_b^2 , \qquad \mu_b^2 < 0 . \tag{2.33}$$

2.3 Scalar Lagrangian

The scalar potential is not the complete picture, we also have to take into account the kinetic terms in order to write the full scalar Lagrangian

$$\mathcal{L}_S = (\partial_\mu \sigma)(\partial^\mu \sigma)^\dagger + (D_\mu \Phi)(D^\mu \Phi)^\dagger - \mathcal{V}_0(\Phi, \sigma)\,, \tag{2.34}$$

where D_μ is the covariant derivative. For a field with an $SU(2)_L \times U(1)_Y$ symmetry it is defined as

$$D_\mu = \partial_\mu - ig\frac{\tau_a}{2}W_\mu^a - ig'YB_\mu\,, \tag{2.35}$$

where we used the Einstein convention for repeated indices. g is the coupling constant of the $SU(2)_L$ group, g' the coupling constant of the $U(1)_Y$ group (Y is the generator of the $U(1)_Y$ group), τ_a are the Pauli matrices ($T_a = \tau_a/2$ are the generators of the $SU(2)_L$ group), W^a are the $SU(2)_L$ gauge fields and B is the $U(1)_Y$ gauge field. The new particle, σ, is an $SU(2)_L \times U(1)_Y$ scalar and so its covariant derivative is just the partial derivative. As in the SM, the Higgs VEV v_h breaks the electroweak gauge group down to the local $U(1)$ charge,

$$SU(2)_L \times U(1)_Y \to U(1)_Q\,. \tag{2.36}$$

The numbers of generator of the gauge group goes from $3+1=4$ to 1. The Goldstone theorem [17] tells us that three Goldstone bosons are created, the number of broken generators, and become the longitudinal polarization of the gauge bosons (gauge bosons become massive). The mass generation of the gauge bosons is induced the Higgs mechanism. To find the masses we collect the bilinear field terms (of W^a and B) of the scalar potential, dropping all kinetic terms, the ones with two partial derivatives. Only the Higgs covariant derivative of the doublet Φ contributes

$$-\mathcal{L}_S\big|_{\text{bilinear}} = -(D_\mu\Phi)(D^\mu\Phi)^\dagger|_{\text{bilinear}} = \frac{v_h^2}{8}\left[\left|W^1 - iW^2\right|^2 g^2 + \left|-gW^3 + g'B\right|^2\right]. \tag{2.37}$$

This expression tells us that $W^1 \pm iW^2$ form a particle-antiparticle pair, and that there is a mixing between W^3 and B. The mass eigenstates are obtained by the following transformations

$$W^\pm = \frac{W^1 \mp W^2}{\sqrt{2}} \quad , \quad \begin{pmatrix} W^3 \\ B \end{pmatrix} = \begin{pmatrix} c_w & s_w \\ -s_w & c_w \end{pmatrix}\begin{pmatrix} Z \\ A \end{pmatrix} \quad , \quad g = \frac{e}{s_w} \quad , \quad g' = \frac{-e}{c_w}\,, \tag{2.38}$$

with $c_w = \cos\Theta$, $s_w = \sin\Theta$, where Θ is the Weinberg angle. After inserting these transformation into Eq. 2.37 we get

$$-\mathcal{L}_S\big|_{\text{bilinear}} = \frac{v_h^2 g^2}{4}W_\mu^+ W^{-\mu} + \frac{v_h^2 g^2}{8c_w^2}Z_\mu Z^\mu\,. \tag{2.39}$$

The masses of the gauge bosons are

$$m_W = \frac{v_h g}{2} \approx 80.379\,\mathrm{GeV} \tag{2.40}$$

$$m_Z = \frac{v_h g}{2c_w} \approx 91.1876\,\mathrm{GeV} \tag{2.41}$$

$$m_A = 0\,. \tag{2.42}$$

Notice that the ρ parameter, introduced in Eq. 2.2, is identically 1 at tree-level in this model.

2.4 Lagrangian

In this section I will be making a very short description of the full Lagrangian which will be used in this thesis in order to fix the notation. It is given by

$$\mathcal{L}_{\text{CxSM}} = \mathcal{L}_{\text{Gauge}} + \mathcal{L}_{\text{Fermion}} + \mathcal{L}_{\text{S}} + \mathcal{L}_{\text{Yukawa}} + \mathcal{L}_{\text{GF}} + \mathcal{L}_{\text{Ghost}}\,, \tag{2.43}$$

where $\mathcal{L}_{\text{S}}$ is the scalar Lagrangian discussed in the previous section 2.3. The remaining terms are going to be discussed in the following sections.

2.4.1 Gauge Lagrangian

The Gauge Lagrangian is composed by the kinetic terms of the gauge bosons. It cannot have explicit mass terms because that would break $SU(2)_L \times U(1)_Y$ symmetry.

$$\mathcal{L}_{\text{Gauge}} = \frac{1}{4} G^a_{\mu\nu} G^{a\mu\nu} + \frac{1}{4} W^a_{\mu\nu} W^{a\mu\nu} + \frac{1}{4} B_{\mu\nu} B^{\mu\nu}\,, \tag{2.44}$$

where $G^a_{\mu\nu}$, $W^a_{\mu\nu}$, $B^a_{\mu\nu}$ are, respectively, the field strength tensors of the gluons fields, the $SU(2)_L$ gauge bosons and the $U(1)_Y$ gauge boson. The tensors are defined as

$$G^a_{\mu\nu} = \partial_\mu G^a_\nu - \partial_\nu G^a_\mu + f^{abc} G^b_\mu G^c_\nu\,, \tag{2.45}$$

$$W^a_{\mu\nu} = \partial_\mu W^a_\nu - \partial_\nu W^a_\mu + \epsilon^{abc} G^b_\mu G^c_\nu\,, \tag{2.46}$$

$$B_{\mu\nu} = \partial_\mu B_\nu - \partial_\nu B_\mu\,, \tag{2.47}$$

where f^{abc} are the $SU(3)$ structure constants and ϵ^{abc} are the $SU(2)$ structure constants.

2.4.2 Fermionic Lagrangian

The Fermionic Lagrangian is responsible for the kinetic terms of the fermionic fields as well as the gauge interactions. It is given by

$$\mathcal{L}_{\text{Fermion}} = \sum_q i\bar{q}\gamma^\mu D_\mu q + \sum_l i\bar{l}\gamma^\mu D_\mu l \tag{2.48}$$

where q are the quark fields and l are the leptonic fields. The covariant derivative D_μ is not the same for all the fields and should be changed according to the quantum numbers that each field. The fields with a bar over them, e.g. $\overline{q}$, are called the adjoint fields and they are defined as $\overline{q} = q^\dagger \gamma^0$ in the Dirac representation [16]. They are necessary to write Lorentz invariants and Lorentz vectors in the Lagrangian. There are 6 quarks. They can be organized as up-type quarks $p:$ $\{u$ (up), t (top), c (charm)$\}$ and down-type quarks $n:\{d$ (down), b (bottom) and s (strange)$\}$ quark. It is also useful to group them in flavours which are $\{(u,d),\ (c,s),\ (t,b)\}$. There are 6 leptons. They can be grouped into the massive leptons : e (electron), μ (muon) and τ (tau) and the massless leptons ν_e (electron neutrino), ν_μ (muon neutrino) and ν_τ (tau neutrino). The leptonic families are $\{(\nu_e, e),\ (\nu_\mu, \mu),\ (\nu_\tau, \tau)\}$.

A central point of the Standard Model is that only left-handed chiral particles are present in the weak interaction, hence the L in the $SU(2)_L$ gauge group. As a consequence, since neutrinos are massless and only found in left-handed states, we do not need right-handed neutrinos in our Lagrangian[3]. The meaning of left and right-handed chiral states comes from the chirality operator $\gamma^5 \equiv i\gamma^0\gamma^1\gamma^2\gamma^3$, where $\gamma^i,\ i \in \{0,1,2,3\}$ are the Dirac matrices. The left and right chirality projection operators are defined as

$$P_R = \frac{1+\gamma^5}{2} \quad , \quad P_L = \frac{1-\gamma^5}{2}\,, \tag{2.49}$$

respectively. This operator is the operator that splits the Dirac spinors into components with different chirality,

$$\Psi = (P_R + P_L)\Psi = \Psi_R + \Psi_L . \tag{2.50}$$

In the relativistic limit, chirality has the same handedness as the helicity operator $\vec{h} = \frac{\vec{s}\cdot\vec{p}}{p^2}$, that is why we can use right-handed chirality and helicity interchangeably for neutrinos. In the Standard Model left-handed and right-handed chiral particle have different interactions and belong to different representations of the gauge groups. Left-handed particle are grouped into $SU(2)_L$ doublets while the right-handed particles belong in $SU(2)_L$ singlets

$$q = \begin{pmatrix} p_{\alpha L} \\ n_{\alpha L} \end{pmatrix},\, p_{\alpha R},\, n_{\alpha R} \quad , \quad l = \begin{pmatrix} \nu_{\beta L} \\ l_{\beta L} \end{pmatrix},\, l_{\beta R}\,, \tag{2.51}$$

where $\alpha \in \{u,c,t\}$ ($\beta \in \{e,\mu,\tau\}$) is the quark (lepton) flavour (family).

If we try to add a mass term to the Fermionic Lagrangian we run into a problem

$$-m_e\bar{e}e = -m_e\bar{e}(P_R^2 + P_L^2)e = -m_e(\overline{e_L}e_R + \overline{e_R}e_L)\,. \tag{2.52}$$

Therefore terms like $\overline{e_L}e_R$ and $\overline{e_R}e_L$ break the gauge group and so explicit mass terms for the fermions cannot exist in the Lagrangian.

---

[3] This is an approximation of the SM, in reality they have a very small mass so we can have both left and right-handed neutrinos.

2.4.3 Yukawa Lagrangian

The Yukawa Lagrangian is responsible for the interactions between the scalar sector and the fermionic sector. It is also responsible for the fermion masses which are generated when the Higgs field acquires its VEV. We define the quark and lepton left-handed doublets, respectively, as

$$Q_i = \begin{pmatrix} p_{iL} \\ n_{iL} \end{pmatrix} \quad , \quad L_\beta = \begin{pmatrix} \nu_{\beta L} \\ l_{\beta L} \end{pmatrix} \tag{2.53}$$

where only left-handed particles are present. The Yukawa Lagrangian is constructed by combining the Q_i and L_β doublets with the Φ doublet in an $SU(2)_L$ invariant way. In order to build hypercharge invariant terms, we couple these terms with their right-handed components. A table with the quantum numbers of the fermions of the SM is shown below 2.1.

	p_L	p_R	n_L	n_R	l_L	l_R	ν_L
T^3	$\frac{1}{2}$	0	$-\frac{1}{2}$	0	$-\frac{1}{2}$	0	$\frac{1}{2}$
Y	$\frac{1}{6}$	$\frac{2}{3}$	$\frac{1}{6}$	$-\frac{1}{3}$	$-\frac{1}{2}$	-1	$-\frac{1}{2}$
Q	$\frac{2}{3}$	$\frac{2}{3}$	$-\frac{1}{3}$	$-\frac{1}{3}$	-1	-1	0

Table 2.1: Quantum numbers of the SM fermions.

All the possible combinations of allowed terms are

$$\mathcal{L}_{\text{Yukawa}} = -\sum_{i,j} \overline{Q_i} \Gamma_{i,j} n_{jR} \Phi - \sum_{i,j} \overline{Q_i} \Delta_{i,j} p_{jR} \tilde{\Phi} - \sum_{\beta} y_\beta \overline{L_{\beta L}} l_{\beta R} \Phi + (h.c.) \,, \tag{2.54}$$

where $\tilde{\Phi} = i\sigma^2 \Phi^*$ is the $SU(2)$ Higgs doublet with $Y = -\frac{1}{2}$, $\Gamma_{i,j}$, $\Delta_{i,j}$ and y_β are the Yukawa couplings, *h.c.* is the hermitian conjugate of the expression that came before. The Higgs VEV will cause the appearance of terms like $-v_h \Gamma_{i,j} \overline{n_{iL}} n_{jR} + (h.c.)$ which are the mass terms of the n-quarks, the same happens for the p-quarks and leptons. The quark Yukawa couplings $\Gamma_{i,j}$, $\Delta_{i,j}$ are, in general, not diagonal. In the quark sector, we cannot simultaneously diagonalize all Yukawa matrices, this allows for different flavours to interact via charged bosons through the CKM matrix [16]. The same does not happen in the leptonic sector, the inexistence of right-handed neutrinos allows us to diagonalize the Yukawa coupling y_β so that charged-current interactions can only happen inside each leptonic family. When diagonalizing the mass terms we notice that flavour changing neutral currents (FCNC) vanish at tree level.

2.4.4 Gauge Fixing Lagrangian

The gauge fixing Lagrangian is necessary so that the gauge boson propagators can be properly defined. For each gauge boson i there is a gauge parameter ξ_i that is introduced which acts as a Lagrange multiplier.

The gauge parameters are unphysical quantities that can be chosen arbitrarily, and all observables (e.g. amplitudes, widths, etc) are independent of them. In the R_ξ gauge, the Lagrangian is given by

$$\mathcal{L}_{\text{GF}} = -\frac{1}{2\xi_G} F_G^2 - \frac{1}{2\xi_A} F_A^2 - \frac{1}{2\xi_Z} F_Z^2 - \frac{1}{\xi_W} F_{W^-} F_{W^+} \,. \tag{2.55}$$

where

$$F_G^a = \partial^\mu G_\mu^a \,, \tag{2.56}$$

$$F_A^a = \partial^\mu A_\mu^a \,, \tag{2.57}$$

$$F_Z^a = \partial^\mu Z_\mu^a - \xi_Z m_Z \eta \,, \tag{2.58}$$

$$F_{W^+}^a = \partial^\mu W_\mu^{+a} - \xi_W m_W G \,, \tag{2.59}$$

$$F_{W^-}^a = \partial^\mu W_\mu^{-a} + \xi_W m_W G' \,. \tag{2.60}$$

The most common choices for calculations are [18]

- Lorenz gauge $\xi = 0$
- Feynman-t'Hooft gauge $\xi = 1$
- Unitary gauge $\xi \to \infty$, which decouple the Goldstone bosons and ghosts from the theory.

2.4.5 Ghost Lagrangian

The gauge fixing procedure introduced in Eq. 2.55 enables us to define the gauge bosons propagators properly, but it also enables for the propagation of non-transversal modes of the gauge bosons which indicates that we have too many degrees of freedom [18]. In the path integral formalism these additional degrees of freedom are cancelled by the appearance of a non trivial Jacobian with the form of a determinant [19]. A way to simplify the calculations is to write the determinant as a functional of the Grassmann numbers

$$\det(\partial_\mu \mathcal{D}^\mu) = \int \mathcal{D}\bar{\theta}\mathcal{D}\theta \exp\left\{ i \int \mathrm{d}^4x \, \bar{\theta}(-\partial_\mu D^\mu)\theta \right\} , \tag{2.61}$$

where θ are the Grassmann fields (numbers), which anti-commute

$$\theta_i \theta_j = -\theta_j \theta_i \,,$$

and are scalars under Lorentz transformations. This method transforms the non trivial determinant into interactions of a new ghost particle θ_i so that calculations are simplified at the cost of additional Feynman diagrams. These new ghost fields do not obey the spin-statistics theorem [18] and therefore are unphysical particles that can only appear as internal lines of Feynman diagrams, and not in external legs. The ghost Lagrangian is given by

$$\mathcal{L}_{\text{Ghost}} = \sum_{i=1}^{4} \left[\bar{c}_+ \frac{\partial(\delta F_{W^+})}{\partial(\alpha^i)} + \bar{c}_- \frac{\partial(\delta F_{W^-})}{\partial(\alpha^i)} + \bar{c}_Z \frac{\partial(\delta F_A)}{\partial(\alpha^i)} + \bar{c}_A \frac{\partial(\delta F_Z)}{\partial(\alpha^i)} \right] c_i \tag{2.62}$$

$$+ \sum_{a,b=1}^{8} \overline{\omega}_a \frac{\partial(\delta F_G^a)}{\partial(\beta^b)} \omega_b \,, \tag{2.63}$$

where c_+, c_-, c_Z, c_A and ω_a are, respectively, the ghost fields corresponding to the W^+, W^-, Z, A and gluons bosons. The α_i and β_b are a parametrization to find the analytical expression for the variation of the gauge fixing terms F_V. The complete expression is given in Ref. [20]. The ghost Lagrangian is also necessary to ensure unitarity and gauge independent results. One can think of ghost particles as particles with negative degrees of freedom that cancel against those introduced during the gauge fixing procedure.

Chapter 3

Renormalization

3.1 Introduction

The main goal of this chapter is to calculate the next-to-leading order decay width of the Higgs boson into two dark matter particles. The 1-loop contributions to the decay width will produce infinite results and we have to perform the renormalization of the process, i.e. to remove the divergent parts in a consistent way. We are going to perform the renormalization in 4 different schemes. The different schemes originate from the possible ways to renormalize the VEV v_σ and mixing angle α. A thorough discussion on the different schemes is performed in the following sections.

Using `ScannerS` [14, 15] we can collect a sample of parameter points that fulfil the most relevant theoretical constraints such as perturbative unitarity, vacuum stability and boundedness from below as well as the most relevant experimental constraints from colliders such as the measurements of the Higgs coupling to the remaining SM particles and the bounds coming from direct searches for new scalars. Finally, dark matter constraints are also included. The DM relic density has to be below the experimental value measured by the Plank experiment [21], the DM-nucleon cross section has to be below the bounds set by the XENON1T [22] experiment and the invisible width constraints are also taken into account [23]. All constraints are included in `ScannerS` via the interface with other high energy physics codes: `HiggsBounds-5` [24] for the Higgs searches and `HiggsSignals-2` [25] for the experimental constraints of the SM-like Higgs boson measurements. For the DM constraints, the relic density and the nucleon-DM cross section for direct detection are calculated using `MicroOMEGAs-5.2.1` [26]. To simplify the notation we are going to consider that the h_1 always coincides with the SM-like Higgs

$$m_{h_1} = 125.1\,\text{GeV}\,, \tag{3.1}$$

and the scalar h_2 can be lighter or heavier than the SM-like Higgs.

The Feynman Rules for the CxSM were generated using the `Mathematica` [27] package `FeynRules` [28]. The analytic expression for the amplitudes were generated with the `FeynArts` [29] package and

`FeynCalc` [30] was used to write the the amplitudes as functions of the Passarino-Veltman [31] integrals. The numerical value of the integrals is obtained from `LoopTools` [32, 33]

3.2 Leading Order Amplitude

The calculation of a particle width using quantum field theory is a perturbative process. In most cases, like the one we are studying, the first contribution comes from the tree level amplitude[1]. If we want to increase the precision of our calculations we have to calculate the contributions of the next order in perturbation theory, which translates into the 1-loop corrections in our case. The leading-order contribution to the amplitude is straightforward since it only involves scalar fields and it is given by the single diagram

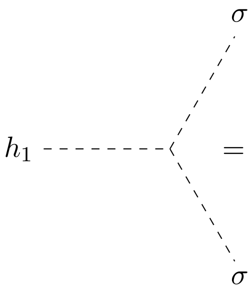

$$= i\mathcal{A}^{\text{LO}}_{h_1\sigma_I\sigma_I} = -i\frac{m^2_{h_1}\sin(\alpha)}{v_\sigma} \equiv i\lambda_{h_1\sigma_I\sigma_I}\,.$$

Figure 3.1: Leading order amplitude $i\mathcal{A}^{\text{LO}}_{h_1\sigma_I\sigma_I}$ of the Higgs decay into dark matter particles.

where we defined $\lambda_{h_1\sigma_I\sigma_I}$ as the trilinear coupling between the h_1, σ_I and σ_I fields.

3.3 Next-to-leading Order Amplitude

In order to calculate the next-to-leading order (NLO) amplitude we need to calculate the 1-loop corrections, which are composed by the diagrams of the next order in perturbation theory. The 1-loop contributions are not so trivial. If one is tempted to simply add the Feynman diagrams of the following order one runs into the problem of the appearance of diagrams with internal loops which diverge when we integrate over the loop momentum. To solve this problem we need to add the corresponding counterterm Lagrangian which arises from the transformation of the initial Lagrangian (more details in the next sections). The goal of renormalization is to choose these counterterms such that the divergences that appear in the 1-loop corrections are cancelled consistently, therefore achieving a finite result for any physical process. The physical process also needs to be gauge independent, an issue to be discussed later.

We are going to split the 1-loop contributions into eight parts: the vertex correction $\mathcal{A}^{\text{VC}}$, the vertex counterterm $\mathcal{A}^{\text{CT}}$ and the corrections to the external legs $\mathcal{A}^{\text{leg},i}$ with the corresponding counterterms for each leg $\mathcal{A}^{\text{leg CT},i}$, which is depicted in Fig. 3.2.

---

[1] This is not always the case, e.g. in the SM the Higgs decay to photons only happens at 1-loop

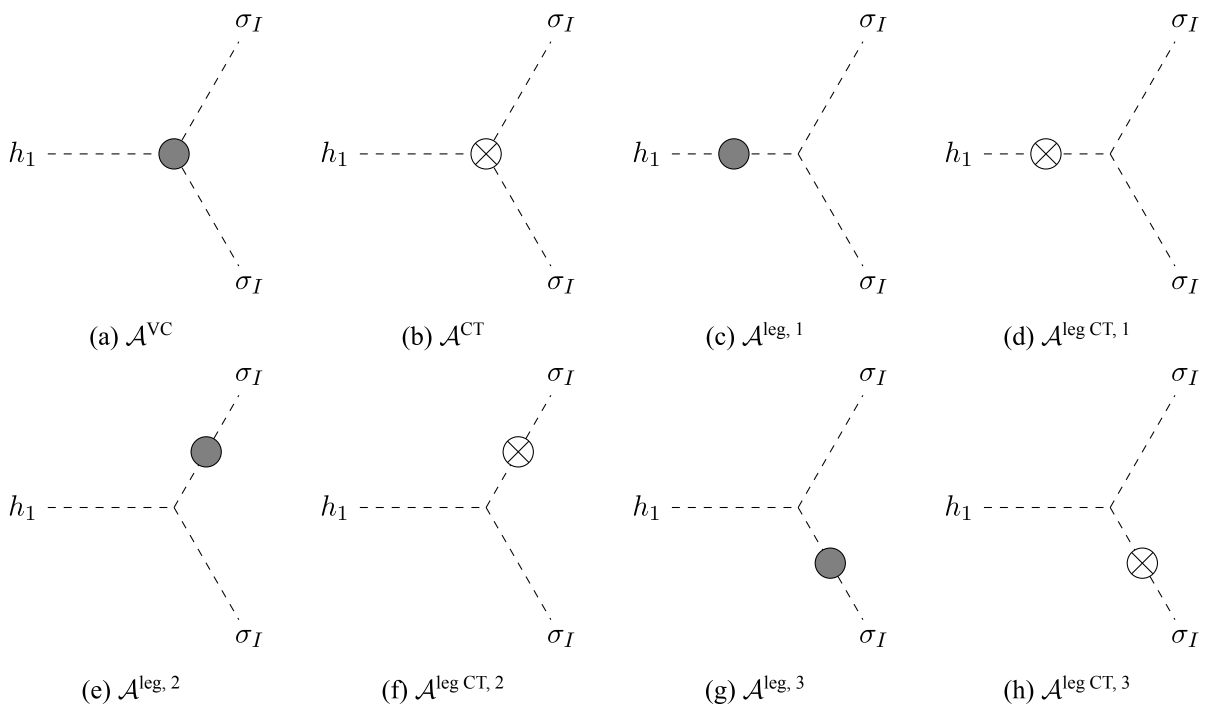
σ_I
h_1
σ_I
(a) $\mathcal{A}^{\text{VC}}$
(b) $\mathcal{A}^{\text{CT}}$
(c) $\mathcal{A}^{\text{leg, 1}}$
(d) $\mathcal{A}^{\text{leg CT, 1}}$
(e) $\mathcal{A}^{\text{leg, 2}}$
(f) $\mathcal{A}^{\text{leg CT, 2}}$
(g) $\mathcal{A}^{\text{leg, 3}}$
(h) $\mathcal{A}^{\text{leg CT, 3}}$

Figure 3.2: 1-loop corrections to the leading order amplitude. $\mathcal{A}^{\text{VC}}$ is vertex correction, $\mathcal{A}^{\text{CT}}$ is the vertex counterterm, $\mathcal{A}^{\text{leg},i}$ is the leg correction for the leg i and $\mathcal{A}^{\text{leg CT},i}$ is the vertex counterterm for the leg i. The gray circles indicates the 1-loop corrections while the crossed circles indicate diagrams coming from the counterterm Lagrangian.

The 1-loop amplitude is the sum of all the 1-loop contribution from the diagrams above

$$\begin{aligned} i\mathcal{A}^{\text{1-loop}} &= i\mathcal{A}^{\text{VC}} + i\mathcal{A}^{\text{CT}} \\ &+ i\mathcal{A}^{\text{leg, 1}} + i\mathcal{A}^{\text{leg, 2}} + i\mathcal{A}^{\text{leg, 3}} \\ &+ i\mathcal{A}^{\text{leg CT, 1}} + i\mathcal{A}^{\text{leg CT, 2}} + i\mathcal{A}^{\text{leg CT, 3}} . \end{aligned} \tag{3.2}$$

We define the next-to-leading order amplitude as[2] the sum of the leading order amplitude with the 1-loop corrections

$$i\mathcal{A}^{\text{NLO}} = i\mathcal{A}^{\text{LO}} + i\mathcal{A}^{\text{1-loop}} . \tag{3.3}$$

Computing the squared absolute value of the NLO amplitude yields

$$|\mathcal{A}^{\text{NLO}}|^2 \approx |\mathcal{A}^{\text{LO}}|^2 + 2\,\text{Re}[(\mathcal{A}^{\text{LO}})^* \mathcal{A}^{\text{1-loop}}] \tag{3.4}$$

where we neglected the term $|\mathcal{A}^{\text{1-loop}}|^2$ because it is a second order relative to the expansion parameter.

---

[2] If there is no tree level amplitude then next-to-leading order amplitude is $i\mathcal{A}^{\text{1-loop}} + i\mathcal{A}^{\text{2-loop}}$ and so on.

3.4 Decay Width

In this section we present the calculation of the decay width. The branching raio is what is measured experimentally (usually a cross section times a branching ratio) but the decay width is the first step to calculate the branching ratio. To go from the amplitude to the decay width we have to integrate the amplitude over the Lorentz invariant phase space

$$\Gamma^{\text{NLO}}_{h_1\sigma_I\sigma_I} = S\frac{(2\pi)^{-2}}{2E_{\sigma_I}}\int |\mathcal{A}^{\text{NLO}}_{h_1\sigma_I\sigma_I}|^2\delta^4(p^\mu_{h_1} - p^\mu_{\sigma_I,1} - p^\mu_{\sigma_I,2})\delta(p^2_{\sigma_I,1} - m^2_\sigma)\delta(p^2_{\sigma_I,2} - m^2_\sigma)d^4p_{\sigma_I,1}d^4p_{\sigma_I,2} \tag{3.5}$$

where $p^\mu_{\sigma_I,1}$ and $p^\mu_{\sigma_I,2}$ are the four momentum vector for each outgoing particle. After some simplifications [16] the width is given by

$$\Gamma^{\text{NLO}}_{h_1\sigma_I\sigma_I} = S\frac{p_{\sigma_I}}{32\pi^2 m^2_{h_1}}\int |\mathcal{A}^{\text{NLO}}_{h_1\sigma_I\sigma_I}|^2 d\Omega \tag{3.6}$$

where p_{σ_I} is the σ_I absolute value of the linear momentum in the centre of mass (CM) reference frame, and $\int(...)d\Omega$ is the integration over the solid angle. S is the symmetry factor that accounts for indistinguishable particles, in our case, $S = \frac{1}{2!}$. Using the conservation of momentum $p^\mu_{h_1} = p^\mu_{\sigma_I,1} + p^\mu_{\sigma_I,2}$ and the energy–momentum relation $E^2_i = p^2_i + m^2_i$ for each particle i we can find an expression for p_{σ_I}, the magnitude of the momentum in the CM reference frame,

$$p_{\sigma_I} = \frac{1}{2}\sqrt{m^2_{h_1} - 4m^2_{\sigma_I}}, \tag{3.7}$$

and $m_{h_1} > 2m_{\sigma_I}$ for the process to be kinematically allowed. Putting everything together and integrating over the solid angle (the amplitude does not depend on the angle), we get the full expression for the decay width

$$\Gamma^{\text{NLO}}_{h_1\sigma_I\sigma_I} = \frac{\sqrt{m^2_{h_1} - 4m^2_{\sigma_I}}}{32\pi m^2_{h_1}}|\mathcal{A}^{\text{NLO}}_{h_1\sigma_I\sigma_I}|^2 \tag{3.8}$$

3.5 Regularization

The need for renormalization is not yet explicitly clear. Let us suppose we want to calculate the 1-loop correction to the Higgs decay into dark matter. The 1-loop diagrams will contain loops. An example of such a diagram is shown in Fig. 3.3.

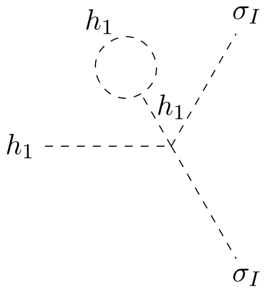

Figure 3.3: Example of a tadpole diagram that contains divergences. This contribution belongs to the $\mathcal{A}^{\text{VC}}$ diagrams in Fig. 3.2

The amplitude for the diagram Fig. 3.3 is given by

$$i\mathcal{A} = i\int d^4k\lambda_{h_1h_1\sigma_I\sigma_I}\frac{i}{-m^2_{h_1}}\lambda_{h_1h_1h_1}\frac{i}{k^2-m^2_{h_1}} \propto i\int\frac{d^4k}{k^2-m^2_{h_1}} \tag{3.9}$$

where we have to integrate over the internal loop momentum. The calculation of this integral is not trivial because we have a non-trivial metric, dia$(1,-1,-1,-1)$, and therefore we cannot change into spherical coordinates right away. Using Wick's rotation [17], that consists of defining the four-momentum $k^\mu_E = (k^0_E, \vec{k}) = (-ik^0, \vec{k})$ which transforms as an Euclidian vector with $k^2 = -k^2_E$, and with Cauchy integral theorem[3] we can change our metric from Minkowski into Euclidian and, consequently, go to spherical coordinates. The integral then becomes

$$i\int\frac{d^4k}{k^2-m^2_{h_1}} = \int dk^4_E\frac{1}{k^2_E+m^2_{h_1}} = 2\pi^2\int_0^\infty dk_E\frac{k^3_E}{k^2_E+m^2_{h_1}} = \infty\,. \tag{3.10}$$

The integrand diverges as we take $k_E \to \infty$, so the integral also diverges and the amplitude, for this tadpole diagram, is infinite.

The first step of renormalization is *regularization*. Regularization consists of making the loop integrals depend on a parameter that controls the infinities, that parameter is called *regulator*. The aim of regularization is to isolate the infinities. The method we will be using is *dimensional regularization* because it preserves the gauge structure of the theory. We start by going from an integral in 4 dimensions to a integral in d-dimensions, where $d = 4-\varepsilon$

$$\int I(k)d^4k \to (2\pi\mu)^{4-d}\int I(k)d^dk = (2\pi\mu)^{4-d}\int k^{d-1}I(k)dk\int d\Omega_d \tag{3.11}$$

where $I(k)$ is an arbitrary integrand. The infinity is restored when we set the regulator to zero, i.e. $\varepsilon \to 0$. This procedure consists of using the analytical continuations for each expression in d-integer dimensions that comes out the integral, this is why we are allowed to take the limit $d \to 4$. The parameter μ ensures that the dimensionality of the integrand is maintained. The parameter μ is called the *renormalization scale*, although the dependence on the renormalization scale is unwanted it is not always possible to cancel it. We can simplify the integral above using the following expressions [17]

---

[3] $\oint f(z)dz = 0$ if there are no simple poles inside the path.

$$\int_0^\infty dk_E \frac{k_E^a}{\left(k_E^2+M^2\right)^b} = M^{2\left(\frac{a+1}{2}-b\right)} \frac{\Gamma\left(\frac{a+1}{2}\right)\Gamma\left(b-\frac{a+1}{2}\right)}{2\Gamma(b)}, \qquad \Omega_d = \int d\Omega_d = \frac{2\pi^{d/2}}{\Gamma(d/2)}, \tag{3.12}$$

where $\Gamma(n)$ is the factorial analytical continuation, with $\Gamma(n+1) = n! = n \times n-1 \times \ldots \times 2 \times 1\,, n \in \mathbb{Z}^+$. It is defined as

$$\Gamma(x) = \int\limits_0^\infty s^{x-1} e^{-s} ds, \qquad\qquad \Gamma(n+1) = n!,\; n \in \mathbb{N}\,. \tag{3.13}$$

In this work, we catalogue the internal loop momentum integrals into the Passarino-Veltman (PV) Integrals [31, 34]. The ones relevant for our calculations are

$$A_0\left(m_0^2\right) = \frac{(2\pi\mu)^\epsilon}{i\pi^2}\int d^dk \frac{1}{k^2-m_0^2}\,, \tag{3.14}$$

$$B_0\left(r_{10}^2, m_0^2, m_1^2\right) = \frac{(2\pi\mu)^\epsilon}{i\pi^2}\int d^dk \prod_{i=0}^{1} \frac{1}{\left[(k+r_i)^2-m_i^2\right]}\,, \tag{3.15}$$

$$C_0\left(r_{10}^2, r_{12}^2, r_{20}^2, m_0^2, m_1^2, m_2^2\right) = \frac{(2\pi\mu)^\epsilon}{i\pi^2}\int d^dk \prod_{i=0}^{2} \frac{1}{\left[(k+r_i)^2-m_i^2\right]}\,, \tag{3.16}$$

$$\text{where } r_{ij}^2 = (r_i - r_j)^2\,.$$

Fortunately, the package `FeynCalc` can perform the catalogation for us and using `LoopTools` we can get a numerical value for the the Passarino-Veltman integrals. The numerical results is presented considering that the divergent part Δ

$$\Delta = \frac{2}{\varepsilon} - \gamma_E + \ln(4\pi)\,, \tag{3.17}$$

is zero, equivalent to the $\overline{\text{MS}}$ scheme. We can change the settings of `LoopTools` such that Δ and μ take other values, this allows us to check if our results are divergences free and if they do not depend on the renormalization scale. As an example the tadpole amplitude presented in Eq. 3.9 can be written as a function of the Passarino-Veltman integral as

$$i\mathcal{A} = \frac{i}{m_{h_1}^2}\lambda_{h_1h_1\sigma_I\sigma_I}\lambda_{h_1h_1h_1}\int d^4k \frac{1}{k^2-m_{h_1}^2} \overset{\text{PV}}{=} \frac{i}{m_{h_1}^2}\lambda_{h_1h_1\sigma_I\sigma_I}\lambda_{h_1h_1h_1}\left[i\pi A(m_{h_1}^2)\right] \tag{3.18}$$

3.6 Renormalization

Now that we found a way to regularize the infinities, it is time to start defining the counterterm Lagrangian which will cancel the divergences. The usual procedure is to consider that all of the parameters of the potential, as well as the fields, are infinite. They are called the *bare* parameters and *bare* fields. The standard notation is a 0 in the subscript (i.e. λ_0 or ϕ_0). Then we consider that these bare quantities can each be split into a finite part and counterterm (denoted with a δ). The counterterms are considered to be infinite. The finite parts defined in this way are dubbed as the *renormalized parameters/fields*. The bare parameters are defined as

$$\begin{aligned}\mu_{\sigma,0} &= \mu_\sigma + \delta\mu_\sigma \,, \\ \lambda_{\sigma,0} &= \lambda_\sigma + \delta\lambda_\sigma \,. \end{aligned} \tag{3.19}$$

The bare fields are defined as

$$\sigma_{I,0} = \sqrt{Z_{\sigma_I}}\sigma_I \,, \tag{3.20}$$

where $\sqrt{Z_{\sigma_I}}$ is the field renormalization constant to all orders of perturbation theory. Since we only want the next to leading order contribution it is useful to expand this renormalization constant as

$$\sqrt{Z_{\sigma_I}} \approx \left(1 + \frac{\delta Z_{\sigma_I}}{2}\right) . \tag{3.21}$$

We have seen before that in our model we have mixing between the Higgs field and the real component of σ. For that reason, we have to introduce field renormalization constants that also mixes the counterterms of the fields because they have the same quantum numbers,

$$\begin{pmatrix} h_1 \\ h_2 \end{pmatrix}_0 = \sqrt{Z_h}\begin{pmatrix} h_1 \\ h_2 \end{pmatrix} . \tag{3.22}$$

Just as before, we expand this matrix up to first order

$$\sqrt{Z_h} \approx \left(\mathbb{1} + \frac{\delta Z_h}{2}\right) = \begin{pmatrix} 1 + \dfrac{\delta Z_{h_1 h_1}}{2} & \dfrac{\delta Z_{h_1 h_2}}{2} \\ \dfrac{\delta Z_{h_2 h_1}}{2} & 1 + \dfrac{\delta Z_{h_2 h_2}}{2} \end{pmatrix} . \tag{3.23}$$

These shifts do not happen only to the fields present in Eq. 3.19, Eq. 3.20 and Eq. 3.22 but to all parameters and fields appearing in the Lagrangian. But since we are only interested in a particular decay we do not have to find the counterterms for all fields and parameters and we will only focus on the scalar sector. With these rescalings we rewrite the whole Lagrangian, up to first order, as

$$\mathcal{L}_{\text{CxSM},0} \approx \mathcal{L}_{\text{CxSM}} + \delta\mathcal{L}_{\text{CxSM}} \,, \tag{3.24}$$

where $\mathcal{L}_{\text{CxSM}}$ is the tree level Lagrangian which produces the tree-level diagrams as in Fig. 3.3, and the 1-loop diagrams (gray circles) in Fig. 3.2. The $\delta\mathcal{L}_{\text{CxSM}}$ is called the counterterm Lagrangian and is responsible for generating the counterterm diagrams at 1-loop, which are represented as a crossed circle in Fig. 3.2.

The input parameters in the theory are chosen, as much as possible, as physical quantities that can be measured. In the potential, we have 6 independent parameters. The two VEVs are not independent as they are determined by the minimization condition. The most obvious choice is the masses of the particles and to complete the number of independent parameters we also choose the VEVs and the mixing angle α, that can be extracted from physical processes. We chose for input parameters

$$m_{h_1}, m_{h_2}, m_{\sigma_I}, v_h, v_\sigma, \alpha \,. \tag{3.25}$$

which are the only quantities that have to be renormalized. The shift in the DM mass is defined as

$$m^2_{\sigma_{I,0}} = m^2_{\sigma_I} + \delta m^2_{\sigma_I} \,, \tag{3.26}$$

and the mixing angle is shifted as

$$\alpha_0 = \alpha + \delta\alpha \,, \tag{3.27}$$

while for the VEVs we have

$$v_{h,0} = v_h + \delta v_h \tag{3.28}$$

$$v_{\sigma,0} = v_\sigma + \delta v_\sigma . \tag{3.29}$$

The mass matrix of the two Higgs bosons is redefined as

$$D_0^2 = D^2 + \delta D^2 \,. \tag{3.30}$$

although, as we will see in the next section, the counterterm δD^2 requires a more careful examination and is not necessarily diagonal.

3.7 On-shell Renormalization

In the next sections we are going to discuss how to find the parameter counterterms and field renormalization constants. In this particular section, we focus on the renormalization of the mass and of the corresponding field. This is not enough to calculate the counterterms because the minimum conditions also need to be discussed. The on-shell renormalization scheme aims to calculate the renormalized propagator using the *on-shell renormalization conditions*. First, it is useful to define the *1-particle irreducible* (1PI) diagrams, also called the *self-energies*. This is the set of $1 \to 1$, next to leading order diagrams, which cannot be split into two by cutting an internal line.

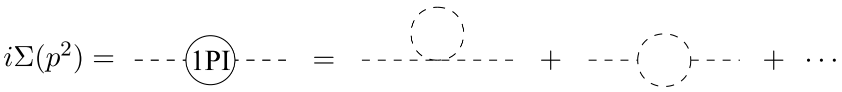

Figure 3.4: One-particle irreducible diagrams, also called self-energies. Set of diagrams that cannot be split into two by cutting an internal line. Although the self-energies are defined to all order of perturbation theory we only show, and use in our calculations, up to the leading order contribution.

Next we compute the bare propagator to all orders of perturbation theory by summing all 1PI diagrams as in

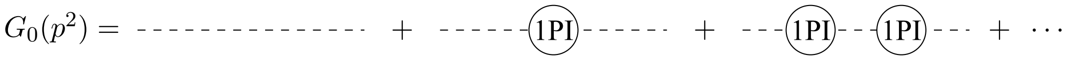

When we write the analytical expression for each diagram it is easy to notice a pattern that allows us to rewrite the whole sum as a geometric series as

$$\begin{aligned}G_0(p^2) =&\frac{i}{p^2-m_0^2}+\frac{i}{p^2-m_0^2}\left(i\Sigma(p^2)\frac{i}{p^2-m_0^2}\right)+\frac{i}{p^2-m_0^2}\left(i\Sigma(p^2)\frac{i}{p^2-m_0^2}\right)^2+\cdots\\ =&\frac{i}{p^2-m_0^2}\sum_{n=0}^{\infty}\left(i\Sigma(p^2)\frac{i}{p^2-m_0^2}\right)^n\\ =&\frac{i}{p^2-m_0^2+\Sigma(p^2)}\end{aligned} \tag{3.31}$$

To calculate the renormalized propagator we substitute the bare fields by the renormalized fields in the definition of the propagator in momentum space

$$\begin{aligned}G_0(p^2) &= \int e^{-ipx}\left\langle 0\right|T\left[\phi_0(x)\phi_0^*(0)\right]\left|0\right\rangle d^4x\\ &= \sqrt{Z}\left(\int e^{-ipx}\left\langle 0\right|T\left[\phi(x)\phi^*(0)\right]\left|0\right\rangle d^4x\right)\sqrt{Z^*}\\ &= \sqrt{Z}\hat{G}(p^2)\sqrt{Z}^*\,,\end{aligned} \tag{3.32}$$

where the $\hat{G}$ is the renormalized propagator[4] and T is the time order operator. Inverting Eq. 3.32 and introducing it into Eq. 3.31 yields

$$\hat{G}(p^2) = \frac{i}{p^2-m^2+\hat{\Sigma}(p^2)}\,, \tag{3.33}$$

where $\hat{\Sigma}(p^2)$ is the renormalized self-energy

$$\hat{\Sigma}(p^2) = \Sigma(p^2) - \delta m^2 + \frac{\delta Z}{2}\left(p^2-m^2\right) + \left(p^2-m^2\right)\frac{\delta Z^*}{2}\,. \tag{3.34}$$

---

[4] The hat $\wedge$ is standard notation for renormalized quantities

The renormalized self-energy is the result of expanding $\sqrt{Z}\left[(p^2 - m_0^2 + \Sigma(p^2)\right]\sqrt{Z}^*$ and collecting all next-to-leading order terms, i.e. everything except $p^2 - m^2$, into the new self-energy which we call *renormalized*. The procedure for mixing of fields is very similar but instead of having complex number we have 2×2 field renormalization constants, mass counterterms and self-energies.

The renormalized propagator is similar to the tree level propagator, apart from the renormalized self-energy in the denominator. We have the freedom to choose the counterterms, so we will impose the following three on-shell renormalization conditions [18, 17]

1. $\hat{G}(p^2)$ has a single pole at $p^2 = m^2$.
2. $\hat{G}(p^2)$ has residue i at $p^2 = m^2$.
3. Mixing of the fields vanishes at $p^2 = m^2$.

The analysis for one field or for two mixing field is different and will both be discussed next.

3.7.1 Single Field

The first condition imposes that the renormalized self-energy must vanish on-shell

$$\mathrm{Re}\left[\hat{\Sigma}(m^2)\right] = 0 \implies \delta m^2 = \mathrm{Re}\left[\Sigma(m^2)\right] \tag{3.35}$$

The second condition imposes that the residue is i at $p^2 = m^2$

$$i = (p^2 - m^2)\frac{i}{p^2 - m^2 + \hat{\Sigma}(p^2)}\Bigg|_{p^2=m^2} \overset{\text{L'Hôpital}}{=} \frac{i}{1 + \frac{d\hat{\Sigma}(p^2)}{dp^2}}\Bigg|_{p^2=m^2} \tag{3.36}$$

$$\mathrm{Re}\left[\frac{d\hat{\Sigma}(p^2)}{dp^2}\right]\Bigg|_{p^2=m^2} = 0 \implies \delta Z = -\,\mathrm{Re}\left[\frac{d\Sigma(p^2)}{dp^2}\right]\Bigg|_{p^2=m^2} \tag{3.37}$$

In this case, the third condition does not apply since there is no mixing.

We can see that that these conditions impose that the tree level propagator $G(p^2)$ coincide with the renormalized propagator $\hat{G}(p^2)$ on a vicinity of $p^2 = m^2$. These conditions allow us to renormalize the mass and the field renormalization constant of the DM particle

$$\delta m_{\sigma_I}^2 = \mathrm{Re}\left[\Sigma_{\sigma_I}(m_{\sigma_I}^2)\right] \tag{3.38}$$

$$\delta Z_{\sigma_I} = -\,\mathrm{Re}\left[\frac{d\Sigma_{\sigma_I}(p^2)}{dp^2}\right]\Bigg|_{p^2=m_{\sigma_I}^2} \tag{3.39}$$

3.7.2 Two Mixing Fields

The case for two mixing fields is not so trivial because the field renormalization constants are not diagonal. We start by defining the self-energy for two mixing fields as

$$i\Sigma_{h_ih_j}(p^2) =$$

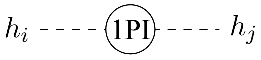

Figure 3.5: Self-energies for two mixing fields. In the case for mixing fields the incoming particle and outgoing particle is not always the same.

The next step is to calculate the renormalized propagator. Due the matricial nature of the mixing it is easier to analyse the the inverse propagator[5] instead of the propagator itself. It is given by the symmetric matrix

$$i\hat{G}^{-1}_{h_ih_j} = \left[\mathbb{1}p^2 - D^2 + \hat{\Sigma}_h(p^2)\right]_{h_ih_j} , \tag{3.40}$$

where is 2×2 renormalized self-energy matrix is given by

$$\hat{\Sigma}_h(p^2) = \Sigma_h(p^2) - \delta D^2 + \frac{\delta Z_h}{2}\left(\mathbb{1}p^2 - D^2\right) + \left(\mathbb{1}p^2 - D^2\right)\frac{\delta Z_h^\dagger}{2} , \tag{3.41}$$

where we introduced the following notation for the self-energy and renormalized self-energy

$$\Sigma_h(p^2) = \begin{pmatrix} \Sigma_{h_1h_1}(p^2) & \Sigma_{h_1h_2}(p^2) \\ \Sigma_{h_2h_1}(p^2) & \Sigma_{h_2h_2}(p^2) \end{pmatrix} \quad \text{and} \quad \hat{\Sigma}_h(p^2) = \begin{pmatrix} \hat{\Sigma}_{h_1h_1}(p^2) & \hat{\Sigma}_{h_1h_2}(p^2) \\ \hat{\Sigma}_{h_2h_1}(p^2) & \hat{\Sigma}_{h_2h_2}(p^2) \end{pmatrix} \tag{3.42}$$

Both $\Sigma_h(p^2)$ and $\hat{\Sigma}_h(p^2)$ are symmetric, this imposes $\delta Z_h = \delta Z_h^*$, i.e. the field renormalized counterterms must be real. The counterterm for the diagonal mass matrix δD^2 is symmetric and, in general, not diagonal. The reason is that the tadpoles themselves are going to be shifted during renormalization, so they will cause also a shift in the mass matrix. This discussion will be the subject of the next section. When we apply the first renormalization condition we get the same relation as before but only for the diagonal entries

$$\text{Re}\left[\hat{\Sigma}_{h_ih_i}(m^2_{h_i})\right] = 0 \implies \delta D^2_{h_ih_i} = \text{Re}\left[\Sigma_{h_ih_i}(m^2_{h_i})\right] . \tag{3.43}$$

The second condition yields the same results as for the single field but only for the diagonal field renormalization constants

$$\text{Re}\left[\frac{d\hat{\Sigma}_{h_ih_i}(p^2)}{dp^2}\right]\Bigg|_{p^2=m^2_{h_i}} = 0 \implies \delta Z_{h_ih_i} = -\,\text{Re}\left[\frac{d\Sigma_{h_ih_i}(p^2)}{dp^2}\right]\Bigg|_{p^2=m^2_{h_i}} . \tag{3.44}$$

---

[5] Also called the two point correlation function, up to a minus sign

The third condition imposes that the off-diagonal elements must vanish on-shell,

$$\hat{\Sigma}_{h_i h_j}(m^2_{h_i}) = 0\,, \tag{3.45}$$

$$\hat{\Sigma}_{h_i h_j}(m^2_{h_j}) = 0\,. \tag{3.46}$$

Therefore the counterterms for the off-diagonal field renormalization constants is

$$\delta Z_{h_i h_j} = \frac{2}{m^2_{h_i} - m^2_{h_j}} \left[\Sigma_{h_i h_j}(m^2_{h_i}) - \delta D^2_{h_i h_j} \right]\,, \quad i \neq j\,. \tag{3.47}$$

The complete expression for the field renormalization constants needs the matrix counterterm δD^2, which is yet to be determined. This is the subject of the next section.

3.8 Fleischer-Jegerlehner Tadpole Scheme

As we have seen in the last section, we need the off diagonal terms of the mass counterterm δD^2 matrix so that we can write the complete expression for the field renormalization constants. If we do not impose the tree level minimum conditions $T_h = T_\sigma = 0$, which we cannot do because all the parameters are shifted, then the diagonal mass counterterm matrix is not diagonal due to the tadpole equations

$$D^2_0 = \begin{pmatrix} m^2_{h_1,0} & 0 \\ 0 & m^2_{h_2,0} \end{pmatrix} - R_0 \begin{pmatrix} \frac{T_{h,0}}{v_{h,0}} & 0 \\ 0 & \frac{T_{\sigma,0}}{v_{\sigma,0}} \end{pmatrix} R_0^{-1}\,. \tag{3.48}$$

In this section we are going to use $h_i = h_1, h_2$ for the two mixing fields in the mass basis and $\phi_i = h, \sigma_R$ for the two mixing fields in the gauge basis. We are also going to neglect all second order contributions.

One can try to go around this issue by making the bare parameters also satisfy the tadpole equations, in that case we would have $T_{\phi_i,0} = 0$ making the counterterm mass matrix diagonal. This approach has a problem because there are non-zero 1-point functions at 1-loop such as

ϕ_i 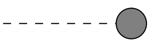 $= iT^{\text{1-loop}}_{\phi_i}$ (3.49)

disallowing the use of perturbation theory. To recover the condition that allows us to do perturbation theory at tree level (imposing vanishing tadpoles) we have to force that all 1-point functions must cancel the corresponding counterterm. That is the main reason we have to be careful with the tadpoles diagrams contributions.

In this work we use the method developed by Fleischer and Jegerlehner (FJTS) [35, 36], where we split the bare VEV into the component $v^t_{\phi_i,0}$ which satisfies the bare tadpole equation and is the proper renormalized VEV and counterterm, and an additional contribution Δv_{ϕ_i} which does not have a physical interpretation yet. So we have that

$$\left.\frac{\partial \mathcal{V}_{\text{CxSM},0}}{\partial \phi_{i,0}}\right|_{\phi_{i,0} = v^t_{\phi_i,0}} = 0\,, \qquad v_{\phi_i,0} = v^t_{\phi_i,0} + \Delta v_{\phi_i} = v_{\phi_i} + \delta v_{\phi_i} + \Delta v_{\phi_i}\,. \tag{3.50}$$

To make things clear we write the minimum conditions using the explicit dependence of the tadpole equations on the VEVs. We start with the component $v^t_{\phi_i,0}$ which, by definition, makes the tadpole equations vanish

$$T_{\phi_i,0}(v^t_{h,0}, v^t_{\sigma,0}) = 0\,, \tag{3.51}$$

which can be written explicitly as

$$-v^t_{h,0}\left(\mu^2_{\Phi,0} + \frac{1}{2}\lambda_{\Phi\sigma,0}\left(v^t_{\sigma,0}\right)^2 + \lambda_{\Phi,0}\left(v^t_{h,0}\right)^2\right) = 0\,, \tag{3.52}$$

$$-v^t_{\sigma,0}\left(\mu^2_{b,0} + \mu^2_{\sigma,0} + \lambda_{\sigma,0}\left(v^t_{\sigma,0}\right)^2 + \frac{1}{2}\lambda_{\Phi\sigma,0}\left(v^t_{h,0}\right)^2\right) = 0\,. \tag{3.53}$$

For bare VEVs $v_{\phi_i,0}$ the tadpoles equation do not vanish and there in a contribution to the 1-point function

$$\overline{T_{\phi_i}} \equiv T_{\phi_i,0}(v_{h,0}, v_{\sigma,0}) \neq 0\,, \tag{3.54}$$

where $\overline{T_{\phi_i}}$ is a compact way of writing the total contribution to the one-point functions from the tadpoles equations. Explicitly the two tadpole equations are written as

$$\overline{T_h} \equiv -v_{h,0}(\mu^2_{\Phi,0} + \frac{1}{2}\lambda_{\Phi\sigma,0}v^2_{\sigma,0} + \lambda_{\Phi,0}v^2_{h,0}) \neq 0\,, \tag{3.55}$$

$$\overline{T_\sigma} \equiv -v_{\sigma,0}(\mu^2_{b,0} + \mu^2_{\sigma,0} + \lambda_{\sigma,0}v^2_{\sigma,0} + \frac{1}{2}\lambda_{\Phi\sigma,0}v^2_{h,0}) \neq 0\,. \tag{3.56}$$

Each component of the bare VEV will give a contribution to the non-diagonal mass matrix M^2 and to the diagonal mass matrix D^2. We can split each shift to the mass matrices as

$$D^2_0 = D^2 + \delta D^2 = D^2 + \delta D^2_t + \Delta D^2\,, \tag{3.57}$$

$$M^2_0 = M^2 + \delta M^2 = M^2 + \delta M^2_t + \Delta M^2\,, \tag{3.58}$$

where $D^2_0(M^2_0)$ is the bare mass matrix, $D^2(M^2)$ is the renormalized mass matrix, $\delta D^2_t(\delta M^2_t)$ is the shift on the bare mass matrix caused by the vev shift δv_{ϕ_i}, and $\Delta D^2(\Delta M^2)$ is the shift on the bare mass matrix caused by the vev shift Δv_{ϕ_i}. The last two contributions $\delta(...)$ and $\Delta(...)$ are considered to be a next-to-leading order contribution.

To ensure that there are no 1-point functions we impose that bare tadpoles at $v_{\phi_i,0}$ must cancel against the 1-loop contributions of the tadpoles diagrams. The linear terms in the renormalized field in the potential must vanish

$$-\mathcal{V}^{\text{linear}}_{\text{CxSM, eff}} = \sum_{\phi_i}\phi_i\left(\overline{T_{\phi_i}} + T^{\text{1-loop}}_{\phi_i}\right) = 0\,. \tag{3.59}$$

The leading order term of $\overline{T_{\phi_i}}$ is zero because of Eq. 3.51. This allows us to interpret $\overline{T_{\phi_i}}$ as a counterterm [6] that cancels the 1-loop contributions of the 1-point functions. The conditions $\overline{T_{\phi_i}} = -T^{\text{1-loop}}_{\phi_i}$ can be diagrammatically represented as

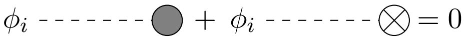

(3.60)

which means that all tadpoles, along with tadpole counterterms, vanish from the theory [7].

We still have to find a way to determine the additional VEV counterterms Δv_ϕ and understand the impact of this shift. On one hand, after writing explicitly the dependence of the $\overline{T_\phi}$ on the bare VEVs we can Taylor expand it around $v^t_{\phi,0}$, up to first order, and get

$$\overline{T_{\phi_i}} = T_{\phi_i,0}\left(v^t_{h,0} + \Delta v_h, v^t_{\sigma,0} + \Delta v_\sigma\right) \tag{3.61}$$

$$= \underbrace{T_{\phi_i,0}\left(v^t_{h,0}, v^t_{\sigma,0}\right)}_{=0\ (3.51)} + \Delta v_h \frac{\partial T_{\phi_i,0}}{\partial v_{h,0}}\bigg|_{\Delta v_{\phi_i}=0} + \Delta v_\sigma \frac{\partial T_{\phi_i,0}}{\partial v_{\sigma,0}}\bigg|_{\Delta v_{\phi_i}=0} + \mathcal{O}((\Delta v_{\phi_i})^2) \tag{3.62}$$

$$\approx \Delta v_h \frac{\partial T_{\phi_i}}{\partial v_h} + \Delta v_\sigma \frac{\partial T_{\phi_i}}{\partial v_\sigma} \tag{3.63}$$

We are allowed to make the last approximation because the shift $(\Delta v_{\phi_i})^2$ is already of second-order and only first-order contributions will survive from the tadpole derivative. On the other hand, we have that

$$\frac{\partial T_{\phi_i}}{\partial v_{\phi_j}} = -M_{ij}\,, \tag{3.64}$$

where M is the mass matrix. This allows us to relate the Δv_ϕ and $T^{\text{1-loop}}_\phi$ in a compact way

$$\begin{pmatrix} T^{\text{1-loop}}_h \\ T^{\text{1-loop}}_{\sigma_R} \end{pmatrix} = -\begin{pmatrix} \overline{T_h} \\ \overline{T_\sigma} \end{pmatrix} = M^2 \begin{pmatrix} \Delta v_h \\ \Delta v_\sigma \end{pmatrix}. \tag{3.65}$$

The appearance of the mass matrix allows us to convert all the tadpoles and VEVs shifts from the gauge basis into the mass basis, which is more suited for amplitude calculations. We can rotate the tadpole counterterm and 1-loop corrections from the gauge basis to the mass basis by using the same rotation matrix R_α

$$\begin{pmatrix} T^{\text{1-loop}}_h \\ T^{\text{1-loop}}_\sigma \end{pmatrix} = R^{-1}_\alpha \begin{pmatrix} T^{\text{1-loop}}_{h_1} \\ T^{\text{1-loop}}_{h_2} \end{pmatrix}, \quad \begin{pmatrix} \overline{T_h} \\ \overline{T_\sigma} \end{pmatrix} = R^{-1}_\alpha \begin{pmatrix} \overline{T_{h_1}} \\ \overline{T_{h_2}} \end{pmatrix}, \quad \begin{pmatrix} \Delta v_h \\ \Delta v_\sigma \end{pmatrix} \equiv R^{-1}_\alpha \begin{pmatrix} \Delta v_{h_1} \\ \Delta v_{h_2} \end{pmatrix}. \tag{3.66}$$

---

[6] Although we have call it a *tadpole counterterm* we are not renormalizing the tadpoles, we merely imposing that we are in the true vacuum.

[7] This is why we defined the self-energies without the contribution of tadpoles.

Multiplying both sides of Eq. 3.65 by the R_α matrix, which diagonalizes bare mass matrix, yields

$$\begin{pmatrix} T^{\text{1-loop}}_{h_1} \\ T^{\text{1-loop}}_{h_2} \end{pmatrix} = -\begin{pmatrix} \overline{T_{h_1}} \\ \overline{T_{h_2}} \end{pmatrix} = \begin{pmatrix} m^2_{h_1}\Delta v_{h_1} \\ m^2_{h_2}\Delta v_{h_2} \end{pmatrix} . \tag{3.67}$$

Finally we can identify that VEV shifts, in the mass basis, as a connected tadpole diagram with zero linear momentum transfer

$$\Delta v_{h_i} = \frac{1}{m^2_{h_1}} T^{\text{1-loop}}_{h_i} = i\frac{i}{-m^2_{h_i}} T^{\text{1-loop}}_{h_i} = i \left(\right. $$

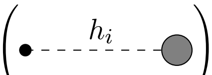

$$\left. \right) \tag{3.68}$$

We almost have the complete set of physical relations to determine δD^2. To get to the final result it is useful to use some relation between the gauge basis and mass basis in index notation. We have that the mass fields and gauge field relate as

$$h_m = R_{mn}\phi_n, \qquad \phi_n = R^{-1}_{mn} h_n = R^T_{mn} h_n = R_{nm} h_n \tag{3.69}$$

$$\implies \frac{\partial}{\partial \phi_n}(...) = \frac{\partial h_m}{\partial \phi_n}\frac{\partial}{\partial h_m}(...) = R_{mn}\frac{\partial}{\partial h_m}(...) . \tag{3.70}$$

Now we can determine the bare mass matrix counterterm, and therefore $\Delta D^2 = \overline{D^2} - D^2 - \delta D^2_t$ using Eq. 3.57. The aim is to expand the bare potential $\mathcal{L}_{\text{CxSM},0}$ calculated in the FJTS, and Taylor expand it around the bare VEV $v^t_{\phi_i,0}$[8]

$$\begin{aligned}
(D^2_0)_{ij} &= (R_0)_{im}(M^2_0)_{mn}(R^{-1}_0)_{nj} && (3.71)\\
&= -(R_0)_{im}\frac{\partial^2 \mathcal{L}^t_{\text{CxSM}}}{\partial \phi_m \partial \phi_n}(R^{-1}_0)_{nj} && (3.72)\\
&= -(R_0)_{im}\left\langle \frac{\partial^2 \mathcal{L}^t_{\text{CxSM},0}}{\partial \phi_m \partial \phi_n} + \frac{\partial^3 \mathcal{L}_{\text{CxSM}}}{\partial \phi_m \partial \phi_n \partial \phi_k}\Delta v_{\phi_k}\right\rangle (R^{-1}_0)_{nj} && (3.73)\\
&= (D^2_{t,0})_{i,j} - R_{im}R_{m\tilde{m}}R_{n\tilde{n}}R_{k\tilde{k}}R_{jn}R^{-1}_{kl}\Delta v_{h_l}\left\langle \frac{\partial^3 \mathcal{L}_{\text{CxSM}}}{\partial h_{\tilde{m}}\partial h_{\tilde{n}}\partial h_{\tilde{k}}}\right\rangle && (3.74)\\
&= (D^2_{t,0})_{i,j} - \delta_{i\tilde{m}}\delta_{j\tilde{n}}\delta_{l\tilde{k}}\Delta v_{h_l}\left\langle \frac{\partial^3 \mathcal{L}_{\text{CxSM}}}{\partial h_{\tilde{m}}\partial h_{\tilde{n}}\partial h_{\tilde{k}}}\right\rangle && (3.75)\\
&= (D^2_{t,0})_{i,j} - \left\langle \frac{\partial^3 \mathcal{L}_{\text{CxSM}}}{\partial h_i \partial h_j \partial h_l}\right\rangle \Delta v_{h_l} && (3.76)\\
&= (D^2_{t,0})_{i,j} - \lambda_{h_i h_j h_l}\Delta v_{h_l} && (3.77)
\end{aligned}$$

where δ_{ij} is the Kronecker delta, $\lambda_{h_i h_j h_l}$ is the trilinear coupling between particles h_i, h_j and h_l, and $D_{t,0}$ is the bare mass matrix with $\Delta v_{\phi_i} = 0$. $\mathcal{L}^t_{\text{CxSM},0}$ is the bare Lagrangian with $\Delta v_{\phi_i} = 0$. Here we see what happens to the mass matrix counterterm - it is shifted by the contributions to the tadpole diagrams. Analysing Eq. 3.48 and Eq. 3.54 we can conclude that $D^2_{t,0}$ is diagonal

---

[8] Differentiating in $v_{\phi_{i,0}}$ is the same as differentiating in ϕ_i because the Lagrangian is a function of $(v_{\phi_{i,0}} + \phi_i)$.

$$D^2_{t,0} = \underbrace{\begin{pmatrix} m^2_{h_1} & 0 \\ 0 & m^2_{h_2} \end{pmatrix}}_{D^2} + \underbrace{\begin{pmatrix} \delta m^2_{h_1} & 0 \\ 0 & \delta m^2_{h_2} \end{pmatrix}}_{\delta D^2_t} , \tag{3.78}$$

and the the VEVs shift Δv_{h_i} create a contribution that can be described by tadpole Feynman diagrams

$$(D^2_0)_{ij} = (D^2_{t,0})_{ij} + i \sum_{h_l} \left(\quad \right) . \tag{3.79}$$

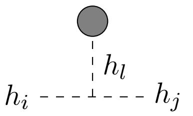

We can now go back to the renormalized self-energy, Eq. 3.41 in the on-shell renormalization scheme section, and see the effect of the VEV shifts Δv_{h_i} in the FJTS

$$\left[\hat{\Sigma}_h(p^2)\right]_{ij} = \left[\Sigma_h(p^2)\right]_{ij} - \left[\delta D^2_t\right]_{ij} + \lambda_{h_i h_j h_l} \Delta v_{h_l} + (...) \tag{3.80}$$

The contribution from the Δv_{h_l}, in the FJTS, creates additional self-energy like diagrams that can be included in the definition of the self-energies making the mass matrix counterterm diagonal. We redefine the self-energies as

$$i\Sigma^{\text{tad}}_{h_i h_j}(p^2) = i\Sigma_{h_i h_j}(p^2) + i\lambda_{h_i h_j h_l} \Delta v_{h_l} . \tag{3.81}$$

where the the subscript *tad* indicates that we also take the tadpole contribution to the self-energy into account. Diagrammatically, the self-energies with tadpoles can be drawn as

$$i\Sigma^{\text{tad}}_{h_i h_j}(p^2) =$$

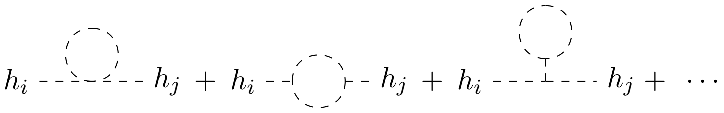

Figure 3.6: One-particle irreducible diagrams, also called self-energies. On this definition of self-energy we include the tadpoles.

The FJTS also affects the trilinear couplings. Consider the definition of a bare trilinear coupling $\lambda_{h_i h_j h_k,0}$

$$\lambda_{h_i h_j h_k,0} = \langle \partial_i \partial_j \partial_k \mathcal{L}_{\text{CxSM},0} \rangle \tag{3.82}$$

$$= \left\langle \partial_i \partial_j \partial_k \mathcal{L}^t_{\text{CxSM},0} \right\rangle + \Delta v_{h_m} \left\langle \partial_i \partial_j \partial_k \partial_m \mathcal{L}_{\text{CxSM}} \right\rangle \tag{3.83}$$

$$= \lambda_{h_i h_j h_k} + \delta\lambda_{h_i h_j h_k} + \Delta v_{h_m} \lambda_{h_i h_j h_k h_m} . \tag{3.84}$$

where $\partial_i \equiv \frac{\partial}{\partial h_i}$. We can see that, in the FJTS, the VEV shifts Δv_{ϕ_i} represent an additional contribution to the bare trilinear couplings and create additional tadpole diagrams [9] that have to be included as well

$$i\lambda_{h_ih_jh_k,0} =$$

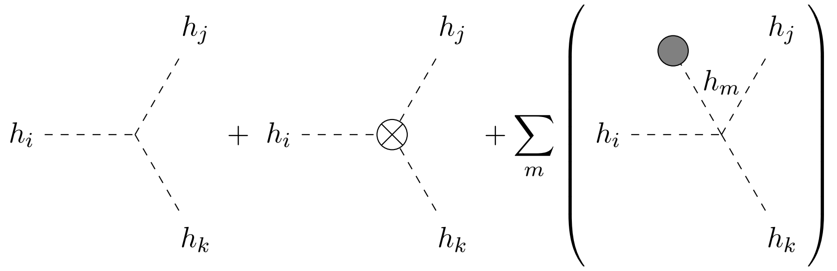

(3.85)

In this method, by imposing that we are in the true VEV, all 1-point functions are zero in the renormalized potential, and we found a way to determine the counterterm of the mass matrix by redefining the self-energies. We can apply again the on-shell renormalization conditions stated in the last section, and find that the field renormalization constants and mass counterterms

$$\delta Z_{h_1h_1} = -\operatorname{Re}\left[\frac{\partial\Sigma^{\text{tad}}_{h_1h_1}\left(p^2\right)}{\partial p^2}\right]_{p^2=m^2_{h_1}} \tag{3.86}$$

$$\delta Z_{h_1h_2} = \frac{2}{m^2_{h_1}-m^2_{h_2}}\operatorname{Re}\left[\Sigma^{\text{tad}}_{h_1h_2}\left(m^2_{h_2}\right)\right] \tag{3.87}$$

$$\delta Z_{h_2h_1} = \frac{2}{m^2_{h_2}-m^2_{h_1}}\operatorname{Re}\left[\Sigma^{\text{tad}}_{h_1h_2}\left(m^2_{h_1}\right)\right] \tag{3.88}$$

$$\delta Z_{h_2h_2} = -\operatorname{Re}\left[\frac{\partial\Sigma^{\text{tad}}_{h_2h_2}\left(p^2\right)}{\partial p^2}\right]_{p^2=m^2_{h_2}} \tag{3.89}$$

$$\delta m^2_{h_1} = \operatorname{Re}\left[\Sigma^{\text{tad}}_{h_1h_1}\left(m^2_{h_1}\right)\right] \tag{3.90}$$

$$\delta m^2_{h_2} = \operatorname{Re}\left[\Sigma^{\text{tad}}_{h_2h_2}\left(m^2_{h_2}\right)\right] \tag{3.91}$$

The mass counterterms are gauge independent by construction in this scheme but the same is not true in general for the field renormalization constants. This is not a problem because the field renormalization constants are not physical observables. Still, care should be taken if they are used to define other renormalization constants as will be discussed later.

3.9 Leg Corrections and Leg counterterms

Now that we found how to describe the field renormalization in the on-shell scheme we are going to take a closer look at what happens between the leg corrections and the corresponding leg counterterm.

---

[9] Assuming that the quadrilinear coupling $\lambda_{h_ih_jh_kh_m}$ exists

We are going to explore the case without mixing, which corresponds to any of the dark matter legs.

$$i\mathcal{A}^{\text{leg, 3}} + i\mathcal{A}^{\text{leg CT, 3}} =$$

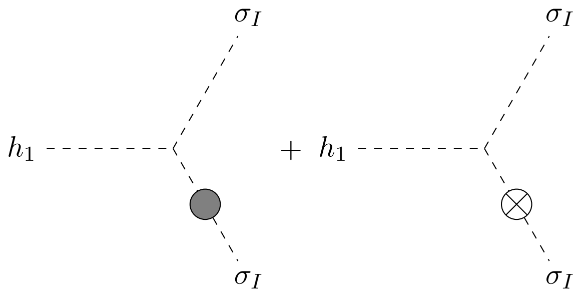

(3.92)

The total amplitude is given by the self-energy like terms on the left and the 2-point function counterterms of the dark matter particle on the right. It can be written as

$$i\mathcal{A}^{\text{leg, 3}} = i\lambda_{h_1\sigma_I\sigma_I}\frac{i}{p^2 - m^2_{\sigma_I}}\Sigma^{\text{tad}}_{\sigma_I\sigma_I}(p^2)\,, \tag{3.93}$$

$$i\mathcal{A}^{\text{leg CT, 3}} = i\lambda_{h_1\sigma_I\sigma_I}\frac{i}{p^2 - m^2_{\sigma_I}}\left[(p^2 - m^2_{\sigma_I})\delta Z_{\sigma_I} + \delta m^2_{\sigma_I}\right]\,. \tag{3.94}$$

When we apply the on-shell renormalization conditions and substitute in the counterterms we get

$$i\mathcal{A}^{\text{leg, 3}} + i\mathcal{A}^{\text{leg CT, 3}} = -\lambda_{h_1\sigma_I\sigma_I}\left[\underbrace{\frac{\Sigma^{\text{tad}}_{\sigma_I\sigma_I}(p^2) - \Sigma^{\text{tad}}_{\sigma_I\sigma_I}(m^2_{\sigma_I})}{p^2 - m^2_{\sigma_I}}}_{\approx\frac{d\Sigma^{\text{tad}}_{\sigma_I\sigma_I}(p^2)}{dp^2}} - \frac{d\Sigma^{\text{tad}}_{\sigma_I\sigma_I}(p^2)}{dp^2}\bigg|_{p^2=m^2_{\sigma_I}}\right] \tag{3.95}$$

$$\overset{p^2\to m^2_{\sigma_I}}{=} 0,\,. \tag{3.96}$$

In the on-shell renormalization scheme, the leg corrections and leg counterterms cancel against each other. This result also applies for the case with mixing so all the leg corrections and counterterms cancel. This makes the calculations simpler because when we want to calculate the 1-loop correction to a process we already know that there will be no corrections to the external legs and we can only focus on the structure of the vertex at 1-loop. This is valid for the on-shell renormalization scheme.

3.10 Renormalization of α in the KOSY Scheme

For the renormalization, we are going to use the method developed by Kanemura, Okada, Senaha and Yuan [37] which we denote as the *KOSY scheme*. The method consists of using the basis transformation Eq. 2.26 to link the two bare bases of fields using the bare rotation matrix

$$\begin{pmatrix} h_1 \\ h_2 \end{pmatrix}_0 = R_{\alpha,0}\begin{pmatrix} h \\ \sigma_R \end{pmatrix}_0\,, \tag{3.97}$$

where $R_{\alpha,0}$ is the bare rotation matrix which can be written as

$$R_{\alpha,0} = R(\alpha_0) = R(\alpha + \delta\alpha) = R(\alpha)R(\delta\alpha) = R(\delta\alpha)R(\alpha)\,. \tag{3.98}$$

Since we are only interested in next to leading order contributions, we can expand the correction to the rotation matrix, $R(\delta\alpha)$, as

$$R(\delta\alpha) = \begin{pmatrix} \cos(\delta\alpha) & \sin(\delta\alpha) \\ -\sin(\delta\alpha) & \cos(\delta\alpha) \end{pmatrix} \approx \begin{pmatrix} 1 & \delta\alpha \\ -\delta\alpha & 1 \end{pmatrix}. \tag{3.99}$$

Using appropriate base transformations, it is possible to relate the bare mass field and the mass field using the bare rotation matrix

$$\begin{pmatrix} h_1 \\ h_2 \end{pmatrix}_0 = R_{\alpha,0} \begin{pmatrix} h \\ \sigma_R \end{pmatrix}_0 = R_{\delta\alpha} R_\alpha \sqrt{Z_\phi} R_\alpha^T R_\alpha \begin{pmatrix} h \\ \sigma_R \end{pmatrix} \equiv \sqrt{Z_h^{\text{KOSY}}} \begin{pmatrix} h_1 \\ h_2 \end{pmatrix}, \tag{3.100}$$

where $\sqrt{Z_\phi}$ is a real symmetric matrix that relates the bare field and renormalized field in the gauge basis. Since $\sqrt{Z_\phi}$ is symmetric then $R_\alpha \sqrt{Z_\phi} R_\alpha^{-1}$ is also symmetric and can be parametrized as

$$\left(R_\alpha \sqrt{Z_\phi} R_\alpha^{-1}\right)_{ii} = 1 + \frac{\delta Z_{ii}}{2}\,, \tag{3.101}$$

$$\left(R_\alpha \sqrt{Z_\phi} R_\alpha^{-1}\right)_{ij} = \delta C_{h_2}, \quad i \neq j\,, \tag{3.102}$$

which allow us to write $\sqrt{Z_h^{\text{KOSY}}}$ as

$$R_{\delta\alpha} R_\alpha \sqrt{Z_\phi} R_\alpha^{-1} = \sqrt{Z_h^{\text{KOSY}}} \approx \begin{pmatrix} 1 + \frac{\delta Z_{h_1 h_1}}{2} & \delta C_{h_2} + \delta\alpha \\ \delta C_{h_2} - \delta\alpha & 1 + \frac{\delta Z_{h_2 h_2}}{2} \end{pmatrix}. \tag{3.103}$$

The matrix $\sqrt{Z_h^{\text{KOSY}}}$ has already been defined in Eq. 3.23, so the two must be equal

$$\sqrt{Z_h^{\text{KOSY}}} = \sqrt{Z_h}\,. \tag{3.104}$$

If we compare both matrices term by term we can see that the off-diagonal of Eq. 3.23 can be arranged in a way to determine the α counterterm

$$\delta\alpha = \frac{\left(\sqrt{Z_h^{\text{KOSY}}}\right)_{12} - \left(\sqrt{Z_h^{\text{KOSY}}}\right)_{21}}{2} = \frac{(\sqrt{Z_h})_{12} - (\sqrt{Z_h})_{21}}{2}\,. \tag{3.105}$$

From last section, we already know how to write the field renormalization constants as a function of the self-energies with tadpoles. The α counterterm is

$$\delta\alpha = \frac{1}{2\left(m_{h_1}^2 - m_{h_2}^2\right)} \operatorname{Re}\left[\Sigma_{h_1 h_2}^{\text{tad}}\left(m_{h_1}^2\right) + \Sigma_{h_1 h_2}^{\text{tad}}\left(m_{h_2}^2\right)\right]. \tag{3.106}$$

Unfortunately, this method has one major issue. When we calculate the α counterterm using this method we get a gauge dependent counterterm. This would not be a problem if there were another counterterm that precisely canceled the gauge dependent coming from $\delta\alpha$. This is not the case, the gauge dependence does not cancel and we have that

$$\frac{d\Gamma}{d\xi} \neq 0\,, \tag{3.107}$$

where Γ is the decay width. This result is unphysical. Since the cancellation does not happen we have to find some way to remove the gauge dependence. To do that we are going to use the Pinch technique [38]. This method consists of extracting the self-energy like terms of an auxiliary process and using them to correct the self-energies. This correction cancels the gauge dependence of the self-energy itself and renders the α counterterm gauge independent as well. More details on how to find those corrections are given in the Appendix A. We calculate the new self-energies, which we shall call *pinched self-energies*, as

$$\begin{aligned} i\Sigma^{\text{pinched}}_{h_ih_j}(p^2) &= i\Sigma^{\text{tad}}_{h_ih_j}(p^2)\Big|_{\xi=1} \\ &\quad - \frac{ig^2}{32\pi^2 c_w^2}\left(p^2 - \frac{m^2_{h_i}+m^2_{h_j}}{2}\right)\mathcal{O}_{h_ih_j}B_0(p^2, m_Z^2, m_Z^2) \\ &\quad - \frac{ig^2}{16\pi^2}\left(p^2 - \frac{m^2_{h_i}+m^2_{h_j}}{2}\right)\mathcal{O}_{h_ih_j}B_0(p^2, m_W^2, m_W^2)\,. \end{aligned} \tag{3.108}$$

Note that $\xi = 1$, i.e. $\xi_W = \xi_Z = \xi_A = 1$, does not mean that we are in the Feynman gauge, it is just a way to write the result in comparison with the one obtained if we were choosing that gauge. We have also introduced the quantity $\mathcal{O}_{h_ih_j}$

$$\mathcal{O}_{h_ih_j} = \begin{cases} \cos^2(\alpha), & h_i = h_j = h_1 \\ \sin^2(\alpha), & h_i = h_j = h_2 \\ -\sin(\alpha)\cos(\alpha), & h_i \neq h_j \end{cases} \tag{3.109}$$

The pinched self-energies are gauge independent by design, even before setting p^2 to the mass or any other value. This allows for some freedom on choosing p^2. To write the counterterm for α we can use the on-shell approach and use the pinched self-energies in the expression for the counterterm

$$\delta\alpha^{\text{OS}} = \frac{1}{2\left(m^2_{h_1} - m^2_{h_2}\right)}\,\text{Re}\left[\Sigma^{\text{pinched}}_{h_1h_2}\left(m^2_{h_1}\right) + \Sigma^{\text{pinched}}_{h_1h_2}\left(m^2_{h_2}\right)\right] \tag{3.110}$$

This choice for the momentum in not unique [39], it is also possible to set the momentum p^2 to $p{\star}^2$ where $p{\star}^2$ is the average squared mass

$$p{\star}^2 = \frac{m^2_{h_i}+m^2_{h_j}}{2}\,. \tag{3.111}$$

which simplifies the correction Eq. 3.108 to

$$\Sigma^{\text{pinched}}_{h_i h_j}(p\star^2) = \Sigma^{\text{tad}}_{h_i h_j}(p\star^2)\Big|_{\xi=1}, \tag{3.112}$$

and so we write the counterterm for α in the $p\star$ scheme as

$$\delta\alpha^\star = \frac{1}{\left(m^2_{h_1} - m^2_{h_2}\right)} \operatorname{Re}\left[\Sigma^{\text{tad}}_{h_1 h_2}\left(\frac{m^2_{h_1} + m^2_{h_2}}{2}\right)\right]\Bigg|_{\xi=1}. \tag{3.113}$$

The correction done in Eq. 3.108 to the self-energy, in the on-shell scheme, changes the divergent structure of the self-energy

$$\Sigma^{\text{pinched}}_{h_i h_j}(m^2_{h_j}) - \Sigma^{\text{tad}}_{h_i h_j}(m^2_{h_j})\Big|_{\xi=1} \propto \frac{1}{\epsilon}\left(m^2_{h_i} - m^2_{h_j}\right) + \text{finite parts}. \tag{3.114}$$

This change on the divergent structure is cancelled by the counterterm self-energy so that the correction does not change the divergent part of the $\delta\alpha$.

3.11 Renormalization of v_σ scalar VEV

While discussing the cancelation of the 1-point function using the Fleischer-Jegerlehner scheme, we split the bare VEV into

$$v_{\phi_i} = v_{\phi_i} + \delta v_{\phi_i} + \Delta v_{\phi_i}, \tag{3.115}$$

$$v^t_{\phi_i,0} = v_{\phi_i} + \delta v_{\phi_i}, \qquad \phi_i = h, \sigma_R\,. \tag{3.116}$$

We have seen that the Δv_{h_i} (mass basis) are represented by tadpole diagrams with h_i 1-point functions at 1-loop, which can be relocated into the self-energies and vertices. Nevertheless, we still have not dealt with the renormalization of the VEVs. For our process, Higgs decay into dark matter ($h_1 \to \sigma_I\sigma_I$), the trilinear coupling $\lambda_{h_1\sigma_I\sigma_I}$ does not depend on v_h. Therefore, the vertex counterterm will not depend on δv_h so we do not have to renormalize v_h [10], only v_σ has to be renormalized. The renormalization of v_σ is done using the *process dependent renormalization scheme*. This scheme takes an auxiliary process and imposes that δv_σ is such that there is no 1-loop correction, i.e.the leading order and next to leading order decay widths are the same. In this work we are going to use the decay process $h_2 \to \sigma_I\sigma_I$ as our auxiliary process.

$$\Gamma^{\text{LO}}_{h_2\sigma_I\sigma_I} = \Gamma^{\text{NLO}}_{h_2\sigma_I\sigma_I} \tag{3.117}$$

$$\Leftrightarrow \left|\mathcal{A}^{\text{LO}}_{h_2\sigma_I\sigma_I}\right|^2 = \left|\mathcal{A}^{\text{NLO}}_{h_2\sigma_I\sigma_I}\right|^2 \tag{3.118}$$

$$\Leftrightarrow \left|\mathcal{A}^{\text{LO}}_{h_2\sigma_I\sigma_I}\right|^2 \approx \left|\mathcal{A}^{\text{LO}}_{h_2\sigma_I\sigma_I}\right|^2 + 2\operatorname{Re}[(\mathcal{A}^{\text{LO}}_{h_2\sigma_I\sigma_I})^*\mathcal{A}^{\text{1-loop}}_{h_2\sigma_I\sigma_I}]\,. \tag{3.119}$$

---

[10] In fact, v_h is not usually chosen as an input parameter of the theory. It is usually replaced by the W boson mass.

The expression for $\mathcal{A}^{\text{LO}}_{h_2\sigma_I\sigma_I}$ is real

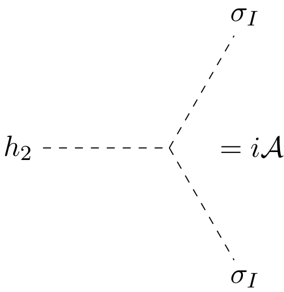

$$= i\mathcal{A}^{\text{LO}}_{h_2\sigma_I\sigma_I} = -i\frac{m^2_{h_2}\cos(\alpha)}{v_\sigma} \equiv i\lambda_{h_2\sigma_I\sigma_I} \,.$$

Therefore Eq. 3.119 is equivalent to the vanishing of the real part of $\mathcal{A}^{\text{1-loop}}_{h_2\sigma_I\sigma_I}$

$$\text{Re}\left[\mathcal{A}^{\text{1-loop}}_{h_2\sigma_I\sigma_I}\right] = 0 \,. \tag{3.120}$$

We can easily solve for δv_σ. The final results yields

$$\begin{aligned}\delta v_\sigma = -\frac{v_\sigma^2}{m^2_{h_2}\cos(\alpha)}\,\text{Re}\Big[&\mathcal{A}^{\text{VC}} + \mathcal{A}^{\text{CT}}\big|_{\delta v_\sigma = 0} \\ &+ \mathcal{A}^{\text{leg, 1}} + \mathcal{A}^{\text{leg, 2}} + \mathcal{A}^{\text{leg, 3}} + \mathcal{A}^{\text{leg CT, 1}} + \mathcal{A}^{\text{leg CT, 2}} + \mathcal{A}^{\text{leg CT, 3}}\Big]_{h_2\sigma_I\sigma_I} \,.\end{aligned} \tag{3.121}$$

If we take the on-shell approach and set the incoming momentum $p^2_{h_2}$ to $m^2_{h_2}$ and both outgoing momenta to $m^2_{\sigma_I}$ Eq. 3.121 simplifies to

$$\delta v_\sigma^{\text{OS}} = -\frac{v_\sigma^2}{m^2_{h_2}\cos(\alpha)}\,\text{Re}\left[\mathcal{A}^{\text{VC}} + \mathcal{A}^{\text{CT}}\big|_{\delta v_\sigma = 0}\right] . \tag{3.122}$$

This approach has a drawback, however. When using the process dependent renormalization scheme we are implicitly adding constraints on the parameter space because for the auxiliary process to be kinematically viable we have to impose that $m_{h_2} > 2m_{\sigma_I}$.

To go around this additional constraint we can use the *zero external momentum* (ZEM) scheme, proposed in [40]. In this scheme, we set the incoming momentum and the outgoing momenta to zero. This means that the leg corrections and leg counterterms in Eq. 3.121 do not cancel and have to be included. In the ZEM scheme there is no constraint on the masses. Unfortunately we obtain a gauge dependent counterterm. In the on-shell approach, the gauge dependency of the vertex correction cancels with the gauge dependency of the vertex counterterm.That does not happen in the ZEM scheme because the vertex correction is gauge independent by itself and cannot cancel the gauge dependency coming from the counterterms. The gauge dependence has its origin in the field renormalization constants as previously discussed. To circumvent this issue we used the pinched self-energies on the definitions of the field renormalization constants. So we have that

$$\begin{aligned}\delta v_\sigma^{\text{ZEM}} = &-\frac{v_\sigma^2}{m_{h_2}^2\cos(\alpha)}\,\text{Re}\Big[\mathcal{A}^{\text{VC}} + \mathcal{A}^{\text{CT}}\big|_{\delta v_\sigma=0} \\ &+\mathcal{A}^{\text{leg, 1}} + \mathcal{A}^{\text{leg, 2}} + \mathcal{A}^{\text{leg, 3}} + \mathcal{A}^{\text{leg CT, 1}} + \mathcal{A}^{\text{leg CT, 2}} + \mathcal{A}^{\text{leg CT, 3}}\Big]_{h_2\sigma_I\sigma_I,\, p_i^2=0}\end{aligned} \tag{3.123}$$

where the field renormalization constants in $\mathcal{A}^{\text{CT}}$ and $\mathcal{A}^{\text{leg, CT, i}}$ are redefined as[11]

$$\delta Z_{\sigma_I} \to \delta Z_{\sigma_I}^{\text{pinched}} \tag{3.124}$$

$$\delta Z_{h_i h_j} \to \delta Z_{h_i h_j}^{\text{pinched}} \tag{3.125}$$

This way we get a finite and gauge independent result. This concludes the renormalization of the model. In the next chapter we discuss the results for the decay width.

---

[11] Only for the mixing angle counterterm in the ZEM scheme.

Chapter 4

Results and Discussion

4.1 Decay widths of $h_1 \to \sigma_I\sigma_I$ at NLO

We can now calculate the decay width in the different proposed schemes at NLO. As previously stated the vertex correction $\mathcal{A}^{\text{VC}}_{h_1\sigma_I\sigma_I}$ are generated with `FeynArts` are are written as functions of the Passarino-Veltman using `FeynCalc`. The vertex correction are given by the following diagrams... To calculate the 1-loop contribution to the amplitude we also need the vertex counterterm

$$\begin{aligned} i\mathcal{A}^{\text{CT}}_{h_1\sigma_I\sigma_I} &= i\lambda_{h_1\sigma_I\sigma_I}\left(\frac{1}{2}\delta Z_{h_1h_1} + \delta Z_{\sigma_I\sigma_I}\right) + i\lambda_{h_2\sigma_I\sigma_I}\left(\frac{1}{2}\delta Z_{h_2h_1}\right) \\ &+ \frac{i}{v_\sigma}\left[\frac{\delta v_\sigma}{v_\sigma}m^2_{h_1}s_\alpha - \delta\alpha m^2_{h_1}c_\alpha - \delta m^2_{h_1}c_\alpha\right] \end{aligned} \tag{4.1}$$

We will perform the calculation in four renormalization schemes, two for $\delta\alpha$ and two for δv_σ. For this reason, we introduce the following notation: the first entry is the renormalization scheme for the mixing angle and the second entry is the renormalization scheme for δv_σ. They are summarized in table 4.1.

	δ**v**$_\sigma$**-OS**	δ**v**$_\sigma$**-ZEM**
$\delta\alpha$**-OS**	OS-OS	OS-ZEM
$\delta\alpha$**-p**$\star$	$p\star$-OS	$p\star$-ZEM

Table 4.1: The four possible choices of renormalization schemes: two for the δv_σ and two for $\delta\alpha$.

To calculate the decay widths we have to use experimental data, which is taken from Particle Data Group (PDG)[3].

Parameter	**Value [GeV]**	**Parameter**	**Value [GeV]**
v_h	246.22	m_t	172.76
m_{h_1}	125.1	m_b	4.18
m_Z	91.1876	m_τ	1.77686
m_W	80.379		

Table 4.2: Experimental values for the Higgs VEV v_h and particle masses of the SM. Due to their low mass we neglected the contribution of light quarks and light fermions. This set of experimental values is complete in the sense that one can derive the electric coupling, the $SU(2)_L$ coupling, Weinberg angle, etc, can be extrapolated from them using the expressions found in section 2.3.

We are still missing the parameters for the added parts of the scalar potential. Since we hypothesised this model there is no direct experimental data for these parameters except constraints coming from theory and indirect experimental bounds. We therefore check if a set of parameters obey the imposed theoretical and experimental constraints. To that end we are going to perform randoms scans in the parameters space and these constraints are going to be verified using the `C++` package `ScannerS`. As discussed, from the theory side it checks for perturbativity, boundedness from below and that the tree level minimum is global minimum and therefore stable[1]. The important experimental constraints that `ScannerS` checks are the ones related to Higgs data. First, that the SM-like Higgs couplings, $h_{125}(\equiv h_1)$, to the remaining SM particles are within the experimental error. Second, that the Higgs searches for a new scalar are taken into account. Regarding dark matter we consider the bounds from direct detection and that the calculated relic density of σ_I is less than the energy density of dark matter Ω_{DM} measured by Planck [2]. All plots were done with a sample of a sample of 100 000 point generated with `ScannerS` that pass all constraints. We neglected points with $|m_{h_1} - m_{h_2}| < 2$ GeV.

Parameter	**Values**	**Parameter**	**Values**
m_{h_2}	[30, 1000] GeV	v_σ	[1, 1000] GeV
m_{σ_I}	[10, 62.55] GeV	α	$\left[-\frac{\pi}{2}, \frac{\pi}{2}\right]$

Table 4.3: Allowed parameter space of the model in the $m_{\sigma_I} - m_{h_2}$ plane. In the left panel $m_{h_1} < m_{h_2}$ and in the right panel $m_{h_1} > m_{h_2}$. The upper bound of m_{σ_I} is 62.55 GeV because is required that $m_{h_1} > 2m_{\sigma_I}$ for the process $h_1 \to \sigma_I\sigma_I$ to be kinetimatically allowed.

In Fig. 4.1 we plot the allowed parameter space for the dark matter particle mass m_{σ_I} and the mass of the second Higgs particle m_{h_2}. In both plots, the blue points are those above the threshold, $m_{h_2} > 2m_{\sigma_I}$, and the orange points are the ones below the threshold, that is $m_{h_2} < 2m_{\sigma_I}$. On the left panel we are in the scenario of light Higgs, i.e. $m_{h_1} < m_{h_2}$. The right panel shows the scenario $m_{h_1} > m_{h_2}$. We can

---

[1] Or a local minimum but stable compared to the age of the Universe

[2] This means that other particles can contribute to the DM relic density.

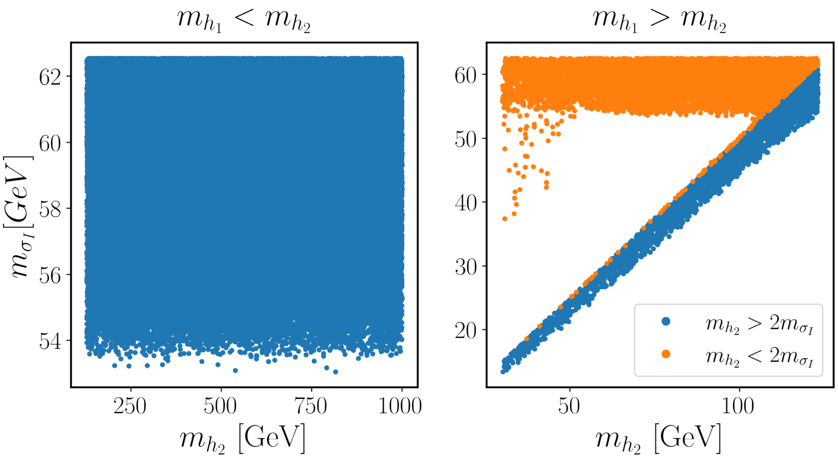

Figure 4.1: Scatter plot of the dark particle mass m_{σ_I} compared to the seconds Higgs mass m_{h_2}. In blue are the points above mass threshold and in orange are the point below mass threshold.

see that the parameter space of m_{h_2} is completely unconstrained while the dark matter mass is between 54 GeV and 62.55 GeV $= \frac{m_{h_1}}{2}$. The the heavy Higgs scenario there are two clear regions: one where the m_{h_2} and m_{σ_I} are tightly correlated and another region where m_{h_2} spans the all parameter space and the dark matter particle mass is around 60 GeV. The cause for the shape of this scatter plot, as well as the non existence of point for α around 0, are the dark matter constraints - these points produce relic densities too high compared to the experimental value..

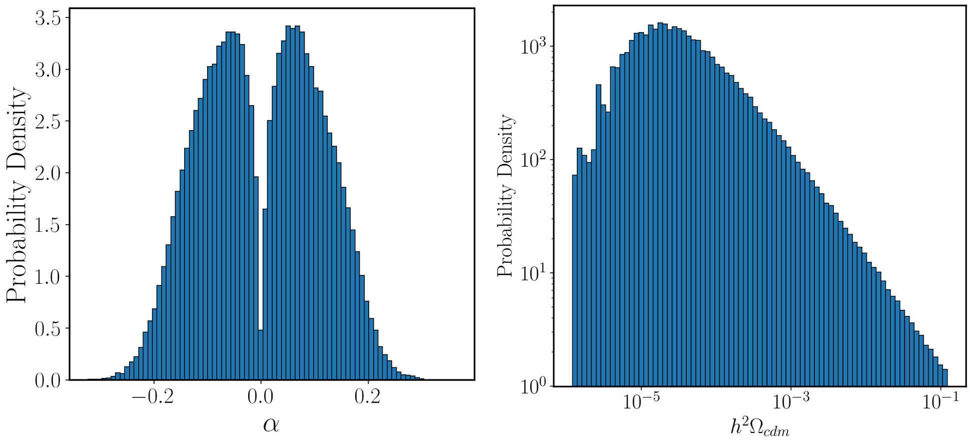

Figure 4.2: Left: histogram for the mixing angle α. Right: histogram of $h^2\Omega_{cdm}$

In the left panel of Fig. 4.2 we show the normalized distribution of the mixing angle α. First we see that the angle is constrained in absolute value to be $|\alpha| < 0.3$. This is a consequence of imposing experimental constraints of the coupling with the remaining SM particles. SM particles since these couplings are all modified by the same factor $\cos\alpha$ in the CxSM. Second the annihilation cross section that is responsible for the DM relic density is proportional to $\cos\alpha\ \sin\alpha$ and therefore when $\alpha = 0$ this cross section is zero and the relic density becomes too large compared to experimental measured value. In the right panel we present a histogram for $h^2\Omega_{cdm}$. Here we can see that most of the allowed points are below the relic density. Still we found about 800 points that are below 2σ and above 5σ of the central value.

In the left panel of Fig. 4.3 we show a scatter plot for the scalar VEV v_σ as a function of the mixing angle α. Just as in Fig. 4.2, there is a small interval around $\alpha \sim 0$ that is not allowed by experimental data, in particular by the DM relic density measurement. In the right panel we now show v_σ as a function of the DM particle mass m_{σ_I}. We conclude from both plots that all the parameter space is accessible in those variables.

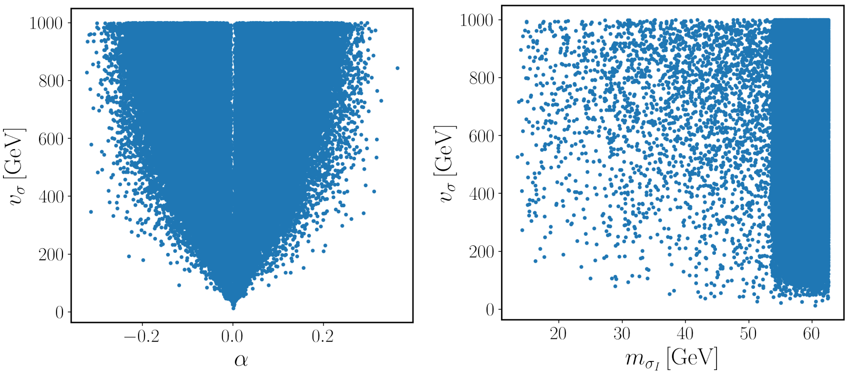

Figure 4.3: Scatter plot of the scalar VEV v_σ as a function of mixing angle α. Scatter plot of the scalar VEV v_σ as a function of the DM particle mass m_{σ_I}.

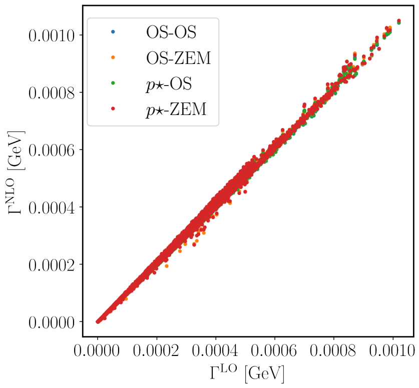

Figure 4.4: Plot of the next-to-leading order amplitude Γ^{NLO} as a function of Γ^{LO}. The different colours identify the different renormalization schemes that we can chose.

In Fig. 4.4 we plot the NLO decay width as a function of the LO one. There is a massive overlap

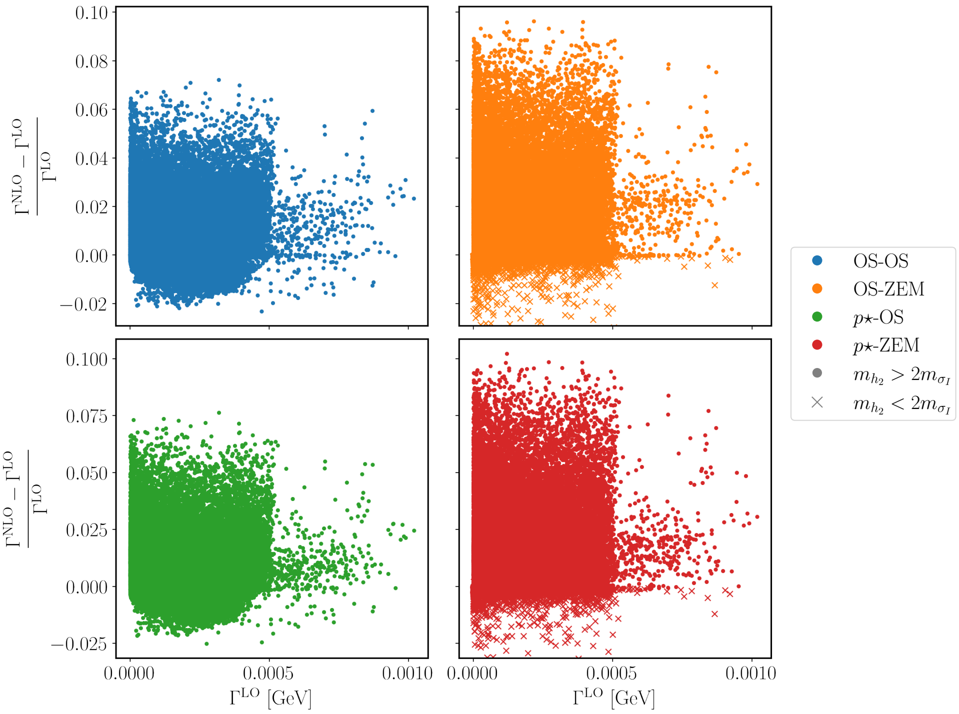

Figure 4.5: Relative difference of the next to leading order decay width. The different colours identify the different renormalization schemes that we can chose. The marker × identifies point below the mass threshold, with $m_{h_2} < 2m_{\sigma_I}$, and therefore can only be calculated using the ZEM scheme. The marker • identifies any other point.

between the points from different renormalization schemes. This happens because the corrections are quite small in all scheme.

In Fig. 4.5 we now show the relative difference between the NLO and LO width as a function of the LO one in the different renormalization schemes. There are two types of markers, the marker × identifies the points with $m_{h_2} < 2m_{\sigma_I}$ and therefore, can only be calculated using the ZEM scheme. The marker • identifies any other point not obeying this kinematical constraint for the OS process dependent renormalization scheme for δv_σ. Looking at both plots on the left, which are the ones where the OS scheme was applied for δv_σ, we can see that the corrections are quite small: the maximum relative difference is about 8% above and about 2% below the leading order decay width. For the plots on the right the corrections are somewhat larger even for points above the mass threshold, i.e. $m_{h_2} > 2m_{\sigma_I}$, showing that the ZEM scheme is less stable.

In Fig. 4.6 we show the relative difference between the NLO and LO width as a function of the LO one, but now only for the points below the mass threshold. We note that the corrections decrease the LO width, except for a few spurious points slightly above zero. The corrections are larger and can reach 50%

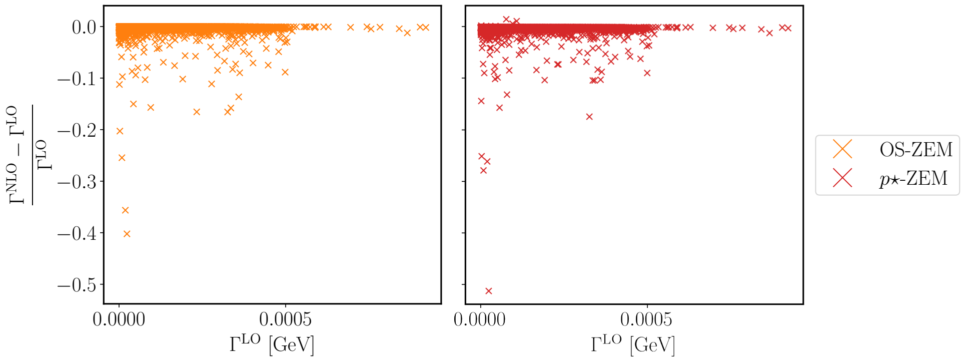

Figure 4.6: Relative difference of the next to leading order decay width for point below the mass threshold, $m_{h_2} < 2m_{\sigma_I}$. The two different colour identify the possible renormalization scheme for $\delta\alpha$.

in the low LO width region. As we approach the experimental bound the corrections are well below 10%.

We will now try to understand how these relative corrections vary with the input parameters. We choose a point, at random, that obeys all experimental constraints imposed by `ScannerS` and vary one parameter at a time while keeping the others fixed. We will not impose any theoretical nor experimental constraints on the new points because we are only interested in the effect that each parameter has in the NLO correction. The central values for the initial parameter point are given in table 4.4. We have calculated 500 equally spaced points for each parameter, with the other parameters set at their central values.

Parameter	**Value**	**Parameter**	**Value**
m_{h_2}	576.80 GeV	v_σ	969.14 GeV
m_{σ_I}	60.06 GeV	α	-0.1508

Table 4.4: Input values for the parameters the point used to scan the dependence of each parameter on the NLO decay width.

In the left panel of Fig. 4.7 we varied the mass m_{h_2} in the interval $[30,\ 1000]$ and plotted the relative width difference. There are two different behaviours which seem to be determined by the renormalization of α and two possible choices. Aside from the fact that we see the thresholds of the Passarino-Veltman functions the corrections grow with m_{h_2} and then decrease for larger values of the mass. The corrections seem to behave accordingly mainly to the choice of the renormalization for α but for larger masses it is the renormalization of v_σ that takes control. In the right panel of Fig. 4.7 we now plot the relative width difference as a function of the DM mass m_{σ_I} which is sampled in the interval $[10,\ 62.55]$. The relative difference is very stable with a slight increase with the mass that reaches a maximum of only 0.1%. We can also see that, while there is a noticeable difference between the renormalization scheme for α, it is the scalar VEV renormalization scheme that has the biggest impact on the relative difference.

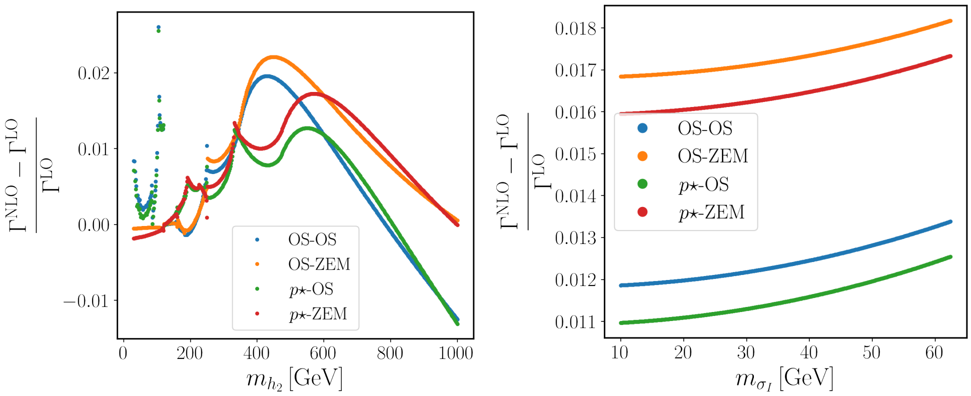

Figure 4.7: Relative difference of the width as a function of m_{h_2} (left) and as a function of DM particle mass m_{σ_I} (right). We started with a point, that verified all theoretical and experimental constraints, and varied the mass m_{h_2} in the interval $[30,\ 1000]$ GeV (left) and varied the DM particle mass m_{σ_I} in the interval $[10,\ 62.55]$ GeV.

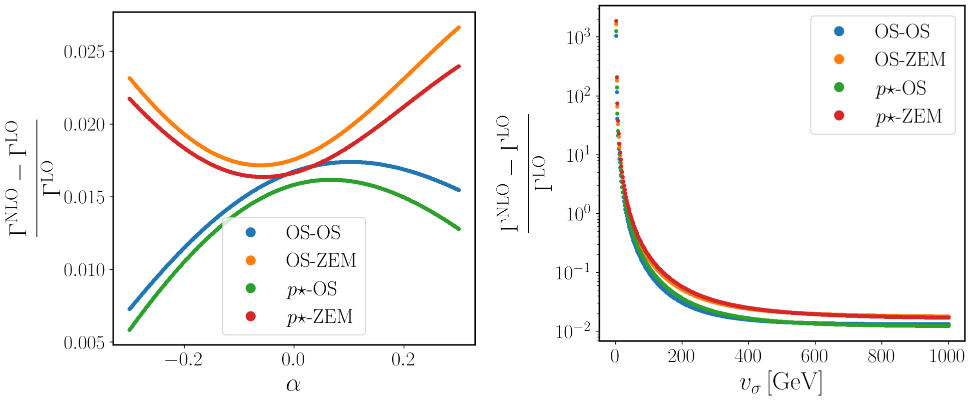

Figure 4.8: Relative difference of the width as a function of the mixing angle α (left) and as a function of v_σ (right). We started with a point, that verified all theoretical and experimental, constraints and varied α in the interval $\left[-\frac{\pi}{2}, \frac{\pi}{2}\right]$ (left) and v_σ in the interval $[10,\ 1000]$ GeV (right).

In the left panel of Fig. 4.8 we plot the relative width difference as a function of the mixing angle α which is sampled in the interval $\left[-\frac{\pi}{2}, \frac{\pi}{2}\right]$. In all range of α variation the relative width difference varies less than 1% for all renormalization schemes. In the right panel of Fig. 4.8 we plot the relative width difference as a function of the scalar VEV v_σ which is varied in the interval $[10,\ 1000]$ GeV. If the scalar VEV v_σ is too small the the width difference diverges for all renormalization schemes. These points are however excluded by the constraints.

We finalise this section with a short discussion of the branching ratio $h_1 \to \sigma_I \sigma_I$ at LO and at NLO. In order to have a rough estimate we divide both the NLO width and the LO width by the total width at

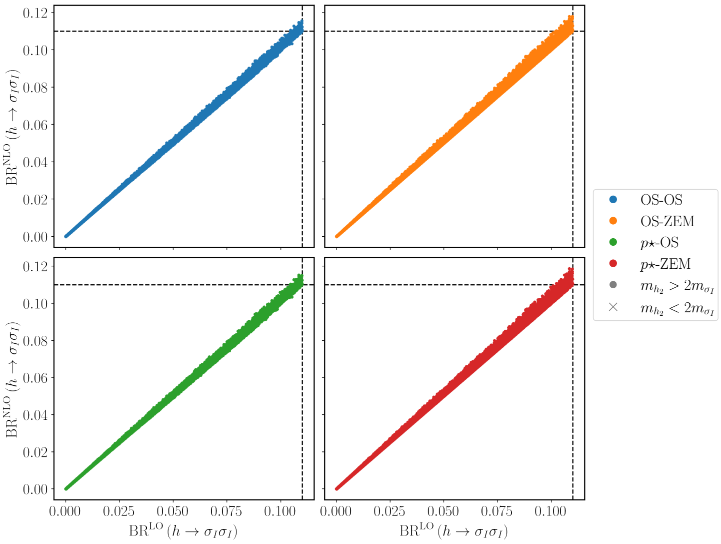

Figure 4.9: Branching ratio for $h_1 \to \sigma_I \sigma_I$ at NLO as a function of the one at LO for the four renormalization schemes.

LO, which is what we have available at the moment. This means that we cannot draw any conclusion but the analysis serves as a rough guide. In Fig. 4.9 we present the branching ratio for $h_1 \to \sigma_I \sigma_I$ at NLO as a function of the one at LO for the four renormalization schemes. It is clear that the corrections are hard to distinguish in the different schemes, especially in a scan. Points with LO branching ratio above 0.11 were discarded. We can see that close to this threshold at LO some NLO points are above this limit. This could hint at improving the parameter space excluded in the future.

4.2 Conclusions on the NLO corrections to Higgs Invisible Width

The main conclusion that one can draw about the NLO corrections to the width in this model is that they are quite stable in all renormalization schemes proposed. The ZEM scheme for the scalar VEV counterterm produces corrections that, although still acceptable, are somewhat larger than the OS scheme for the VEV, particularly for small values of the width. Still these are the values that will hardly be probed in near future. Therefore this small loss is stability is acceptable which allows to probe the entire parameter space, something that can only be done in the ZEM scheme. Although the Higgs mass in the case of the light Higgs scenario is almost unconstrained (only the kinematic constraint on the Higgs decay to DM exists), in the case of the heavy Higgs scenario there are two clear regimes. One regime where the points are above the mass threshold, and in that case the h_2 mass and σ_I mass are tightly correlated. Another regime if the points are below the mass threshold and, in that case, there is no correlation between the two masses. Finally we have compared the branching ratio with its present experimental bound which is 0.11 and saw that could be more points of the parameter space probed if the NLO width is used.

Chapter 5

Primordial Gravitational Waves

5.1 Introduction

Apart from the problem of missing dark matter (DM) analysed in chapter 3 for the particular case of a complex scalar extension of the standard model (CxSM), the SM has another missing key feature: an out of equilibrium epoch. Sakharov [4], in 1967, published a work with the three condition for baryogenesis. The first condition, baryonic number violating processes, is not addressed in this thesis. The second condition, $\mathcal{C}$ and $\mathcal{CP}$ violating processes, has already been established in the SM (although in not enough quantity). $\mathcal{C}$ is violated in weak interactions because gauge bosons couple differently with left-handed or right-handed currents, $\mathcal{CP}$ is also violated via the complex phase in the CKM matrix [41, 42, 3] and can be seen experimentally in Kaon decays into pions [43]. The third condition is the existence of an out of equilibrium transition in the early Universe that does not allow the matter-antimatter symmetry to be restored. A strong candidate for that transition is the electroweak phase transition (EWPT). The Higgs condensation and the consequent breaking of the electroweak (EW) symmetry, $SU(2)_L \times U(1)_Y$ symmetry, into $U(1)_Q$ caused most[1] fundamental particles to acquire mass through the VEV v_h. Unfortunately, it has been known for some time that the SM EWPT is a second-order phase transition for Higgs masses above 66.5 GeV [5] and therefore the third Sakharov condition is not fulfilled. However, it has been shown by Espinosa, Ramon and Quiros that the extension of the SM by a complex scalar is sufficient to produce a first-order phase transition strong enough for EW baryogenesis [44]. Similar results hold for the two Higgs doublet model (2HDM) [45].

In this chapter we will first look for a strong first-order electroweak phase transition and then study the possible production of primordial gravitational waves (GW) that could be detected in the upcoming space interferometer LISA [10]. The implications for the detection of GWs in the case of the complex extension of the SM were first discussed in [46]. To understand where the phase transitions comes from we have to generalize quantum field theory to $T \neq 0$. This is done by modifying the potential so that the parameters become temperature dependent using *finite temperature quantum field theory*[2] (FTQFT) [47]. The phase transition happens between two minima of the potential by quantum tunnelling, described by the formalism of the *bounce action* [48, 47, 49]. The production of gravitational waves is described in detail in [50]. We assume that we have only non-runway bubbles, that is, that the bubble wall velocities are below the speed of light. From a computational point of view, this is no easy task. The relation between the scalar potential parameters and the profile of gravitational waves is populated with numerical instabilities due to the multidimensional nature of the fields as well as the numerical instabilities in the calculation of the bounce action and its derivative. These transitions happen at very specific parameter values. In fact, if we have two very close points in the parameter space, one may produce a FOPT while the other not but intuitively no difference between them was to be expected. We want to study if these instabilities are affected by the experimental uncertainties of the SM and, if so, to what extent. We also want to analyse how codes deal with these uncertainties and if we can improve them somehow. One of the goals of this chapter is to understand the effect of precision of the measurement of the SM parameters affects the spectrum of possible primordial gravitational waves. Another interesting point to analyse is if different patterns of spontaneous symmetry breaking for a specific model can produce different signal strengths for GWs. In this chapter, we are going to analyse how the different types of symmetry breaking in the CxSM model can affect the detectability of GWs and how the addition of new particles can affect the spectrum of GWs. We are going to consider the two phases of CxSM, $v_\sigma = 0$ and $v_\sigma \neq 0$, and also a model with $v_\sigma \neq 0$, Majorana neutrinos and an inverse seesaw mechanism described in [51]. As we will see, the addition of neutrinos will make a big difference in the detectability of the GWs. We are going analyse the GW dependence on the SM parameters in this particular model with added Majorana neutrinos. In the following sections, we are going to define the scenarios that we have for symmetry breaking and also the effective time-dependent potential. The calculations have already been partially implemented in a `python` package named `CosmoTransition`[52] that we are going to use to calculate the bounce action.

---

[1] Not all particles because it is not known how neutrinos masses are generated.

5.2 Scenarios

As stated before we will discuss two different scenarios. The first scenario is the CxSM with both a zero and a non-zero scalar VEV σ, and the second is an extension of the CxSM with Majorana neutrinos with an inverse seesaw mechanism to generate the neutrino masses. The potential is the one described in section 2.2.

- **Scenario 1 -** In this scenario will will examine the two possible patterns of symmetry breaking for the CxSM: one where only the doublet ϕ acquires the usual SM Higgs VEV $v_h = 246.22$ GeV at $T = 0$; the other where both the doublet ϕ and real scalar field σ_R acquire a VEV at $T = 0$ which causes a mixing between the SM-like Higgs boson h and σ_R. In the first case there are two dark matter particles D_1 and D_2 at $T = 0$ and the mass difference is determined by the soft breaking term μ_b^2 in Eq. 2.21. At finite temperature though, the real part of σ may fluctuate around a non zero VEV, i.e. $\phi_\sigma(T)$ is not necessarily zero for all temperatures. In the second case the soft breaking term provides a pseudo-Goldstone mass to the imaginary part of the complex field σ. Again, σ_R can change its VEV as temperature changes but it ends up in a state of $\phi_\sigma(T = 0) \neq 0$.

---

[2] By finite we mean different of 0.

- **Scenario 2 -** This scenario can be seen as an extension of the CxSM with a non-zero singlet VEV, where right-handed neutrinos were added in the context of an inverse seesaw mechanism, see Appendix B. The right-handed components create additional interaction but due to their immensely large mass can be integrated out of the theory[3]. The addition of the right-handed neutrinos will completely change the picture of the equivalent scenario in the CxSM regarding the detection of GWs.

5.3 Finite Temperature Potential

In this section we are going to define effective finite temperature potential. The general expression is given by

$$V_{\text{eff}}(T) = V_0 + V_{\text{CW}}^{(1)} + \Delta V(T) + V_{\text{ct}}\,, \tag{5.1}$$

where V_0 is the tree-level classical scalar potential that was discussed in detail in section 2.2. $V_{\text{CW}}^{(1)}$ is the zero temperature 1-loop Coleman-Weineberg (CW) potential. In the Landau gauge, it is given by

$$V_{\text{CW}} = \sum_i (-1)^{F_i} n_i \frac{m_i^4(\phi_\alpha)}{64\pi^2}\left(\log\left[\frac{m_i^2(\phi_\alpha)}{\Lambda^2}\right] - c_i\right)\,, \tag{5.2}$$

where $F_i = 0(1)$ for bosons(fermions), m_i are the ϕ_α field dependent masses for the particle i and, n_i are the number of degrees of freedom (d.o.f.) of particle i. Finally, Λ is the $\overline{\text{MS}}$ renormalization constants and c_i are $\frac{3}{2}$ for each d.o.f. of scalars, fermions and longitudinally polarised gauge bosons and $\frac{1}{2}$ for each d.o.f. of transversely polarised gauge boson.

The V_{ct} is the counterterm potential that allows for the cancellation of 1-loop divergences. It is obtained by substituting the bare parameters by the counterterms in the tree-level potential and collecting all NLO contributions

$$\begin{aligned} V_{\text{ct}} = {} & \delta\mu_\Phi^2 \Phi^\dagger\Phi + \delta\lambda_\Phi\left(\Phi^\dagger\Phi\right)^2 + \delta\mu_\sigma^2\sigma^\dagger\sigma + \delta\lambda_\sigma\left(\sigma^\dagger\sigma\right)^2 \\ & + \delta\lambda_{\Phi\sigma}\Phi^\dagger\Phi\sigma^\dagger\sigma + \left(\frac{1}{2}\delta\mu_b^2\sigma^2 + \text{ h.c.}\right) \end{aligned} \tag{5.3}$$

Notice that we only perform the renormalization of the potential parameters and leave the fields untouched. The counterterms are fixed by imposing that the Coleman-Weinberg potential and counterterm potential should not change the form of the minimum conditions and masses at zero temperature [53, 45]

---

[3] They are so massive that their propagator is basically zero at EW scale

$$\left\langle \frac{\partial V_{\text{ct}}}{\partial h_i} \right\rangle = \left\langle -\frac{\partial V^{(1)}_{\text{CW}}}{\partial h_i} \right\rangle , \qquad \left\langle \frac{\partial^2 V_{\text{ct}}}{\partial h_i \partial h_j} \right\rangle = \left\langle -\frac{\partial^2 V^{(1)}_{\text{CW}}}{\partial h_i \partial h_j} \right\rangle . \tag{5.4}$$

The counterterms for the CxSM with no VEV in the singlet at zero temperature are given by,

$$\begin{aligned} \delta\mu^2_\Phi &= -\frac{3}{2v_h}\frac{\partial V^{(1)}_{\text{CW}}}{\partial h} + \frac{1}{2}\frac{\partial^2 V^{(1)}_{\text{CW}}}{\partial h^2} , & \delta\lambda_\Phi &= \frac{1}{2v_h^3}\frac{\partial V^{(1)}_{\text{CW}}}{\partial h} - \frac{1}{2v_h^2}\frac{\partial^2 V^{(1)}_{\text{CW}}}{\partial h^2} , \\ \delta\mu^2_\sigma &= 0 , & \delta\lambda_\sigma &= 0 , \\ \delta\lambda_{\Phi\sigma} &= -\frac{2}{v_h^2}\frac{\partial^2 V^{(1)}_{\text{CW}}}{\partial \sigma_R^2} , & \delta\mu^2_b &= 0 . \end{aligned} \tag{5.5}$$

In the case of a non-zero singlet VEV (this also includes scenario 2) we get

$$\begin{aligned} \delta\mu^2_\Phi &= -\frac{3}{2v_h}\frac{\partial V^{(1)}_{\text{CW}}}{\partial h} + \frac{1}{2}\frac{\partial^2 V^{(1)}_{\text{CW}}}{\partial h^2} + \frac{v_\sigma}{2v_h}\frac{\partial^2 V^{(1)}_{\text{CW}}}{\partial h \partial \sigma_R} , & \delta\lambda_\Phi &= \frac{1}{2v_h^3}\frac{\partial V^{(1)}_{\text{CW}}}{\partial h} - \frac{1}{2v_h^2}\frac{\partial^2 V^{(1)}_{\text{CW}}}{\partial h^2} , \\ \delta\mu^2_\sigma &= -\frac{3}{2v_\sigma}\frac{\partial V^{(1)}_{\text{CW}}}{\partial \sigma_R} + \frac{1}{2}\frac{\partial^2 V^{(1)}_{\text{CW}}}{\partial \sigma_R^2} + \frac{v_h}{2v_\sigma}\frac{\partial^2 V^{(1)}_{\text{CW}}}{\partial h \partial \sigma_R} , & \delta\lambda_\sigma &= \frac{1}{2v_\sigma^3}\frac{\partial V^{(1)}_{\text{CW}}}{\partial \sigma_R} - \frac{1}{2v_\sigma^2}\frac{\partial^2 V^{(1)}_{\text{CW}}}{\partial \sigma_R^2} , \\ \delta\lambda_{\Phi\sigma} &= -\frac{1}{v_h v_\sigma}\frac{\partial^2 V^{(1)}_{\text{CW}}}{\partial h \partial \sigma_R} , & \delta\mu^2_b &= 0 . \end{aligned} \tag{5.6}$$

The last ingredient is the one-loop finite-temperature corrections which are denoted as $\Delta V(T)$ and given by [47]

$$\Delta V(T) = \frac{T^4}{2\pi^2}\left\{ \sum_b n_b J_B\left[\frac{m_i^2(\phi_\alpha)}{T^2}\right] - \sum_f n_f J_F\left[\frac{m_i^2(\phi_\alpha)}{T^2}\right] \right\} , \tag{5.7}$$

where n_b (n_f) are the bosonic (fermionic) d.o.f. for each particle b (f) in the summation, and m_i are the field dependent masses. The $J_{B/J}$ functions are the bosonic (fermionic) thermal integrals given by

$$J_{B/F}\left(y^2\right) = \int_0^\infty \mathrm{d}x x^2 \log\left(1 \mp \exp\left[-\sqrt{x^2+y^2}\right]\right) . \tag{5.8}$$

The thermal integrals can be approximated at high temperature ($y \ll 1$) by

$$J_B\left(y^2\right) \approx \frac{-\pi^4}{45} + \frac{\pi^2}{12}y^2 + \mathcal{O}\left(y^3\right) , \tag{5.9}$$

$$J_F\left(y^2\right) \approx \frac{7\pi^4}{360} - \frac{\pi^2}{24}y^2 + \mathcal{O}\left(y^3\right) . \tag{5.10}$$

The presence of T^2 terms in the thermal expansion suggests the possibility for symmetry restoration at high temperatures. This leads to the breakdown of perturbation theory in a close vicinity of the critical temperature, this issue is addressed by means of an all-order resummation procedure via the addition of the so-called daisy, or ring diagrams, [54, 55, 56, 57]. In practice, this is done by a correction to the tree-level potential mass terms given by

$$\mu_\alpha^2(T) = \mu_\alpha^2 + c_\alpha T^2 \,. \tag{5.11}$$

Both for scenarios 1 and 2 there are daisy contributions c_Φ and c_σ of the form

$$c_\Phi = \frac{3}{16}g^2 + \frac{1}{16}g'^2 + \frac{1}{2}\lambda_\Phi + \frac{1}{12}\lambda_{\Phi\sigma} + \frac{1}{4}(y_t^2 + y_b^2 + y_c^2 + y_s^2 + y_u^2 + y_d^2) + \frac{1}{12}(y_\tau^2 + y_\mu^2 + y_e^2)\,, \tag{5.12}$$

$$c_\sigma = \frac{1}{3}\lambda_\sigma + \frac{1}{6}\lambda_{\Phi\sigma}\,, \tag{5.13}$$

with g and g' the EW gauge couplings and y_i the Yukawa coupling of the SM particle i. The longitudinal modes of the gauge bosons also receives thermal corrections

$$m^2_{W_L}(\phi_h;T) = m^2_W(\phi_h) + \frac{11}{6}g^2T^2\,, \tag{5.14}$$

$$m^2_{Z_L,A_L}(\phi_h;T) = \frac{1}{2}m^2_Z(\phi_h) + \frac{11}{12}(g^2+g'^2)T^2 \pm \mathcal{D}\,, \tag{5.15}$$

where

$$\mathcal{D}^2 = \left(\frac{1}{2}m^2_Z(\phi_h) + \frac{11}{12}(g^2+g'^2)T^2\right)^2 - \frac{11}{12}g^2g'^2T^2\left(\phi_h^2 + \frac{11}{3}T^2\right). \tag{5.16}$$

In scenario 2, the daisy correction c_σ receives an additional contribution coming from the neutrino Yukawa sector of the form

$$c_\sigma \to c_\sigma + \frac{1}{24}\sum_{i=1}^{3} Y^2_{\sigma_i}\,, \tag{5.17}$$

where Y_σ are the Yukawa couplings for each leptonic family i (more details on appendix B) the Yukawa coupling Y_h can be neglected because it is orders of magnitude smaller than Y_σ. It is important to notice that the Coleman-Weinberg potential and longitudinal correction to the gauge bosons depend on the field VEVs ϕ_a which are temperature-dependent so that as the potential changes its shape with temperature so will the stationary points change, i.e. the VEVs, and consequently the Coleman-Weinberg potential.

5.4 Gravitational Waves from FOPT

As we mentioned in the last section, the potential shape will change with the decrease of the temperature and as a consequence the VEVs will also change. Additionally, the potential may have two or more simultaneous minima for a given temperature. If we look at Eq. 5.11 we see that at very high temperatures the VEVs are both zero, i.e. $\phi_h(T=0) = \phi_\sigma(T=0) = 0$, which is the beginning of the Universe where the $SU(2)_L \times U_Y(1)$ symmetry is still unbroken. As the temperature drops, another more stable minimum may appear. In that case we call the initial minimum the *false vacuum* and the stable minimum the *true vacuum*. If the conditions are favourable, we can go from one minimum to the other via quantum tunnelling. The transition from the false vacuum to the true vacuum is what we call the *electroweak phase transition*. In order to model the phase transition we use the semi-classical approach [48, 49, 58] of considering the quantum tunnelling from the false vacuum to the true vacuum, also known in the literature as an *instanton* or *pseudo-particle*. Using the semi-classical approach, the tunnelling rate per volume of the transition from the false vacuum to the true vacuum is given by [59]

$$\Gamma(T) = A(T)e^{-\hat{S}_3/T}\,, \tag{5.18}$$

where $\hat{S}_3/T$ is the O(3) symmetric Euclidian action given by

$$\hat{S}_3(\hat{\phi}, T) = 4\pi \int_0^{\infty} \mathrm{d}r\, r^2 \left\{ \frac{1}{2}\left(\frac{\mathrm{d}\hat{\phi}}{\mathrm{d}r}\right)^2 + V_{\text{eff}}(\hat{\phi}, T) \right\}\,, \tag{5.19}$$

with $\hat{\phi}$ being the field VEVs that follow the classical path defined by the Euler-Lagrange equations

$$\frac{d^2\hat{\phi}}{dr^2} + \frac{2}{r}\frac{d\hat{\phi}}{dr} = \frac{dV_{\text{eff}}}{d\hat{\phi}}, \qquad \text{with boundary conditions :} \qquad \hat{\phi}(r)\big|_{r\to\infty} = 0, \qquad \frac{d\hat{\phi}}{dr}\bigg|_{r=0} = 0\,. \tag{5.20}$$

The prefactor $A(T)$ of the tunnelling rate has an intricate expression, but it can be well approximated as

$$A(T) \simeq T^4 \left(\frac{\hat{S}_3}{2\pi T}\right)^{\frac{3}{2}} \tag{5.21}$$

There are three important temperature to characterize the transition. By chronological order, i.e. decreasing temperature, they are

- **Critical Temperature** - T_c - The potential has two degenerate minima and, consequently, the transition from the false vacuum to the true vacuum begins via quantum tunnelling.
- **Nucleation Temperature** - T_n - There is one bubble nucleated per cosmological horizon. T_n is the solutions of

$$\int_{t_c}^{t_n} \Gamma(T)\, V_H(t)\, dt = \int_{T_n}^{T_c} \frac{dT}{T}\frac{\Gamma(T)}{H(T)^4} = \int_{T_n}^{T_c} \frac{dT}{T}\left(\frac{2\zeta M_{\text{Pl}}}{T}\right)^4 e^{-\hat{S}_3/T} = 1\,, \tag{5.22}$$

where $\zeta = 3 \cdot 10^{-3}$ and M_{Pl} is the Planck mass. There is an alternative definition for T_n. It is the temperature at which the tunnelling decay rate matches the Hubble rate [60]

$$\frac{\Gamma(T_n)}{H^4(T_n)} = 1 \tag{5.23}$$

which can be further approximated, in a crude way, as

$$\frac{\hat{S}_3(T_n)}{T_n} \sim 140\,. \tag{5.24}$$

- **Percolation Temperature** - T_* - Temperature at which at least 34% of the false vacuum has tunnelled into the true vacuum [59] or, equivalently, the probability of finding a point still in the false vacuum is 70%. This condition imposes that at the percolation temperature there is a large connected structure of true vacuum that spans the whole Universe, and that is stable and cannot collapse back to the false vacuum. This large structure is known as the *percolating cluster*. The probability of finding a point in the false vacuum is given by [59]:

$$P(T) = e^{-I(T)}, \qquad I(T) = \frac{4\pi v_b^3}{3}\int_T^{T_c} \frac{\Gamma(T')dT'}{T'^4 H(T')}\left(\int_T^{T'} \frac{d\tilde{T}}{H(\tilde{T})}\right)^3 \tag{5.25}$$

  To find the percolation temperature one has to solve $I(T_*) = 0.34$ or, equivalently, $P(T_*) = 0.7$.

The strength of the phase transition, conventionally denoted as α, is related to the latent heat released in the FOPT at the bubble percolation temperature T_*. It is defined by the trace anomaly [61, 62] as

$$\alpha = \frac{1}{\rho_\gamma}\left[V_i - V_f - \frac{T_*}{4}\left(\frac{\partial V_i}{\partial T} - \frac{\partial V_f}{\partial T}\right)\right] \tag{5.26}$$

where $V_i \equiv V_{\text{eff}}(\phi^i_{h,\sigma}; T_*)$ is the value of the effective potential at the false vacuum and $V_f \equiv V_{\text{eff}}(\phi^f_{h,\sigma}; T_*)$ is the value of the effective potential at the true vacuum. And ρ_γ is the energy density of a radiation dominated Universe at the bubble percolation epoch written as a function of the effective number of relativistic degrees of freedom $g_* \simeq 108.75$ for scenario 1 , and $g_* = 114$ for scenario 2[4], [63, 64, 65, 50] is given by

$$\rho_\gamma = g_* \frac{\pi^2}{30} T_*^4 \tag{5.27}$$

For an in-depth study about the strength of the phase transition and the respective GW signal, see Ref. [58].

The second important characteristic of the FOPT is the inverse time-scale of the phase transition denoted as β divided by the Hubble parameter H, such that

$$\frac{\beta}{H} = T_* \frac{d}{dT}\left(\frac{\hat{S}_3(T)}{T}\right)\Bigg|_{T_*}, \tag{5.28}$$

this quantity is relevant for the calculation of the GW profile. The numerical calculation of $\frac{\beta}{H}$ is particularly difficult due to numerical instabilities in the calculation of the derivative, for that reason we have to employ an additional numerical treatment such that we can compute a trustworthy value. This method will be discussed in detail in Appendix C.

In this chapter, we consider only the case of non-runaway nucleated bubbles, i.e. infra-luminal wall expansion velocities $v_b < 1$. By following the formalism of Ref. [50] we can estimate the spectrum of primordial GWs. In the considered scenario the intensity of the GW radiation grows with the ratio $\Delta v_\phi / T_*$, where

---

[4] We admite 6 additional right-handed neutrino that contribute $\frac{7}{8}$ each.

$$\frac{\Delta v_\phi}{T_*} = \frac{|v_\phi^f - v_\phi^i|}{T_*}, \qquad \phi = h, \sigma \tag{5.29}$$

is the difference between the VEVs of the initial v_ϕ^i (metastable) and final v_ϕ^f (stable) phases divided by the bubble percolation temperature T_*. One can also use the quantity $\Delta v_\phi / T_*$ as a way to measure the strength of the GWs.

A phase transition is considered to be of first-order if the order parameter v_c^ϕ / T_c is of order $\mathcal{O}(1)$, where v_c^ϕ are the VEVs calculated at the critical temperature T_c. This sphaleron suppression criterion is one of the most important conditions for successful EW baryogenesis. In this chapter, we consider $\Delta v_*^\phi / T_*$ as the order parameter instead, not only because we have phases with non-zero EW-singlet VEV which contribute to the sphaleron suppression, but also because the actual phase transition starts at $T_n < T_c$, a temperature for which the bubble nucleation rate exceeds that of the cosmological expansion, see Eq. 5.23. Nevertheless, this condition does not necessarily lead to the generation of strong and potentially observable GWs. A sizeable GW signal needs a large bubble wall velocity v_b and a substantial latent heat release which is related to α.

In our analysis we only consider GWs originating only from sound/shock waves (SW) which are generated by the rapid expansion of the bubble in the early Universe. According to Ref. [50] the shock wave is the contribution that dominates the peak frequency and peak amplitude of the GW spectrum. Although there are more sources of gravitational waves such as bubble wall collision [62, 66] and magnetohydrodynamic turbulence of the early Universe plasma [50] their contributions were neglected in this thesis. The primordial GW signals produced in such violent out-of-equilibrium cosmological processes as the FOPTs are redshifted by the cosmological expansion and look today as a cosmic gravitational stochastic background. The corresponding power spectrum [63, 64, 67, 68, 69] of the GW is given by

$$h^2\Omega_{\rm GW}(f) \equiv \frac{h^2}{\rho_c}\frac{\partial \rho_{\rm GW}}{\partial \log f}, \tag{5.30}$$

where ρ_c is the critical energy density today. The power spectrum can be parameterized for various GW frequencies f by multiplying the peak amplitude $h^2\Omega_{\rm GW}^{\rm peak}$ by the spectral function as

$$h^2\Omega_{\rm GW} = h^2\Omega_{\rm GW}^{\rm peak}\left(\frac{4}{7}\right)^{-\frac{7}{2}}\left(\frac{f}{f_{\rm peak}}\right)^3\left[1+\frac{3}{4}\left(\frac{f}{f_{\rm peak}}\right)\right]^{-\frac{7}{2}}, \tag{5.31}$$

where $f_{\rm peak}$ is the peak-frequency. Semi-analytic expressions for peak-amplitude and peak-frequency in terms of β/H and α can be found in Ref. [50] and can be written as

$$f_{\rm peak} = 26 \times 10^{-6} \left(\frac{1}{HR}\right) \left(\frac{T_*}{100}\right) \left(\frac{g_*}{100\ \rm GeV}\right)^{\frac{1}{6}} \rm Hz\,, \tag{5.32}$$

$$h^2\Omega_{\rm GW}^{\rm peak} = 1.159 \times 10^{-7} \left(\frac{100}{g_*}\right) \left(\frac{HR}{\sqrt{c_s}}\right)^2 K^{\frac{3}{2}} \qquad \text{for} \qquad \rm H\tau_{sh} = \frac{2}{\sqrt{3}}\frac{HR}{K^{1/2}} < 1\,, \tag{5.33}$$

$$h^2\Omega_{\rm GW}^{\rm peak} = 1.159 \times 10^{-7} \left(\frac{100}{g_*}\right) \left(\frac{HR}{c_s}\right)^2 K^{2} \qquad \text{for} \qquad \rm H\tau_{sh} = \frac{2}{\sqrt{3}}\frac{HR}{K^{1/2}} \simeq 1\,, \tag{5.34}$$

where $\tau_{\rm sh}$ is the fluid turnover time or the shock formation time, which quantifies the time the GW source was active. In these expressions, $c_s = 1/\sqrt{3}$ is the speed of sound, R is the mean bubble separation,

$$K = \frac{\kappa\alpha}{1+\alpha}\,, \tag{5.35}$$

is the fraction of the kinetic energy in the fluid to the total bubble energy, and

$$HR = \frac{H}{\beta}\,(8\pi)^{\frac{1}{3}} \max\left(v_b, c_s\right)\,, \tag{5.36}$$

where κ is the efficiency factor that can be found in Ref. [70]. The bubble wall velocity has to be rather large to give rise to detectable GWs spectra, although it is quite challenging to provide a precise estimate for it [71, 72]. Our analysis is performed using `CosmoTransitions` [52], considering the case of supersonic detonations to maximize the GW peak amplitude where the wall velocity v_b is taken to be above the Chapman-Jouguet limit,

$$v_{\rm J} = \frac{1}{1+\alpha}\left(c_s + \sqrt{\alpha^2 + \tfrac{2}{3}\alpha}\right)\,. \tag{5.37}$$

For certain parameter configurations, one also expects sequential phase transition patterns potentially leading to multi-peak GWs spectra [73, 74, 75, 76]. Although usually only one of those transitions is strong enough to produce detectable GWs.

5.5 Analysis of Scenario 1

In the first scenario we have two vacuum configuration, the one with zero scalar VEV v_σ and the one with non-zero scalar VEV. They have different renormalization conditions, i.e. Eq. 5.5 and Eq. 5.6. This scenario can indeed produce a first-order EWPT, as well as primordial gravitational waves, but not strong enough to be detectable in the upcoming LISA experiment.

In Fig. 5.1 we present the GW signal $h^2\Omega_{\rm GW}^{\rm peak}$ as a function of the peak frequency $f_{\rm peak}$ in logarithmic scale. The colour in the scatter plots represents the strength of the phase transition α for the zero scalar VEV v_σ (left panel), and for the non-zero scalar VEV (right panel). The grey curves represent the *peak integrated sensitivity curves* (PISCs) for sound waves recently derived in Ref. [77]. To more easily see

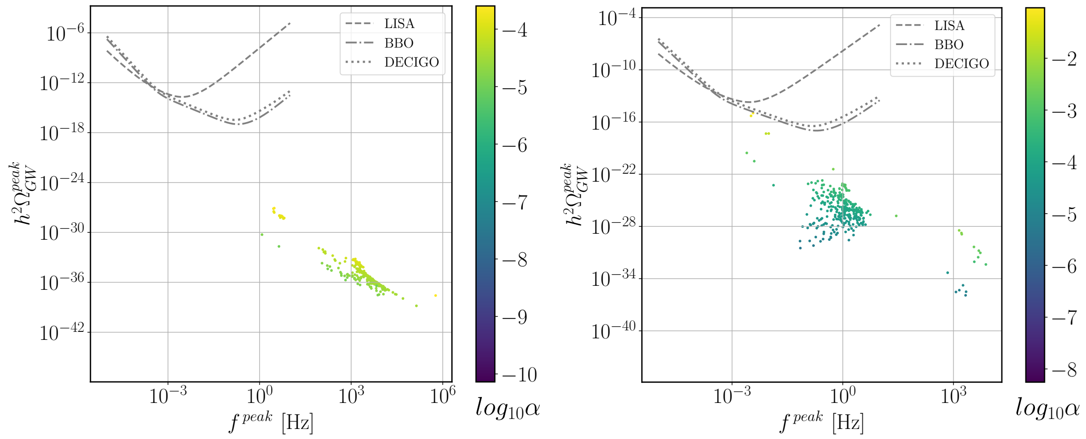

Figure 5.1: The peak-amplitude of the GW signal $h^2\Omega_{\rm GW}^{\rm peak}$ as a function of the peak frequency $f_{\rm peak}$ in logarithmic scale for scenario 1 in both vacuum configurations, the left panel corresponds to the zero scalar VEV v_σ while the right panel is the non-zero scalar VEV v_σ. The colour bar indicates the strength of the phase transition α. The PISCs for LISA BBO and DECIGO are represented with dashed, dot-dashed and dotted lines respectively.

the relation between the detectability of the GWs and α or β/H one should look instead into the signal-to-noise ratio (SNR) which we will do in section 5.7. In our scans, we found 2173 point for the zero scalar VEV v_σ configuration (left), of which only 1336 survived after applying the constraint of having a relative error smaller than 25%, for the non-zero scalar VEV v_σ configuration (right) we found 375 points, of which only 311 points survived the constraint. The important conclusion here is that all points are far from producing detectable GW signals. We see that even though we have more points in the zero VEV configuration, it appears that stronger gravitational waves and naturally produced in the other vacuum configuration. For this reason, considering that we have a rather low number of points and how close we are to entering the zone of detectability, we do not discard the possibility of finding detectable points in the non-zero scalar VEV configuration.

5.6 Analysis of Scenario 2

5.6.1 Gravitational Waves Detection

In scenario 2, the introduction of right-handed neutrinos completely changes the picture of the detectability of gravitational waves. In our scans we found a total of 14390 points, of which only 9613 survived the constraint of having a relative error of 25% or less.

At the time of the phase transition there is a fast change of minima, represented by a fast change of the vacuum configuration. There are different possibilities for how this transition occurs and in order to characterise it we introduce the following notation

$$(v_h^i, v_\sigma^i) \to (v_h^f, v_\sigma^f)\,, \tag{5.38}$$

where the first pair of values represent the VEVs before the phase transition and the second pair are the values after the phase transition. The first term in the pair is the doublet VEV while the second is the real part of the singlet VEV (the imaginary component of the singlet has always zero VEV).

From all 16 possible phase transition patterns, we found that only 7 are strong enough to give rise to detectable GW signals and, of those, the vast majority of points has one of the 3 patterns $(0,0) \to (v_h^f, v_\sigma^f)$, $(0, v_\sigma^i) \to (v_h^f, v_\sigma^f)$ and $(v_h^i, v_\sigma^i) \to (v_h^f, v_\sigma^f)$. Although there are mainly 3 transitions, most of the points in the parameter space that are strong enough to be detectable by the LISA are described by a transition of the type $(0, v_\sigma^i) \to (v_h^f, v_\sigma^f)$. These will be the ones discussed in the following paragraphs. Before moving to the discussion of the results we have to explain in more detail the problems arising with the calculation of the inverse time-scale β/H of the phase transition. The value of β/H is obtained from Eq. (5.28) and it is calculated numerically from the values for the bounce action produced by `CosmoTransitions`. As can be seen from the expression, the calculation involves the derivative of the bounce action, which means that $\hat{S}_3$ has to be a continuous smooth function in the vicinity of the nucleation temperature. This is not always the case – the action obtained from `CosmoTransitions` is, for some points, somewhat erratic so that we had to devise a method to smoothen out these numerical fluctuations before performing the derivative. This procedure is described in great detail in Appendix C together with the estimation of the uncertainty of our method. All results presented, unless otherwise stated, exclude points with an error above 25%.

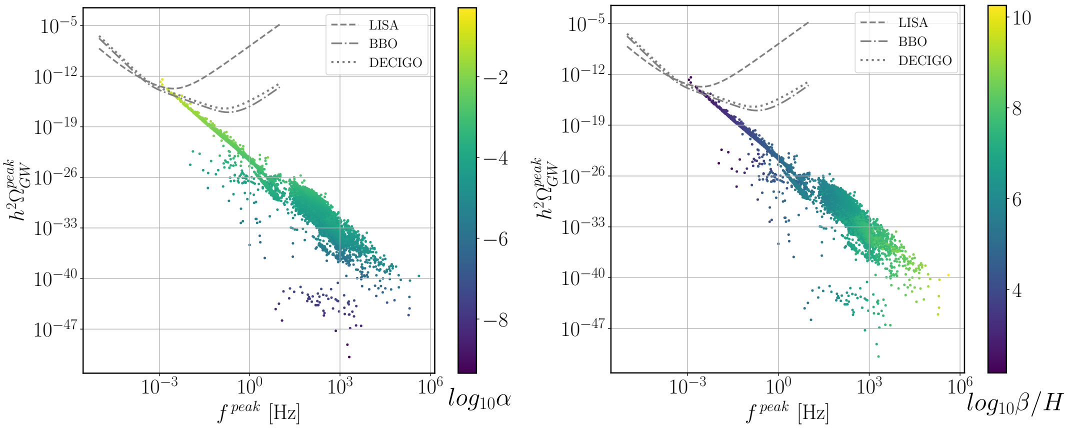

Figure 5.2: The peak-amplitude of the GW signal $h^2\Omega_{\rm GW}^{\rm peak}$ as a function of the peak frequency $f_{\rm peak}$ in logarithmic scale. The colour bar indicates the strength of the phase transition α (left panel) and the inverse time-scale of the phase transition in units of the Hubble parameter H, β/H (right panel). The PISCs for LISA BBO and DECIGO are represented with dashed, dot-dashed and dotted lines respectively.

In Fig. 5.2 we present the GW signal $h^2\Omega_{\rm GW}^{\rm peak}$ as a function of the peak frequency $f_{\rm peak}$ in logarithmic scale. The colour in the scatter plots represents the strength of the phase transition α (left panel), and the inverse time-scale of the phase transition in units of the Hubble parameter H, β/H (right panel). From the figure, it is clear that only values of α above about 0.1 may lead to GW signals detectable in the near future [5]. As for the inverse time-scale, the points within LISA reach are in the range $201 \leq \beta/H \leq 252$.

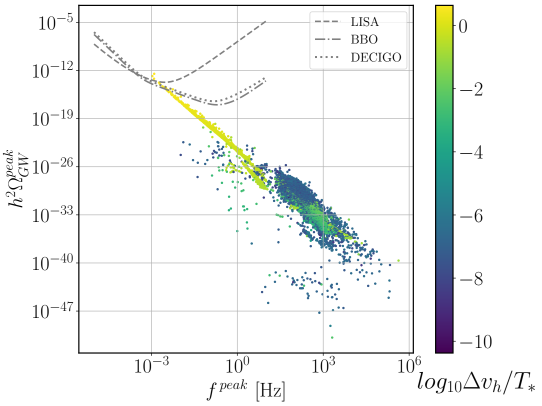

Figure 5.3: Peak-amplitude of the GW signal $h^2\Omega_{\rm GW}^{\rm peak}$ as a function of the peak frequency $f_{\rm peak}$ in logarithmic scale. The scatter plots present, in the colour bar, $\Delta v_h/T_*$ (left panel) and $\Delta v_\sigma/T_*$ (right panel).

A clearer picture of how the different transitions affect the strength of the GW signals can be observed in Fig. 5.4. We can see points clustering around large values of either of the quantities $\Delta v_h/T_*$ and $\Delta v_\sigma/T_*$, but there is only one region that gives rise to observable GW signals, the one where both are simultaneously large.

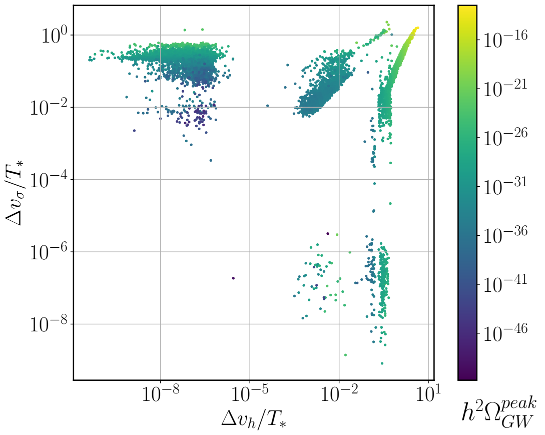

Figure 5.4: Scatter plot showing $\Delta v_h/T_*$ vs. $\Delta v_\sigma/T_*$ with the strength of the GW signal $h^2\Omega_{\rm GW}^{\rm peak}$ given by the colour bar.

---

[5] To be precise, we found points within LISA reach in the range $0.11 \leq \alpha \leq 0.26$.

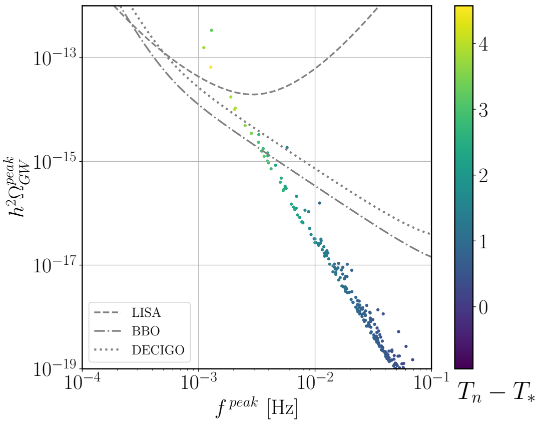

Figure 5.5: The peak-amplitude of the GW signal $h^2\Omega_{\mathrm{GW}}^{\mathrm{peak}}$ as a function of the peak frequency f_{peak} in logarithmic scale. The colour bar indicates the difference between the nucleation temperature and percolation temperature in GeV. The PISCs for LISA BBO and DECIGO are represented with dashed, dot-dashed and dotted lines respectively.

In Fig. 5.5 we present the GW signal $h^2\Omega_{\mathrm{GW}}^{\mathrm{peak}}$ as a function of the peak frequency f_{peak} in logarithmic scale. The colour in the scatter plots represents the difference, in GeV, between the nucleation temperature and the percolation temperature. As the Universe cools down, the characteristic temperatures of the phase transition must occur in the specific order $T_c > T_n > T_*$ The difference between each pair of temperatures also seems to follow a pattern with $T_c - T_n$ much larger than $T_n - T_*$. In our results, we also found that $T_n - T_*$ is usually a few GeV apart for strong points but that difference vanishes as we go below the PISC curves. The difference $T_c - T_n$ seems to be of the order of $\mathcal{O}(20)$ GeV for strong points, but for points below the PISC curves it can take any value.

5.6.2 The dependence on the SM parameters

In the studies presented in the literature connecting FOPT with the detection of primordial GWs, the role of the SM parameters is not usually discussed (to the best of our knowledge). Suppose that a GW is detected and that it points to a given class of models. One should then ask: what happens if we vary each of the SM parameters within the experimentally determined error? Will it lead to significant changes in the characteristics of the GW or not? These are the questions that we will discuss in this section taking, as a benchmark, only scenario 2 into consideration. Note that this scenario is not only one of the simplest extensions of the SM but it also features the perk of generating neutrinos masses. Moreover, as we have seen in the previous section, this is a model that leads to GW signals potentially detectable in the not-so-distant future. In order to understand the impact of the variation of the SM parameters within their experimental errors, we have first chosen points that are within LISA reach of detection and with all SM parameters in their central experimental values, according to the PDG review [3]. We then varied each of the fermion masses, from the electron to the top quark, the W and Z bosons' masses and the Higgs mass, all within their experimental error at 1σ. The variation of the masses of the SM particles and the calculation of the uncertainty in the peak of the GW power spectrum are described in detail in Appendix C. We concluded that using the smoothed version of the bounce action[6], the only SM masses capable of inducing a noticeable variation of the GW peak amplitude and frequency are the top quark mass and, even more so, the Higgs boson mass.

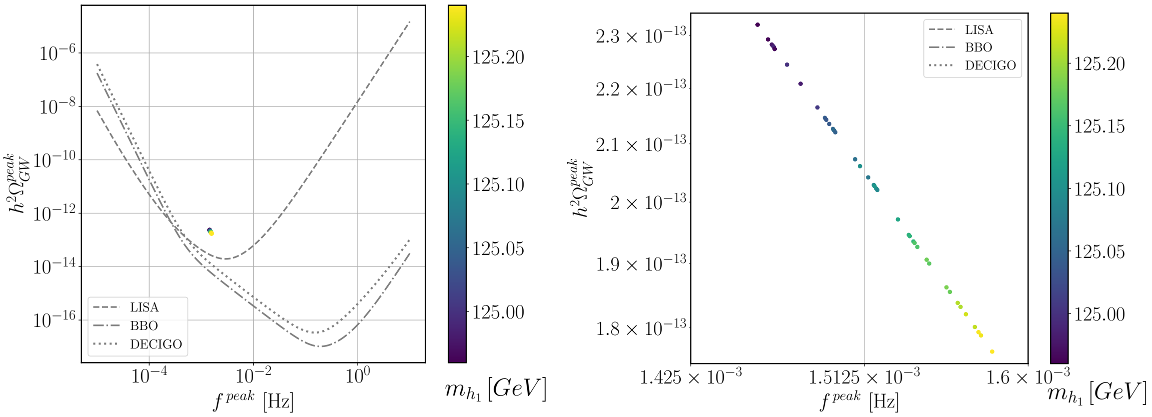

Figure 5.6: The dependence of $h^2\Omega_{\text{GW}}^{\text{peak}}$ on the peak-frequency f_{peak} and the Higgs boson mass m_{h_1} for fixed dark sector parameters, $m_{h_2} = 994.0$ GeV, $m_{\sigma_I} = 599.9$ GeV, $v_\sigma = 275.6$ GeV, $\alpha = -0.52$, $M_\nu = 254.1$ GeV and $\tilde{\mu} = 3.0$ is shown on the left panel, since the variation is very small we show a zoomed in version in the right panel. The chosen original FOPT (before parameters' variation) is characterised by $T_c = 80.7$ GeV, $T_n = 57.5$ GeV, $T_* = 54.2$ GeV, $\left(v_h^i, v_\sigma^i\right) \to \left(v_h^f, v_\sigma^f\right) = (0.0, 185.3) \to (236.2, 269.4)$, $\alpha = 0.26$, $\beta/H = 253$, $\Delta v_h/T_* = 4.4$ and $\Delta v_\sigma/T_* = 1.6$. The Higgs mass is varied within the experimental uncertainty, i.e. between 124.96 GeV and 125.24 GeV. The remaining SM parameters are fixed to their central values. Only the points for which a FOPT took place are shown.

In Fig. 5.6 we present a specific point that could be potentially probed by LISA, in the context of scenario 2. The corresponding FOPT has been found for the central values of the SM parameters and for the following dark sector parameters: $m_{h_2} = 994.0$ GeV, $m_{\sigma_I} = 599.9$ GeV, $v_\sigma = 275.6$ GeV, $\alpha = -0.52$, $M_\nu = 254.1$ GeV and $\tilde{\mu} = 3.0$. The variation of the Higgs mass is performed from 124.96 GeV to 125.24 GeV, corresponding to an uncertainty in the Higgs mass of ±1 standard deviation while keeping the remaining parameters constant. The remaining relevant parameters are shown in the figure caption. In the left plot, we show the GW peak amplitude as a function of the peak frequency. We can see that there is a variation of 25% of the position of the peak. In the right plot, we show a zoomed version of the plot on the left. The conclusion is clear, the variation of only the Higgs mass within its experimental uncertainty leads to a meaningful variation of the peak amplitude (and also peak frequency) . We found similar results for other points with strong GW signals and therefore the dependence on the Higgs mass is indeed meaningful and must be considered in this type of numerical studies.

---

[6] If we do not use the smoothed action we get enormously large variations with any variation of any mass, however small.

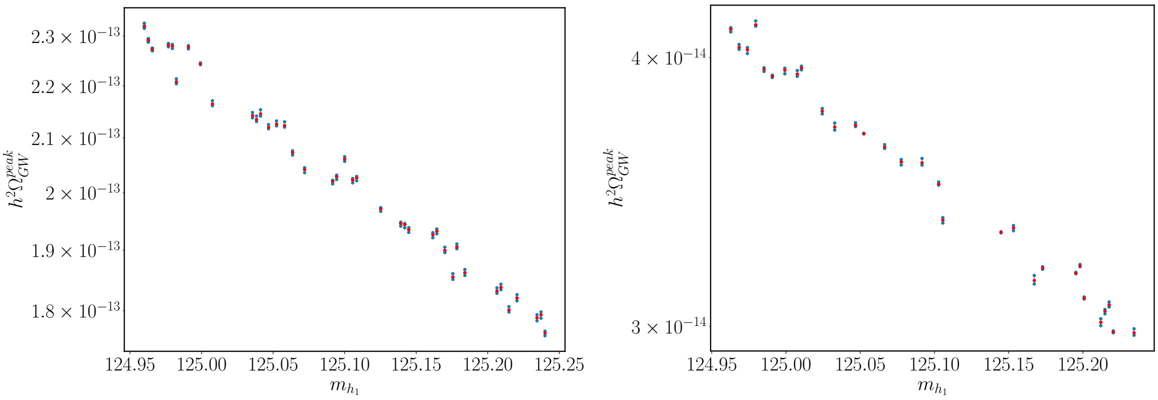

Figure 5.7: The dependence of $h^2\Omega_{\mathrm{GW}}^{\mathrm{peak}}$ on the peak-frequency f_{peak} and the Higgs mass m_{h_1}. The Higgs mass is varied by 1σ around the central value keeping all other parameters fixed. In the left plot, the original (before variation of any parameters) phase transition was found for the central values of the SM parameters and for the fixed parameters of the dark sector: $m_{h_2} = 994.0$ GeV, $m_{\sigma_I} = 599.9$ GeV, $v_\sigma = 275.6$ GeV, $\alpha = -0.52$, $M_\nu = 254.1$ GeV and $\tilde{\mu} = 3.0$. The original FOPT is characterised by $T_c = 80.7$ GeV, $T_n = 57.5$ GeV, $T_* = 54.2$ GeV, $\left(v_h^i, v_\sigma^i\right) \to \left(v_h^f, v_\sigma^f\right) = (0.0, 185.3) \to (236.2, 269.4)$, $\alpha = 0.26$, $\beta/H = 253$, $\Delta v_h/T_* = 4.4$ and $\Delta v_\sigma/T_* = 1.6$. In the right plot, the same quantities is shown but for $m_{h_2} = 955.3$ GeV, $m_{\sigma_I} = 858, 6$ GeV, $v_\sigma = 267.1$ GeV, $\alpha = 0.11$, $M_\nu = 198.3$ GeV and $\tilde{\mu} = 0.03$ yielding the original FOPT characterised by $T_c = 103.0$ GeV, $T_n = 71.6$ GeV, $T_* = 67.1$ GeV, $\left(v_h^i, v_\sigma^i\right) \to \left(v_h^f, v_\sigma^f\right) = (0.0, 170.7) \to (239.8, 263.3)$, $\alpha = 0.11$, $\beta/H = 202$, $\Delta v_h/T_* = 3.6$ and $\Delta v_\sigma/T_* = 1.4$.

The SM parameter that has the most impact in the GW peak amplitude, and frequency, is the Higgs mass. In Fig. 5.7 we show the peak-value of the GW power spectrum $h^2\Omega_{\mathrm{GW}}^{\mathrm{peak}}$ as a function of the Higgs mass m_{h_1} for two points within LISA reach. Only the points for which a FOPT took place are shown, the red dots indicate the numerically calculated value for $h^2\Omega_{\mathrm{GW}}^{\mathrm{peak}}$ and the blue dots are the corresponding error, see Appendix C for more details. The numerical values for the dark sector parameters are shown in the caption. For both plots, we vary the Higgs mass between 124.96 GeV and 125.24 GeV, which corresponds to an uncertainty of ± 1 standard deviation. There is a variation of the peak by approximately a factor of 25%, a small variation but still meaningful to the GW profile.

The other SM parameter that can shift the GW peak amplitude, and frequency, is the top quark mass. In Fig. 5.8 we show the peak-value of the GW power spectrum $h^2\Omega_{\mathrm{GW}}^{\mathrm{peak}}$ as a function of the top quark mass m_t for two points within LISA reach. Again, only the points for which a FOPT took place are shown, the red dots indicate the numerically calculated value for $h^2\Omega_{\mathrm{GW}}^{\mathrm{peak}}$ and the blue dots are the corresponding error, see Appendix C for more details. The numerical values for the dark sector parameters are shown

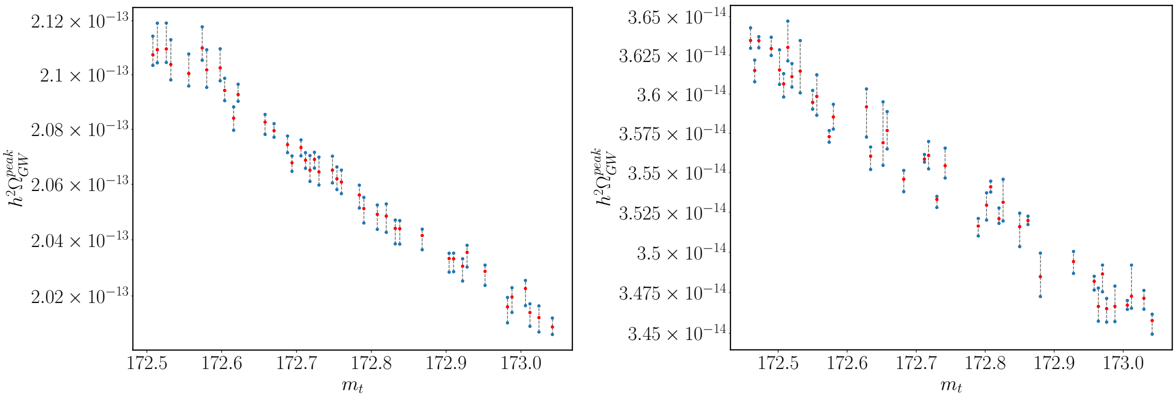

Figure 5.8: The dependence of $h^2\Omega_{\text{GW}}^{\text{peak}}$ on the peak-frequency f_{peak} and the top quark mass m_t. The top quark mass is varied by 1σ around the central value keeping all other parameters fixed. In the left plot, the original (before parameters' variation) phase transition was found for the central values of the SM parameters and for the fixed parameters of the dark sector: $m_{h_2} = 994.0$ GeV, $m_{\sigma_I} = 599.9$ GeV, $v_\sigma = 275.6$ GeV, $\alpha = -0.52$, $M_\nu = 254.1$ GeV and $\tilde{\mu} = 3.0$. The original FOPT is characterised by $T_c = 80.7$ GeV, $T_n = 57.5$ GeV, $T_* = 54.2$ GeV, $\left(v_h^i, v_\sigma^i\right) \to \left(v_h^f, v_\sigma^f\right) = (0.0, 185.3) \to (236.2, 269.4)$, $\alpha = 0.26$, $\beta/H = 253$, $\Delta v_h/T_* = 4.4$ and $\Delta v_\sigma/T_* = 1.6$. In the right plot, the same quantities is shown but for $m_{h_2} = 955.3$ GeV, $m_{\sigma_I} = 858, 6$ GeV, $v_\sigma = 267.1$ GeV, $\alpha = 0.11$, $M_\nu = 198.3$ GeV and $\tilde{\mu} = 0.03$ yielding the original FOPT characterised by $T_c = 103.0$ GeV, $T_n = 71.6$ GeV, $T_* = 67.1$ GeV, $\left(v_h^i, v_\sigma^i\right) \to \left(v_h^f, v_\sigma^f\right) = (0.0, 170.7) \to (239.8, 263.3)$, $\alpha = 0.11$, $\beta/H = 202$, $\Delta v_h/T_* = 3.6$ and $\Delta v_\sigma/T_* = 1.4$.

in the caption. For both plots, we now vary the top quark mass between 172.46 GeV and 173.06 GeV, which corresponds to an uncertainty in the top quark mass of ± 1 standard deviation. There is a variation of the peak by, approximately, a factor of 5%, which is smaller than the variation for the Higgs mass, but still noticeable in the context of the considered variation in the top quark mass inside its experimental uncertainty.

In conclusion, if a GW signal is detected, one must be careful in rushing to conclusions about either the model or its parameters since the experimental uncertainty in the SM parameters can still play a role. With this in mind, a more precise determination of the Higgs and top quark masses is motivated in light of a hypothetical discovery of a primordial GW signal and its theoretical interpretations, which is one further justification for future lepton colliders. We varied the mass of all other particles but found no noticeable impact in the GW profile. We also found that only strong GWs waves, i.e. above PISC curves, are influenced by the Higgs and top quark mass, this dependence seems to vanish as we go to weaker GWs signals.

5.7 Signal-to-Noise Ratio

So far our discussion has been only around Scenario 2. The main reason behind this choice is the fact that the right-handed Majorana neutrinos allows for points with a strong FOPT detectable by LISA experiment. This model also has the advantage of providing an explanation for the neutrino mass which, in turn, leaves room for explanation of the neutrino oscillation that is observed in experiments. We will now discuss the two scenarios from the point of view of the detectability by LISA. In particular, we are going to analyze the signal-to-noise ratio defined as

$$\mathrm{SNR} = \sqrt{\mathcal{T} \int_{f_{\min}}^{f_{\max}} \mathrm{d}f \left[\frac{h^2 \Omega_{\mathrm{GW}}(f)}{h^2 \Omega_{\mathrm{Sens}}(f)} \right]^2}\,, \tag{5.39}$$

where $\mathcal{T}$ is the duration of the acquisition of experimental data (three years on our plots), and $h^2\Omega_{\mathrm{Sens}}(f)$ is the nominal sensitivity for a given LISA configuration, see Ref.[50] for more details.

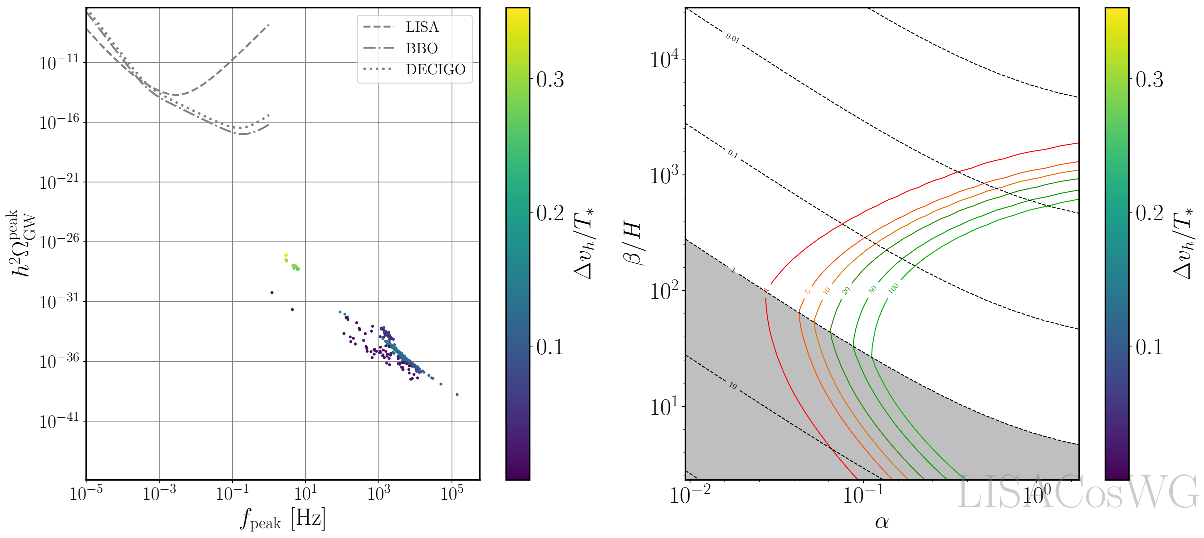

Figure 5.9: Scatter plots showing the strength of the phase transitions $\Delta v_h/T_*$ in the colour scale for scenario 1 with zero scalar VEV v_σ. On the left panel we show the position of the GW peak as a function of the peak frequency while, on the right, we show the corresponding SNR for a mission profile of three years. The colored lines show the SNR that depends on T_*, $g_*(T_*)$ and v_{b}. The dotted curves are contour lines representing the shock formation time τ_{sh} as defined in (5.34). The grey shaded region corresponds to an acoustic period lasting longer than a Hubble time and it is where the sound waves treatment is most reliable.

In Fig. 5.9 we present, for scenario 1 with zero scalar VEV v_σ, the scatter plots showing the GW peak position as a function of the strength of the phase transitions $\Delta v_h/T_*$ in the colour scale (left), and the corresponding signal-to-noise (SNR) ratio for the phase transition (right) for a mission profile of 3 years. The colour grade scale is the same on both plots. The right panel was generated using `PTPlot 1.0.1` [50]. The colored isolines display the expected values for the SNR that depend on T_*, g_* and v_b while the dashed black contour lines represent the shock formation time τ_{sh} (see Eq. 5.34). The grey shaded region corresponds to a Universe with an acoustic period lasting longer than a Hubble time and where the approximation that GWs are produced by sound waves is most reliable [58, 62]. For $\tau_{\text{sh}} \ll 1$, the turbulence effects may become important dumping the acoustic contribution. However, none of our points feature a too small shock formation time. Using the formula for turbulence effects in Refs. [78, 58] for an estimate, we realize that it does indeed have very little impact on the peak position on the left panel. That the actual role of turbulence is not yet very clear [79, 80, 81], and further studies are necessary for a more reliable calculation of such contribution. The SNR contours on the right panel take into account the effect of an increasingly short-lasting shock formation at the cost of a decreasing SNR value. As previously mentioned in section 5.5 we found no points that can be detectable in LISA experiment, this is why the plot of the right has no points. Several dedicated scans were performed but the trend did not change, there are so many terms and variables that could be responsible for this outcome so we could not pinpoint a clear reason for the inexistence of points.

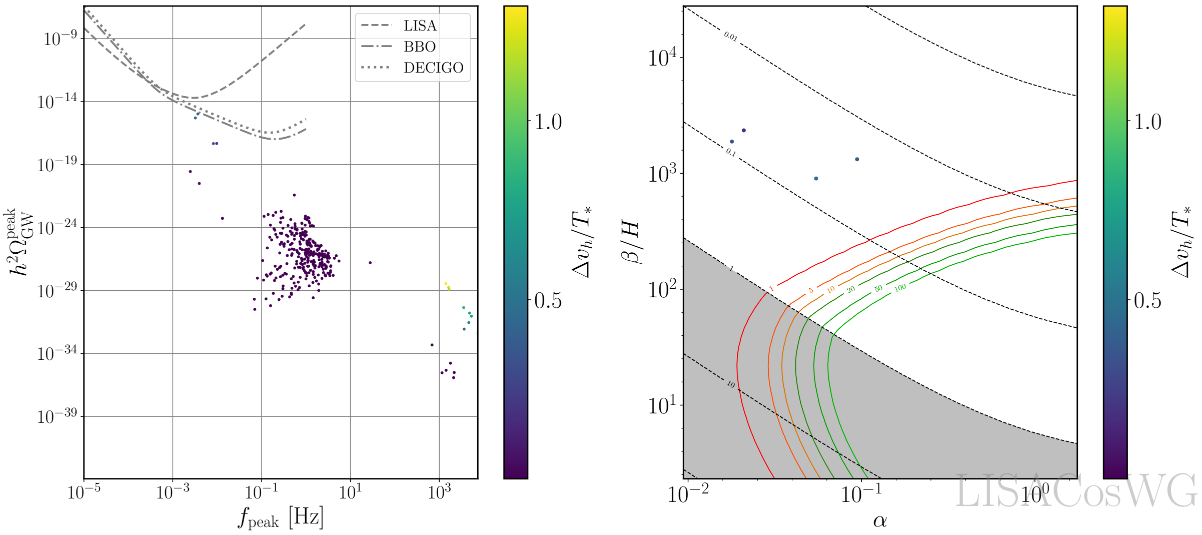

Figure 5.10: Scatter plots showing the typical strength of the phase transitions $\Delta v_h/T_*$ and SNR for scenario 1 with non-zero scalar VEV v_σ.

In Fig. 5.10 we present the same plots as in Fig. 5.9 for scenario 1 but with non-zero scalar VEV v_σ. Just as in the previous case, all points with a FOPT give rise to GW signals not strong enough to reach LISA sensitivity domain, but in this vacuum configuration the points are much stronger than the previous case. Due to the small number of points, and consequently a low statistical significance, we do not discard the possibility of finding points in LISA sensitivity the future.

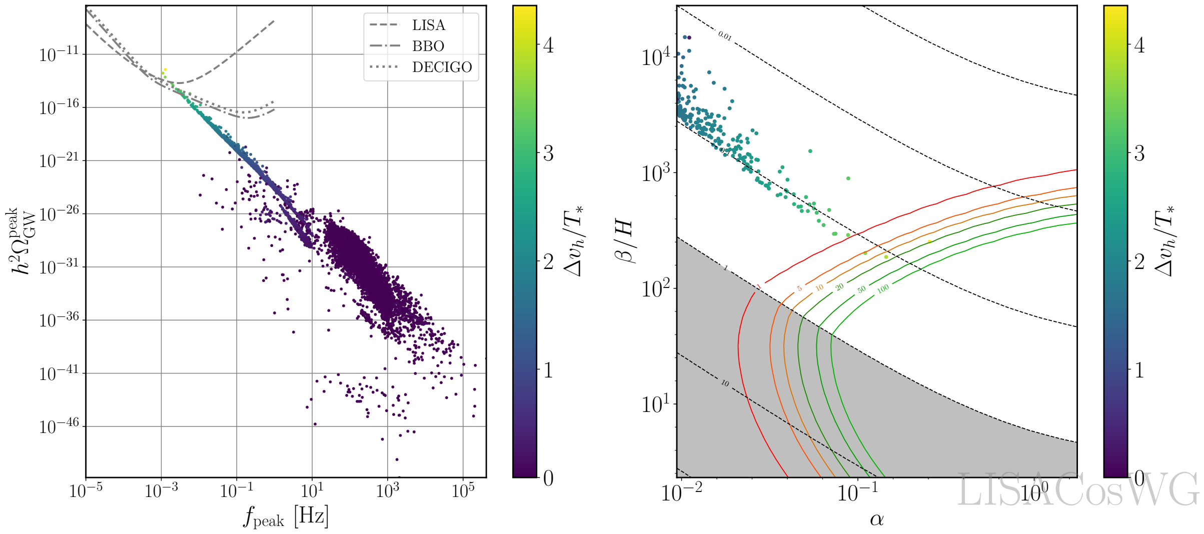

Figure 5.11: Scatter plots showing the typical strength of the phase transitions $\Delta v_h/T_*$ and SNR for scenario 2.

Finally in Fig. 5.11 we show similar plots but for scenario 2. Surprisingly, the addition of right-handed Majorana neutrinos to the CxSM allows us to find detectable points, if not at LISA possibly at DECIGO or BBO. In fact, we have two points above LISA PISCs which correspond to a point with SNR of 5 and another with SNR of 20. The only difference in scenario 2 when compared to scenario 1 is a larger field multiplicity and a modified thermal mass due to the neutrino-Majoron Yukawa coupling $Y_{\sigma,i}$ as shown in Eq. 5.17. Further studies of Majoron models in the context of primordial GWs were performed in Ref. [51] and, more recently, in Ref. [82].

5.8 Conclusions on Gravitational Waves

We have discussed the observation of primordial GWs produced by shock waves originating from a strong EW FOPT using, as a benchmark model, an extension of the SM by a complex singlet field. Two different scenarios were analysed: scenario 1 with two vacuum configurations, one with zero scalar VEV v_σ and another with non-zero scalar v_σ, the first configuration leads to the SM plus two DM candidates that only interact via the portal coupling, and the latter to the SM with two Higgs and a dark matter particle. Finally, scenario 2 where, besides the configuration of scenario 1 with non-zero VEV v_σ, three generations of right-handed neutrinos were added to the model. In this chapter, scenario 2 was then used to answer some key questions that relate the Higgs potential with the detection of GWs. Our conclusion is that the variation of the SM particle masses does indeed lead to sizeable differences both in the peak of the GW power spectrum and in its peak frequency. This is particularly true for the Higgs and top quark mass, the heaviest quark. The other SM masses have little to no impact on the GWs profile. We should underline the point that the variation of the Higgs mass within the measured experimental error can lead to a variation of around 30%, or less, of the GW peak density while the top quark masses produces a variation of around 5%, or less. It is then crucial to increase the precision in the Higgs and top mass measurement if this effect is to be mitigated, which can be seen as a motivation for future lepton collider machines. Note that this is the conclusion for a particular very simple model and that there could be models with even more dramatic changes. After concluding that the SM parameters have an impact on the detection of GWs, it does not come as a surprise that the other parameters from the potential, including the DM masses and the portal coupling also play a major role. The second question we wanted to answer was whether the spontaneous symmetry breaking of a given model would lead to differences in the strength of the GW spectrum. We concluded that indeed it does, the non-zero VEV configuration produces stronger waves than the zero scalar VEV, although not strong enough to lead to detectable gravitational waves. Nevertheless, the addition of right-handed Majorana neutrinos to scenario 2, leads to a possibility of GWs detection. Hence, we believe that our study delivers two clear messages. First, any such study needs to take into account the precision in the measurements of at least the Higgs mass and the top quark mass. Second, even the same model, if considered in different phases at zero temperature, can exhibit a very distinct behaviour in what concerns the detection of GWs originating from strong EW FOPTs. Finally, we have discussed computational issues on the calculation of β/H, and how not taking proper care of the derivative of the bounce action can lead to numerical instabilities and, consequently, to unphysical results.

Appendix A

Pinch technique

The aim of the pinch technique [38] is to separate in a consistent way the gauge dependence of the self energy. In this Appendix, we will derive in detail how to reach this goal in the CxSM. Before applying the pinch technique we will start by considering the self-energy $\Sigma_{h_ih_j}$ and split it into a gauge dependent part and a Feynman-t'Hooft part ($\xi_i = 1$). We define

$$\Sigma^{\text{tad}}_{h_ih_j} = \Sigma^{\text{tad}}_{h_ih_j}|_{\xi=1} + \Sigma^{\text{tad}}_{h_ih_j}|_{\text{g.d.}} \,, \tag{A.1}$$

where the subscript $\xi = 1$ indicates the gauge independent Feynman-t'Hooft contribution to the self-energy and the subscript g.d. indicates that the term is gauge dependent. Without any loss of generality we decide to split the gauge dependent part around $\xi = 1$ is - any other choice is possible. First, we isolate the gauge dependent part of the self-energy as

$$\Sigma^{\text{tad}}_{h_ih_j}|_{\text{g.d.}} = \Sigma^{\text{tad}}_{h_ih_j} - \Sigma^{\text{tad}}_{h_ih_j}|_{\xi=1} \,. \tag{A.2}$$

Explicitly, the gauge dependence of the $h_i \to h_j$ self-energy (diagrams in Fig. A.1) is given by

$$\begin{aligned}\Sigma^{\text{tad}}_{h_ih_j}(p^2)|_{\text{g.d.}} =&\lambda_Z \frac{g^2\mathcal{O}_{h_ih_j}}{64\pi^2 c_w}\left[\frac{\beta_{Z\xi Z}+\beta_{ZZ}}{2}\left(p^4 - m^2_{h_i}m^2_{h_j}\right) - \alpha_Z\left(p^2 - \frac{m^2_{h_i}+m^2_{h_j}}{2}\right)\right]\\ &+\lambda_W \frac{g^2\mathcal{O}_{h_ih_j}}{32\pi^2}\left[\frac{\beta_{W\xi W}+\beta_{WW}}{2}\left(p^4 - m^2_{h_i}m^2_{h_j}\right) - \alpha_W\left(p^2 - \frac{m^2_{h_i}+m^2_{h_j}}{2}\right)\right]\end{aligned} \tag{A.3}$$

where α and β are gauge dependent Passarino-Veltmann integrals defined in Eqs. A.8 and A.9.

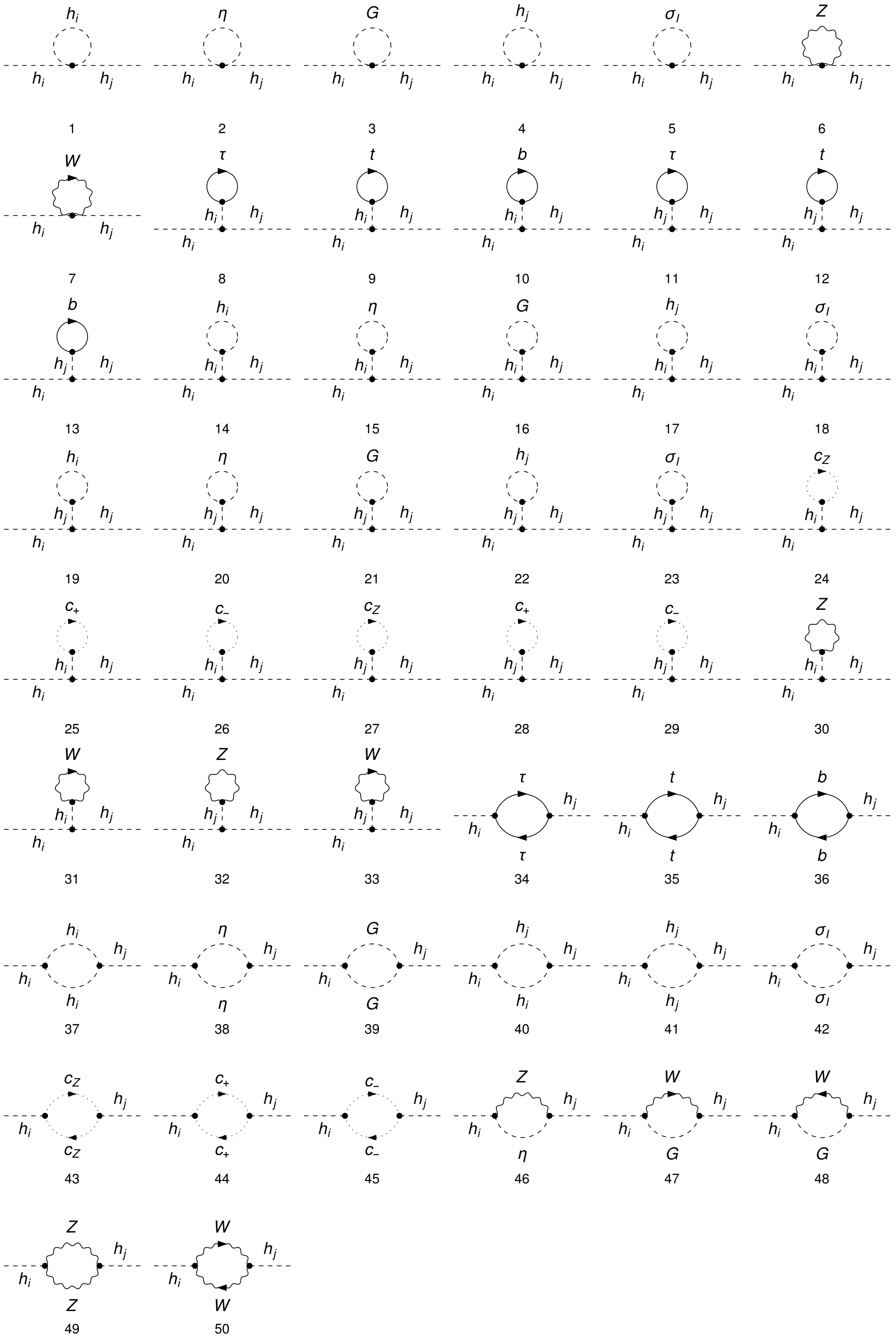
h_i h_i h_j 1
η h_i h_j 2
G h_i h_j 3
h_j h_i h_j 4
σ_l h_i h_j 5
Z h_i h_j 6
W h_i h_j 7
τ h_i h_j h_i 8
t h_i h_j h_i 9
b h_i h_j h_i 10
τ h_j h_j h_i 11
t h_j h_j h_i 12
b h_j h_j h_i 13
h_i h_i h_j h_i 14
η h_i h_j h_i 15
G h_i h_j h_i 16
h_j h_i h_j h_i 17
σ_l h_i h_j h_i 18
h_i h_j h_j h_i 19
η h_j h_j h_i 20
G h_j h_j h_i 21
h_j h_j h_j h_i 22
σ_l h_j h_j h_i 23
c_Z h_i h_j h_i 24
c_+ h_i h_j h_i 25
c_- h_i h_j h_i 26
c_Z h_j h_j h_i 27
c_+ h_j h_j h_i 28
c_- h_j h_j h_i 29
Z h_i h_j h_i 30
W h_i h_j h_i 31
Z h_j h_j h_i 32
W h_j h_j h_i 33
τ h_j h_i τ 34
t h_j h_i t 35
b h_j h_i b 36
h_i h_j h_i h_i 37
η h_j h_i η 38
G h_j h_i G 39
h_j h_j h_i h_i 40
h_j h_j h_i h_j 41
σ_l h_j h_i σ_l 42
c_Z h_j h_i c_Z 43
c_+ h_j h_i c_+ 44
c_- h_j h_i c_- 45
Z h_j h_i η 46
W h_j h_i G 47
W h_j h_i G 48
Z h_j h_i Z 49
W h_j h_i W 50

Figure A.1: Set of diagrams that contribute to the general $h_i \to h_j$ self-energy, in the Fleischer and Jegerlehner tadpole scheme.

Now we are going to discuss the main idea behind the pinch technique. It has been shown that any element of the scattering matrix S is gauge independent at any order of perturbation theory [17]. If we computed the scattering amplitude of $\mu\bar{\mu} \to b\bar{b}$[1] we would find it to be gauge independent. On the other hand, we can split the contribution into diagrams with self-energies and other diagrams as

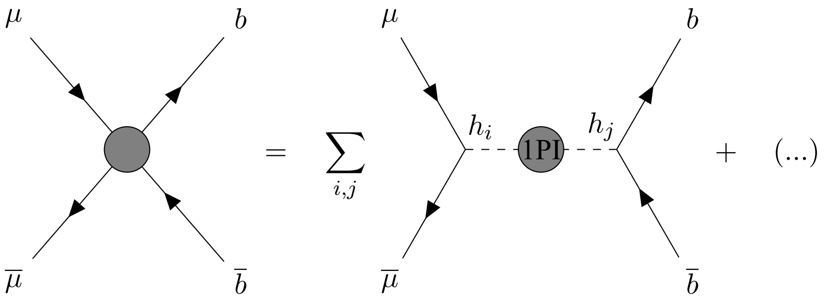

(A.4)

where the 1PI also include tadpole contributions. The self-energies that we are interested in appear explicitly in the scattering amplitude. They can be extracted by removing the external fermionic legs and cutting the h_i and h_j propagators. The self-energies are gauge dependent and therefore the diagrams explicitly drawn in Eq. A.4 are gauge dependent as well. Since the left-hand side of Eq. A.4 is gauge independent then the diagrams not drawn must cancel the gauge dependency of the self-energies. The goal of the pinch technique is to extract this correction that ensures that the final result is gauge independent. At start it is not clear where these corrections come from. There are complex dependencies on the propagators and it is not very easy to see how these dependencies can cancel.

We start by noticing that the gauge bosons Z and W couplings with fermions are proportional to the gamma matrices γ_μ. On the other hand, their propagators have a component proportional to its momentum k^μ. This already allows for a simplification. Suppose we have a fermionic current with an internal propagator, with momentum $p + k$ and a coupling with a gauge boson with momentum k. Then there would be a term proportional to

$$\frac{i}{\not{p}+\not{k}-m_f}\not{k} = \frac{i\left(\not{p}+\not{k}-m_f-(\not{p}-m_f)\right)}{\not{p}+\not{k}-m_f} = i - i\frac{(\not{p}-m_f)}{\not{p}+\not{k}-m_f}\,. \tag{A.5}$$

We successfully managed to get rid of one propagator, at least partially. The first term of Eq. A.5 is called the *pinched contribution*, the second term cannot be simplified further and, for that reason, it will not have any role on cancelling the gauge dependencies of the self-energies and can be dropped. The pinch contributions, which have no internal fermionic propagators, can be rewritten with the structure of a self-energy, just as in Eq. A.4, and contribute to the cancellation of the gauge dependency. This is the heart of the pinch technique. We will now go through all diagrams contributing to the scattering and extract the pieces that have the structure of a self-energy. In the end, we sum all pinch contributions and use them to correct the self-energy, making it gauge independent.

---

[1] We can apply the same reasoning to any other fermionic scattering.

Let us define some extremely useful relations for the pinch technique

$$\lambda_i = 1 - \xi_i, i = \{W, Z\} \quad \text{(W and Z boson)}, \qquad\qquad \sum_{m,n} \mathcal{O}^2_{h_m h_n} = 1\,, \tag{A.6}$$

where $\mathcal{O}_{h_m h_n}$ are couplings defined in Eq. 3.109.

$$\frac{\sum_m \mathcal{O}_{h_m,h_m}}{q^2 - m^2_{h_m}} = \sum_{m,n} \mathcal{O}^2_{h_m,h_n} \frac{q^2 - \dfrac{m_{h_m} + m_{h_n}}{2}}{(q^2 - m_{h_m})(q^2 - m_{h_n})}\,, \tag{A.7}$$

$$\frac{i}{16\pi^2}\alpha_{\mathrm{i}} \equiv \int \frac{d^4k}{\left[k^2 - m_{\mathrm{i}}^2\right]\left[k^2 - \xi_{\mathrm{i}} m_{\mathrm{i}}^2\right]}, \,, \tag{A.8}$$

$$\frac{i}{16\pi^2}\beta_{\mathrm{ij}}\left(p^2\right) \equiv \int \frac{d^4k}{\left[k^2 - m_{\mathrm{i}}^2\right]\left[k^2 - \xi_{\mathrm{i}} m_{\mathrm{i}}^2\right]\left[(k+p)^2 - m_{\mathrm{j}}^2\right]}\,. \tag{A.9}$$

The functions α_i and β_{ij} can be converted back into the Passarino-Veltmann integrals

$$A_0\left(\xi_i m_i^2\right) = A_0(m_i^2) - \lambda_i m_i^2 \alpha_i\,, \tag{A.10}$$

$$B_0\left(p^2, \xi_{\mathrm{i}} m_{\mathrm{i}}^2, m_{\mathrm{j}}^2\right) = B_0\left(p^2, m_{\mathrm{i}}^2, m_{\mathrm{j}}^2\right) - \lambda_{\mathrm{i}} m_{\mathrm{i}}^2 \beta_{\mathrm{ij}}\left(p^2\right)\,. \tag{A.11}$$

And finally, these non-trivial integrals are also extremely useful

$$\int d^4k \frac{k^2 - 2p\cdot k}{[k^2 - m_i^2][k^2 - \xi_i m_i^2][(q-k)^2 - \xi_i m_i^2]} = \frac{i}{16\pi^2}\Big(\alpha_i - (q^2 - m_i^2)\beta_{i\xi i}\Big)\,, \tag{A.12}$$

$$\begin{aligned} &\int d^4k \frac{1}{[k^2 - m_i^2][k^2 - \xi_i m_i^2][(q-k)^2 - m_i^2][(q-k)^2 - \xi_i m_i^2]} = \\ &= \frac{i}{16\pi^2}\frac{1}{\lambda_i m^2}\Big[\beta_{ii}(q^2) - \beta_{i\xi i}(q^2)\Big]\,, \end{aligned} \tag{A.13}$$

$$\begin{aligned} &\int d^4k \frac{k^2 \pm p\cdot k}{[k^2 - m_i^2][k^2 - \xi_i m_i^2][(q\pm k)^2 - m_i^2][(q\pm k)^2 - \xi_i m_i^2]} = \\ &= \frac{i}{16\pi^2}\frac{1}{\lambda_i m^2}\left[\beta_{ii}(q^2)\Big[m_i^2 - \frac{q^2}{2}\Big] - \beta_{i\xi i}(q^2)\Big[m_i^2\xi_i - \frac{q^2}{2}\Big]\right]. \end{aligned} \tag{A.14}$$

The *pinching* aims at isolate all self-energy like terms. It might be a little overwhelming because there are so many diagrams that can, in principle, contribute. We can considerably narrow the number of diagrams once we realise that, to get the vertices proportional to the momentum we need gauge bosons in the diagrams. In fact, all the contributions come from diagrams with gauge bosons $V = Z, W$ and/or goldstones $S = \eta, G$. We also define F as a placeholder for any fermion that can be in that specific diagram. In the following sections, we explicitly write the contributions of each topology of diagrams to the pinched self-energy. We organized the contribution by square diagrams, triangle diagrams and leg diagrams.

A.1 Squares

$$\Pi^{\text{box,Z}}_{h_ih_j} = \lambda_Z \frac{g^2}{64\pi^2 c_w^2}(q^2 - m_{h_i}^2)(q^2 - m_{h_j}^2)\mathcal{O}_{h_ih_j}\frac{\beta_{ZZ}(q^2) + \beta_{Z\xi Z}(q^2)}{2} \tag{A.15}$$

In the table below I specify the contribution from each diagram separately. The red part of the expression above is the sum over each cell (or the final row *All*) multiplied the function in each column header.

Diagram	**Comments**	$\beta_{ZZ}(q^2)$	$\beta_{Z\xi Z}(q^2)$
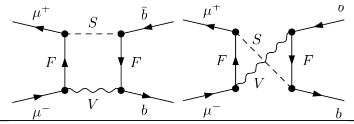		0	$\frac{1}{2}$
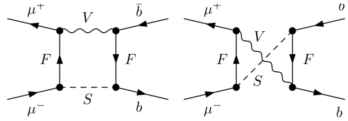		0	$\frac{1}{2}$
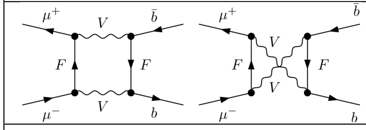		$\frac{1}{2}$	$-\frac{1}{2}$
All		1/2	1/2

Table A.1: Pinch contributions from the square diagrams with Z bosons and η goldstone.

$$\Pi^{\text{box,W}}_{h_ih_j} = \lambda_W \frac{g^2}{32\pi^2}(q^2 - m_{h_i}^2)(q^2 - m_{h_j}^2)\mathcal{O}_{h_ih_j}\frac{\beta_{WW}(q^2) + \beta_{W\xi W}(q^2)}{2} \tag{A.16}$$

Diagram	**Comments**	$\beta_{WW}(q^2)$	$\beta_{W\xi W}(q^2)$
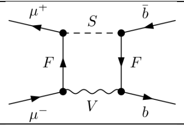		0	$\frac{1}{2}$
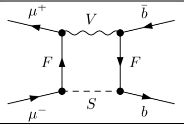		0	$\frac{1}{2}$
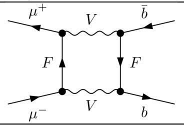		$\frac{1}{2}$	$-\frac{1}{2}$
All		1/2	1/2

Table A.2: Pinch contributions from the square diagrams with W bosons and G goldstone.

A.2 External Legs

There is an additional factor of $\frac{1}{2}$ from the LSZ reduction that has to be taken into account.

$$\Pi^{\text{legs,Z}}_{h_i h_j} = \lambda_Z \frac{-g^2}{128\pi^2 c_w^2}(2q^2 - m_{h_i}^2 - m_{h_j}^2)\mathcal{O}_{h_i h_j}\left[1 + \frac{40}{9}s_w^4 - \frac{8}{3}s_w^2\right]\alpha_Z \tag{A.17}$$

Diagram	**Comments**	α_Z
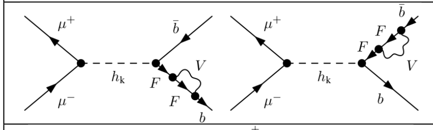 μ^+ μ^- h_k $\bar{b}$ b F V		$\frac{1}{2} + \frac{4}{9}s_w^4 - \frac{4}{6}s_w^2$
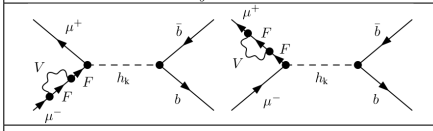 μ^+ μ^- h_k $\bar{b}$ b F V		$\frac{1}{2} + 4s_w^4 - 2s_w^2$
All		$1 + 40/9s_w^4 - 8/3s_w^2$

Table A.3: Pinch contributions from the leg diagrams with Z bosons and η goldstone.

$$\Pi^{\text{legs,W}}_{h_i h_j} = \lambda_W \frac{-g^2}{64\pi^2}(2q^2 - m_{h_i}^2 - m_{h_j}^2)\mathcal{O}_{h_i h_j}\alpha_Z \tag{A.18}$$

Diagram	**Comments**	α_W
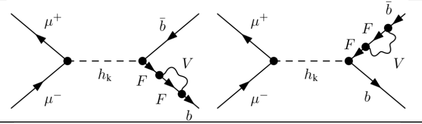 μ^+ μ^- h_k $\bar{b}$ b F V		$\frac{1}{2}$
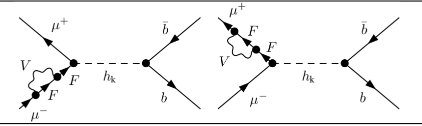 μ^+ μ^- h_k $\bar{b}$ b F V		$\frac{1}{2}$
All		1

Table A.4: Pinch contributions from the leg diagrams with W bosons and G goldstone.

A.3 Triangles

$$\Pi^{\text{tri,Z}}_{h_i h_j} = \lambda_Z \frac{-g^2}{128\pi^2}(2q^2 - m_{h_i}^2 - m_{h_j}^2)\mathcal{O}_{h_i h_j}\left[(q^2 + 2m_Z^2)\beta_{ZZ} + q^2\beta_{Z\xi Z} + \left(-2 - \frac{40}{9}s_w^4 + \frac{8}{3}s_w^4\right)\alpha_W\right] \tag{A.19}$$

Diagram	**Comments**	$\beta_{ZZ}(q^2)$	$\beta_{Z\xi Z}(q^2)$	α_Z
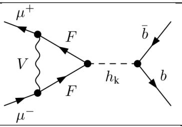		0	0	$-\frac{4}{9}s_w^4+\frac{2}{3}s_w^2$
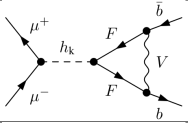		0	0	$-4s_w^4+2s_w^2$
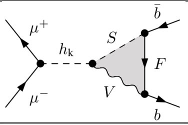	Proportional to λ_Z	0	$2q^2-2\xi_Z m_Z^2$	-2
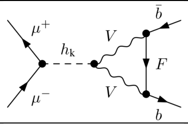	Proportional to λ_Z	$2m_z^2$	0	0
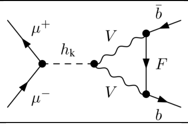	Proportional to λ_Z^2	$\frac{q^2}{2}-m_z^2$	$\xi_Z m_z^2-\frac{q^2}{2}$	0
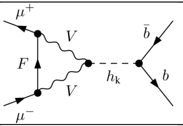	Proportional to λ_Z	$2m_z^2$	0	0
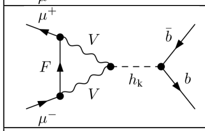	Proportional to λ_Z^2	$\frac{q^2}{2}-m_z^2$	$\xi_Z m_z^2-\frac{q^2}{2}$	0
All		$q^2+2m_Z^2$	q^2	$-2-\frac{40}{9}s_w^4+\frac{8}{3}s_w^4$

Table A.5: Pinch contributions from the triangle diagrams with Z bosons and η goldstone.

Where we compressed all triangles diagrams with V and S in:

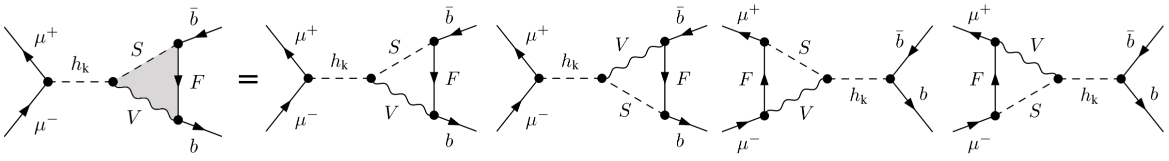

$$\Pi^{\text{tri,W}}_{h_ih_j}=\lambda_W\frac{-g^2}{64\pi^2}(2q^2-m_{h_i}^2-m_{h_j}^2)\mathcal{O}_{h_ih_j}\Big[(q^2+2m_W^2)\beta_{WW}+q^2\beta_{W\xi W}-2\alpha_W\Big] \tag{A.20}$$

Diagram	**Comments**	$\beta_{WW}(q^2)$	$\beta_{W\xi W}(q^2)$	α_W
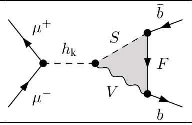	Proportional to λ_W	0	$2q^2 - 2\xi_W m_W^2$	-2
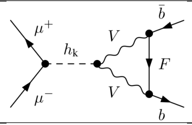	Proportional to λ_W	$q^2/2 - m_W^2$	$\xi_Z m_W^2 - q^2/2$	0
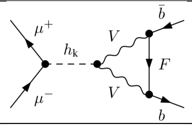	Proportional to λ_W^2	$2m_W^2$	0	0
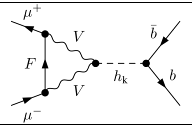	Proportional to λ_W	$q^2/2 - m_W^2$	$\xi_Z m_W^2 - q^2/2$	0
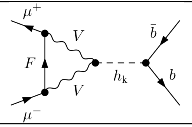	Proportional to λ_W^2	$2m_W^2$	0	0
All		$q^2 + 2m_W^2$	q^2	-2

Table A.6: Pinch contributions from the triangle diagrams with W bosons and G goldstone.

A.4 Additional Diagrams - from $\xi_i = 1$ part of the propagators

These contributions originate from the transformation of B_0 functions with a gauge parameter, multiplied by a mass, as an argument. They come from the following diagrams

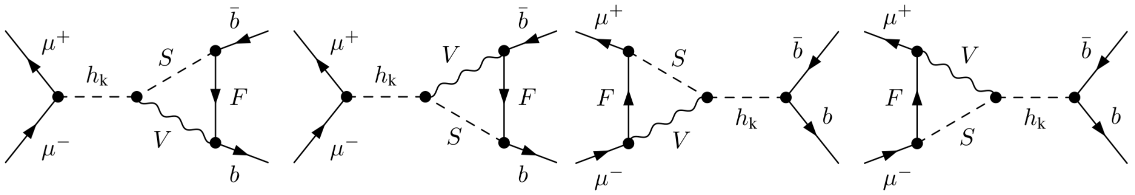

Figure A.2: Triangle diagrams with pinch contributions initially not proportional to λ_i (that can be restored later by the B_0 function).

$$\Pi^{\text{add,Z}}_{h_i h_j} = \lambda_Z \frac{g^2}{128\pi^2 c_w^2}(2q^2 - m_{h_i}^2 - m_{h_j}^2)\mathcal{O}_{h_i h_j} 2m_Z^2 \beta_{ZZ}(q^2)$$
$$+ \frac{-g^2}{32\pi^2 c_w^2}\left(q^2 - \frac{m_{h_i}^2 + m_{h_j}^2}{2}\right)\mathcal{O}_{h_i h_j} B_0(q^2, m_Z^2, m_Z^2)\,, \tag{A.21}$$

$$\begin{aligned}\Pi^{\text{add,W}}_{h_ih_j} &= \lambda_W \frac{g^2}{64\pi^2 c_w^2}(2q^2 - m_{h_i}^2 - m_{h_j}^2)\mathcal{O}_{h_ih_j} 2m_W^2 \beta_{WW}(q^2) + \\ &+ \frac{-g^2}{16\pi^2}\left(q^2 - \frac{m_{h_i}^2+m_{h_j}^2}{2}\right)\mathcal{O}_{h_ih_j} B_0(q^2, m_W^2, m_W^2)\,. \qquad \text{(A.22)}\end{aligned}$$

A.5 Pinched self-energy

Now we can sum over all diagrams such that we get a pinch contribution that has a self-energy like structure. We obtain the following expression

$$\begin{aligned}\Pi^{\text{pinch}}_{h_\mathrm{i}h_\mathrm{j}}\left(p^2\right) =& \Pi^{\text{box,Z}}_{h_\mathrm{i}h_\mathrm{j}}\left(p^2\right) + \Pi^{\text{legs,Z}}_{h_\mathrm{i}h_\mathrm{j}}\left(p^2\right) + \Pi^{\text{tri,Z}}_{h_\mathrm{i}h_\mathrm{j}}\left(p^2\right) + \Pi^{\text{add,Z}}_{h_\mathrm{i}h_\mathrm{j}}\left(p^2\right) \\ &+ \Pi^{\text{box,W}}_{h_\mathrm{i}h_\mathrm{j}}\left(p^2\right) + \Pi^{\text{legs,W}}_{h_\mathrm{i}h_\mathrm{j}}\left(p^2\right) + \Pi^{\text{tri,W}}_{h_\mathrm{i}h_\mathrm{j}}\left(p^2\right) + \Pi^{\text{add,W}}_{h_\mathrm{i}h_\mathrm{j}}\left(p^2\right) \qquad \text{(A.23)} \\ =& -\lambda_Z \frac{g^2\mathcal{O}_{h_ih_j}}{64\pi^2 c_w}\left[\frac{\beta_{Z\xi Z}+\beta_{ZZ}}{2}\left(p^4 - m_{h_i}^2 m_{h_j}^2\right) - \alpha_Z\left(p^2 - \frac{m_{h_i}^2+m_{h_j}^2}{2}\right)\right] \\ &- \lambda_W \frac{g^2\mathcal{O}_{h_ih_j}}{32\pi^2}\left[\frac{\beta_{W\xi W}+\beta_{WW}}{2}\left(p^4 - m_{h_i}^2 m_{h_j}^2\right) - \alpha_W\left(p^2 - \frac{m_{h_i}^2+m_{h_j}^2}{2}\right)\right] \\ &- \frac{g^2}{32\pi^2 c_\mathrm{w}^2}\left(p^2 - \frac{m_{h_\mathrm{i}}^2+m_{h_\mathrm{j}}^2}{2}\right)\mathcal{O}_{h_\mathrm{i}h_\mathrm{j}} B_0\left(q^2; m_\mathrm{Z}^2, m_\mathrm{Z}^2\right) \\ &- \frac{g^2}{16\pi^2}\left(p^2 - \frac{m_{h_\mathrm{i}}^2+m_{h_\mathrm{j}}^2}{2}\right)\mathcal{O}_{h_\mathrm{i}h_\mathrm{j}} B_0\left(p^2; m_\mathrm{W}^2, m_\mathrm{W}^2\right). \qquad \text{(A.24)}\end{aligned}$$

One can see that the pinched terms $\Pi^{\text{pinch}}_{h_\mathrm{i}h_\mathrm{j}}$ precisely cancel the gauge dependency of Eq. A.3. If we use the pinched terms to correct the self-energies we get the:

$$\begin{aligned}\Sigma^{\text{pinch}}_{h_ih_j}(p^2) =& \Sigma^{\text{tad}}_{h_ih_j}(p^2) + \Pi^{\text{pinch}}_{h_\mathrm{i}h_\mathrm{j}}\left(p^2\right) \qquad \text{(A.25)} \\ =& \Sigma_{h_ih_j}(p^2)|_{\xi_i=1} \\ &+ \frac{-g^2}{32\pi^2 c_\mathrm{W}^2}\left(p^2 - \frac{m_{h_\mathrm{i}}^2+m_{h_\mathrm{j}}^2}{2}\right)\mathcal{O}_{h_\mathrm{i}h_\mathrm{j}} B_0\left(q^2, m_\mathrm{Z}^2, m_\mathrm{Z}^2\right) \\ &+ \frac{-g^2}{16\pi^2}\left(p^2 - \frac{m_{h_\mathrm{i}}^2+m_{h_\mathrm{j}}^2}{2}\right)\mathcal{O}_{h_\mathrm{i}h_\mathrm{j}} B_0\left(p^2, m_\mathrm{W}^2, m_\mathrm{W}^2\right)\,. \qquad \text{(A.26)}\end{aligned}$$

which is in fact gauge independent.

Appendix B

Right-Handed Neutrinos

In scenario 2 we added two right-handed neutrinos N_R and S to each fermionic family (in the framework of the CxSM model) to trigger an inverse seesaw mechanism [83] which naturally generates the light left-handed neutrinos present in the SM. In this case the neutrinos ν (from the SM), N_R and S are considered to be Majorana neutrinos, i.e. they are their own anti-particles ($\mathcal{CP}$-conjugates)

$$\psi = \psi^c \equiv -i\gamma^2\psi^* \,. \tag{B.1}$$

In general, for Dirac and Majorana neutrinos we have that

$$(\psi^c)_L = (\psi_R)^c \,, \tag{B.2}$$

$$(\psi^c)_R = (\psi_L)^c \,. \tag{B.3}$$

Then it is straightforward to show that the left(right)-handed neutrino coincide with the right(left)-handed anti neutrinos

$$\psi_R = (\psi_L)^c \equiv \psi_L^c \,, \tag{B.4}$$

$$\psi_L = (\psi_R)^c \equiv \psi_R^c \,. \tag{B.5}$$

Therefore, Majorana neutrinos can be written as

$$\psi = \psi_L + \psi_L^c = \psi_R^c + \psi_R \,. \tag{B.6}$$

Finally, for any neutrino ψ and ϕ we have that

$$\overline{\psi_L}\phi_R = \overline{\phi_R^c}\psi_L^c \,, \tag{B.7}$$

which can be see from

$$\begin{aligned} \overline{\psi_L}\phi_R &= \left(\overline{\psi_L}\phi_R\right)^T = -\phi_R^T\gamma_0^T\psi_L^* \\ &= -\left(\phi_R^*\right)^\dagger\gamma_0\left(-i\gamma_2\right)\left(-i\gamma_2\psi_L^*\right) = \left(-i\gamma_2\phi_R^*\right)^\dagger\gamma_0\left(-i\gamma_2\psi_L^*\right) \\ &= \overline{\phi_R^c}\psi_L^c \,. \end{aligned} \tag{B.8}$$

In scenario 2, we add two right-handed Majorana neutrinos to each fermionic family, see Ref [83] for more details. The new contribution to the Lagrangian of interest to us is

$$\mathcal{L}_{\text{CxSM}} = (...) - Y_h \overline{L_\beta} \tilde{\Phi} N_R - M_\nu \overline{S_R^c} N_R - \frac{1}{2} \tilde{\mu} \overline{S_R^c} S_R \sigma + \text{ h.c.}\,, \tag{B.9}$$

where we implicitly sum over fermionic families. Y_h is a Yukawa-like coupling, $\tilde{\Phi}$ is the Higgs doublet with opposite hypercharge, L_β is the leptonic doublet, just as in Eq. 2.53, M_ν is a parameter with units of mass and $\tilde{\mu}$ is a dimensionless quantity. Both right-handed neutrinos are sterile ($T^3 = Y = 0 \implies Q = 0$). We could also add a Majorana mass term for N_R but that would not change the core of the model because it could be absorbed by redefining $\tilde{\mu}$.

After spontaneous symmetry breaking we have the following mass terms

$$\mathcal{L}_{\text{CxSM}}^{\text{bilinear}} = (...) - Y_h \overline{\nu_L} \frac{v_h}{\sqrt{2}} N_R - M_\nu \overline{S_R^c} N_R - \frac{1}{2} \tilde{\mu} \overline{S_R^c} S_R \frac{v_\sigma}{\sqrt{2}} + \text{ h.c.} \tag{B.10}$$

$$\begin{aligned} &= (...) - \frac{1}{2} \left(m_D \overline{\nu_L} N_R + M_\nu \overline{S_R^c} N_R \right) - \frac{1}{2} \mu \overline{S_R^c} S_R \\ &\quad - \frac{1}{2} \left(m_D \overline{N_R^c} \nu_L^c + M_\nu \overline{N_R^c} S_R \right) + \text{ h.c.}\,, \end{aligned} \tag{B.11}$$

where in the last step we used Eq. B.7 to split the first two terms, with $m_D \equiv Y_h \frac{v_h}{\sqrt{2}}$, $\mu \equiv \tilde{\mu} \frac{v_\sigma}{\sqrt{2}}$ and, for simplicity, we assumed real Yukawa couplings and no mixing between families. We can write the mass terms in a compact way and see that there is a mixing between the two neutrinos

$$\mathcal{L}_{\text{CxSM}}^{\text{bilinear}} = (...) - \frac{1}{2} \begin{pmatrix} \overline{\nu_L} & \overline{N_R^c} & \overline{S_R^c} \end{pmatrix} \begin{pmatrix} 0 & m_D & 0 \\ m_D & 0 & M_\nu \\ 0 & M_\nu & \mu \end{pmatrix} \begin{pmatrix} \nu_L^c \\ N_R \\ S_R \end{pmatrix} + \text{h.c.}\,. \tag{B.12}$$

We expect μ to be very small since the Majorana term violates the leptonic number, $\Delta l = 2$. We also expect the Dirac term to be small since there are upper limits on the SM neutrino masses that only allow for very small masses. For these reasons we impose a strong hierarchy in the mass parameters

$$M_\nu \gg m_D \gg \mu\,. \tag{B.13}$$

The masses of the particles are given by the eigenvalues of the mass matrix. The hierarchy allow us to approximately determine the lightest neutrino mass as

$$m_{\nu_1} \approx \mu \frac{m_D^2}{M_\nu^2}\,, \tag{B.14}$$

which coincides with the SM neutrinos. We also have two Majorana neutrinos with large masses approximately equal to

$$m_{\nu_2} \approx M_\nu + \frac{m_D}{2}\,, \tag{B.15}$$

$$m_{\nu_3} \approx M_\nu - \frac{m_D}{2}\,. \tag{B.16}$$

Appendix C

Smoothing the action

The value of β/H is given by Eq. (5.28). As can be seen from this expression, the calculation involves the derivative of the action with respect to the temperature. A possible method to calculate it numerically is to use the Difference Quotient Method (DQM) with the bounce action numerically computed by `CosmoTransitions` as

$$\frac{\beta}{H} = T_* \, \frac{d}{dT}\left(\frac{\hat{S}_3(T)}{T}\right)\Bigg|_{T_*} \approx T_* \frac{1}{2\cdot\Delta T}\left(\left(\frac{\hat{S}_3(T)}{T}\right)\Bigg|_{T=T_*+\Delta T} - \left(\frac{\hat{S}_3(T)}{T}\right)\Bigg|_{T=T_*-\Delta T}\right) \,, \quad \text{(C.1)}$$

where ΔT is the small step of the DQM. This method correctly calculates β/H for points with a strong GW signal, but for weaker points, numerical errors in the calculation of $\hat{S}_3$ make the DQM not completely reliable. Our solution is to interpolate the action around T_n starting by sampling $N = \{60\,,75\,,90\,,105\}$ bounce actions[1] inside the interval ranging from $\max\{T_n - 30 \text{ GeV}, T_n/2\}$, which should leave enough room to calculate the percolation temperature, up to $T_c - 3$ GeV. We do not interpolate exactly up to T_c to prevent numerical instabilities regarding the existence/location of the minimum. Moreover, for the calculation of the percolation temperature, T_*, this truncation has a negligible effect since the biggest contribution comes from the epoch around T_n. The 4 independent samples of N actions are linearly distributed inside the mentioned interval, in each sample. If we calculate more than 7 bounce actions then a degree 6 polynomial in T can be fitted that models $\hat{S}_3/T$. After this procedure the calculation of the derivative is trivial. Applying this method to four independent samples of points allows us to calculate β/H four times. We consider the most correct value for β/H to be the average between all 4 samples. This allows us to estimate an error $\Delta\left(\beta/H\right)$ for our method which we define as the difference between the biggest β/H and the smallest β/H divided by two,

$$\Delta\left(\beta/H\right) = \frac{\max\{\beta/H\} - \min\{\beta/H\}}{2}\,. \quad \text{(C.2)}$$

---

[1] `CosmoTransitions` is not always able to calculate all of the N bounce actions. When this happens we do the fit with whichever points it managed to calculate.

The next question to ask is: which points will we consider as valid when we use this method on the output of `CosmoTransitions`? In Fig. C.1 we now present a scatter plot with the GW signal $h^2\Omega_{\text{GW}}^{\text{peak}}$ as a function of the peak frequency f^{peak} for three different levels of constraints set upon the uncertainty of β/H. On the left panel, a total of 14390 points are shown which are the ones with no restrictions on $\Delta(\beta/H)$, that is, the original set of points before the smoothing procedure is applied. Once we impose that $\Delta(\beta/H) < 0.25$ (middle panel) the number of points is reduced to 9613 and if we further restrict the error $\Delta(\beta/H) < 0.1$, the number of allowed points is reduced to 3637, that is, less than 26% of the points remain. In the plots presented in the paper, all points have $\Delta(\beta/H) < 0.25$. We did not want to further restrict the error because it could be that we were also losing too many good points.

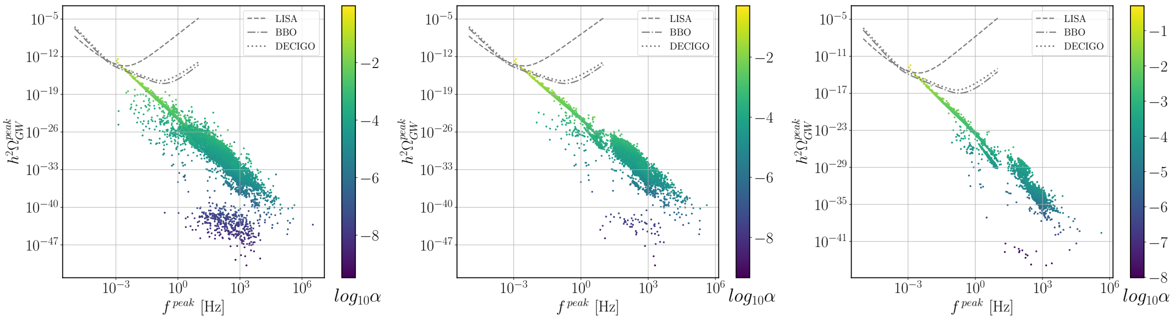

Figure C.1: The peak-amplitude for the GW signal $h^2\Omega_{\text{GW}}^{\text{peak}}$ as a function of the peak frequency f_{peak} in logarithmic scale. The scatter plots present, in the colour bar, the strength of the phase transition α. In the left plot, there are no restrictions related to the calculation of β/H, in the middle plot only points with $\Delta(\beta/H) < 0.25$ are accepted, and in the right panel only points with $\Delta(\beta/H) < 0.1$ are accepted.

Our method has another benefit, the interpolation of the bounce action provides us with an approximate analytical expression for $\hat{S}_3/T$ which, in turn, gives us an approximate analytical expression for the tunnelling rate $\Gamma(T)$. This allows us to calculate the nucleation temperature and percolation temperature with great precision and because we have 4 samples we can also estimate the error associated with our calculation of the characteristic temperatures.

References

[1] B. Aharmim, S. N. Ahmed, A. E. Anthony, E. W. Beier, A. Bellerive, M. Bergevin, S. D. Biller, J. Boger, M. G. Boulay, M. G. Bowler, T. V. Bullard, Y. D. Chan, M. Chen, X. Chen, B. T. Cleveland, G. A. Cox, C. A. Currat, X. Dai, F. Dalnoki-Veress, H. Deng, P. J. Doe, R. S. Dosanjh, G. Doucas, C. A. Duba, F. A. Duncan, M. Dunford, J. A. Dunmore, E. D. Earle, S. R. Elliott, H. C. Evans, G. T. Ewan, J. Farine, H. Fergani, F. Fleurot, J. A. Formaggio, K. Frame, W. Frati, B. G. Fulsom, N. Gagnon, K. Graham, D. R. Grant, R. L. Hahn, J. C. Hall, A. L. Hallin, E. D. Hallman, W. B. Handler, C. K. Hargrove, P. J. Harvey, R. Hazama, K. M. Heeger, L. Heelan, W. J. Heintzelman, J. Heise, R. L. Helmer, R. J. Hemingway, A. Hime, C. Howard, M. A. Howe, M. Huang, P. Jagam, N. A. Jelley, J. R. Klein, L. L. Kormos, M. S. Kos, A. Krüger, C. Kraus, C. B. Krauss, A. V. Krumins, T. Kutter, C. C. M. Kyba, H. Labranche, R. Lange, J. Law, I. T. Lawson, K. T. Lesko, J. R. Leslie, I. Levine, J. C. Loach, S. Luoma, R. MacLellan, S. Majerus, H. B. Mak, J. Maneira, A. D. Marino, N. McCauley, A. B. McDonald, S. McGee, G. McGregor, C. Mifflin, K. K. S. Miknaitis, B. A. Moffat, C. W. Nally, M. S. Neubauer, B. G. Nickel, A. J. Noble, E. B. Norman, N. S. Oblath, C. E. Okada, R. W. Ollerhead, J. L. Orrell, S. M. Oser, C. Ouellet, S. J. M. Peeters, A. W. P. Poon, K. Rielage, B. C. Robertson, R. G. H. Robertson, E. Rollin, S. S. E. Rosendahl, V. L. Rusu, M. H. Schwendener, S. R. Seibert, O. Simard, J. J. Simpson, C. J. Sims, D. Sinclair, P. Skensved, M. W. E. Smith, N. Starinsky, R. G. Stokstad, L. C. Stonehill, R. Tafirout, Y. Takeuchi, G. Tešić, M. Thomson, M. Thorman, T. Tsui, R. Van Berg, R. G. Van de Water, C. J. Virtue, B. L. Wall, D. Waller, C. E. Waltham, H. Wan Chan Tseung, D. L. Wark, J. Wendland, N. West, J. F. Wilkerson, J. R. Wilson, P. Wittich, J. M. Wouters, A. Wright, M. Yeh, and K. Zuber. Electron energy spectra, fluxes, and day-night asymmetries of ^{8}b solar neutrinos from measurements with nacl dissolved in the heavy-water detector at the sudbury neutrino observatory. *Phys. Rev. C*, 72:055502, Nov 2005. 1

[2] S. Abe, T. Ebihara, S. Enomoto, K. Furuno, Y. Gando, K. Ichimura, H. Ikeda, K. Inoue, Y. Kibe, Y. Kishimoto, M. Koga, A. Kozlov, Y. Minekawa, T. Mitsui, K. Nakajima, K. Nakajima, K. Nakamura, M. Nakamura, K. Owada, I. Shimizu, Y. Shimizu, J. Shirai, F. Suekane, A. Suzuki, Y. Takemoto, K. Tamae, A. Terashima, H. Watanabe, E. Yonezawa, S. Yoshida, J. Busenitz, T. Classen, C. Grant, G. Keefer, D. S. Leonard, D. McKee, A. Piepke, M. P. Decowski, J. A. Detwiler, S. J. Freedman, B. K. Fujikawa, F. Gray, E. Guardincerri, L. Hsu, R. Kadel, C. Lendvai, K.-B. Luk,

H. Murayama, T. O'Donnell, H. M. Steiner, L. A. Winslow, D. A. Dwyer, C. Jillings, C. Mauger, R. D. McKeown, P. Vogel, C. Zhang, B. E. Berger, C. E. Lane, J. Maricic, T. Miletic, M. Batygov, J. G. Learned, S. Matsuno, S. Pakvasa, J. Foster, G. A. Horton-Smith, A. Tang, S. Dazeley, K. E. Downum, G. Gratta, K. Tolich, W. Bugg, Y. Efremenko, Y. Kamyshkov, O. Perevozchikov, H. J. Karwowski, D. M. Markoff, W. Tornow, K. M. Heeger, F. Piquemal, and J.-S. Ricol. Precision measurement of neutrino oscillation parameters with kamland. *Phys. Rev. Lett.*, 100:221803, Jun 2008. 1

[3] P.A. Zyla et al. Review of Particle Physics. *PTEP*, 2020(8):083C01, 2020. 1, 4, 39, 47, 59

[4] A. D. Sakharov. Violation of CP Invariance, C asymmetry, and baryon asymmetry of the universe. *Pisma Zh. Eksp. Teor. Fiz.*, 5:32–35, 1967. 1, 2, 47

[5] F. Csikor, Z. Fodor, and J. Heitger. End point of the hot electroweak phase transition. *Physical Review Letters*, 82(1):21–24, Jan 1999. 1, 47

[6] F. Zwicky. Die Rotverschiebung von extragalaktischen Nebeln. *Helv. Phys. Acta*, 6:110–127, 1933. 1

[7] A V Zasov, A S Saburova, A V Khoperskov, and S A Khoperskov. Dark matter in galaxies. *Physics-Uspekhi*, 60(1):3–39, Jan 2017. 1, 3

[8] Douglas Clowe, Maruša Bradač, Anthony H. Gonzalez, Maxim Markevitch, Scott W. Randall, Christine Jones, and Dennis Zaritsky. A direct empirical proof of the existence of dark matter. *The Astrophysical Journal*, 648(2):L109–L113, Aug 2006. 1

[9] Virginia Trimble. Existence and Nature of Dark Matter in the Universe. *Ann. Rev. Astron. Astrophys.*, 25:425–472, 1987. 1

[10] Pau Amaro-Seoane et al. Laser Interferometer Space Antenna. 2017. 2, 47

[11] Seiji Kawamura, Masaki Ando, Naoki Seto, Shuichi Sato, Mitsuru Musha, Isao Kawano, Jun'ichi Yokoyama, Takahiro Tanaka, Kunihito Ioka, Tomotada Akutsu, Takeshi Takashima, Kazuhiro Agatsuma, Akito Araya, Naoki Aritomi, Hideki Asada, Takeshi Chiba, Satoshi Eguchi, Motohiro Enoki, Masa-Katsu Fujimoto, Ryuichi Fujita, Toshifumi Futamase, Tomohiro Harada, Kazuhiro Hayama, Yoshiaki Himemoto, Takashi Hiramatsu, Feng-Lei Hong, Mizuhiko Hosokawa, Kiyotomo Ichiki, Satoshi Ikari, Hideki Ishihara, Tomohiro Ishikawa, Yousuke Itoh, Takahiro Ito, Shoki Iwaguchi, Kiwamu Izumi, Nobuyuki Kanda, Shinya Kanemura, Fumiko Kawazoe, Shiho Kobayashi, Kazunori Kohri, Yasufumi Kojima, Keiko Kokeyama, Kei Kotake, Sachiko Kuroyanagi, Kei ichi Maeda, Shuhei Matsushita, Yuta Michimura, Taigen Morimoto, Shinji Mukohyama, Koji Nagano, Shigeo Nagano, Takeo Naito, Kouji Nakamura, Takashi Nakamura, Hiroyuki Nakano, Kenichi Nakao, Shinichi Nakasuka, Yoshinori Nakayama, Kazuhiro Nakazawa, Atsushi Nishizawa,

Masashi Ohkawa, Kenichi Oohara, Norichika Sago, Motoyuki Saijo, Masaaki Sakagami, Shin ichiro Sakai, Takashi Sato, Masaru Shibata, Hisaaki Shinkai, Ayaka Shoda, Kentaro Somiya, Hajime Sotani, Ryutaro Takahashi, Hirotaka Takahashi, Takamori Akiteru, Keisuke Taniguchi, Atsushi Taruya, Kimio Tsubono, Shinji Tsujikawa, Akitoshi Ueda, Ken ichi Ueda, Izumi Watanabe, Kent Yagi, Rika Yamada, Shuichiro Yokoyama, Chul-Moon Yoo, and Zong-Hong Zhu. Current status of space gravitational wave antenna decigo and b-decigo, 2020. 2

[12] Jeff Crowder and Neil J. Cornish. Beyond lisa: Exploring future gravitational wave missions. *Phys. Rev. D*, 72:083005, Oct 2005. 2

[13] John F. Gunion, Howard E. Haber, Gordon L. Kane, and Sally Dawson. *The Higgs Hunter's Guide*, volume 80. 2000. 3

[14] Rita Coimbra, Marco O. P. Sampaio, and Rui Santos. ScannerS: Constraining the phase diagram of a complex scalar singlet at the LHC. *Eur. Phys. J. C*, 73:2428, 2013. 5, 15

[15] Margarete Mühlleitner, Marco O. P. Sampaio, Rui Santos, and Jonas Wittbrodt. Scanners: Parameter scans in extended scalar sectors, 2020. 5, 15

[16] M. Thomson. *Modern Particle Physics*. Modern Particle Physics. Cambridge University Press, 2013. 6, 10, 11, 18

[17] Michael E. Peskin and Daniel V. Schroeder. *An Introduction to quantum field theory*. Addison-Wesley, Reading, USA, 1995. 8, 19, 20, 24, 69

[18] Matthew D. Schwartz. *Quantum Field Theory and the Standard Model*. Cambridge University Press, 3 2014. 12, 24

[19] L.D. Faddeev and V.N. Popov. Feynman diagrams for the yang-mills field. *Physics Letters B*, 25(1):29–30, 1967. 12

[20] Jorge C. Romao and Joao P. Silva. A resource for signs and feynman diagrams of the standard model, 2012. 13

[21] N. Aghanim, Y. Akrami, F. Arroja, M. Ashdown, J. Aumont, C. Baccigalupi, M. Ballardini, A. J. Banday, R. B. Barreiro, and et al. Planck2018 results. *Astronomy & Astrophysics*, 641:A1, Sep 2020. 15

[22] E. Aprile, J. Aalbers, F. Agostini, M. Alfonsi, L. Althueser, F. D. Amaro, M. Anthony, F. Arneodo, L. Baudis, B. Bauermeister, and et al. Dark matter search results from a one ton-year exposure of xenon1t. *Physical Review Letters*, 121(11), Sep 2018. 15

[23] Combination of searches for invisible Higgs boson decays with the ATLAS experiment. 10 2020. 15

[24] P. Bechtle, O. Brein, S. Heinemeyer, G. Weiglein, and K.E. Williams. Higgsbounds: Confronting arbitrary higgs sectors with exclusion bounds from lep and the tevatron. *Computer Physics Communications*, 181(1):138–167, Jan 2010. 15

[25] Philip Bechtle, Sven Heinemeyer, Oscar Stål, Tim Stefaniak, and Georg Weiglein. Higgssignals: Confronting arbitrary higgs sectors with measurements at the tevatron and the lhc. *The European Physical Journal C*, 74(2), Feb 2014. 15

[26] G. Bélanger, F. Boudjema, A. Goudelis, A. Pukhov, and B. Zaldívar. micromegas5.0 : Freeze-in. *Computer Physics Communications*, 231:173–186, Oct 2018. 15

[27] Wolfram Research, Inc. Mathematica, Version 12.3.1, 2021. Champaign, IL, 2021. 15

[28] Adam Alloul, Neil D. Christensen, Céline Degrande, Claude Duhr, and Benjamin Fuks. Feynrules 2.0 — a complete toolbox for tree-level phenomenology. *Computer Physics Communications*, 185(8):2250–2300, Aug 2014. 15

[29] Thomas Hahn. Generating Feynman diagrams and amplitudes with FeynArts 3. *Computer Physics Communications*, 140(3):418–431, Nov 2001. 15

[30] Vladyslav Shtabovenko, Rolf Mertig, and Frederik Orellana. New developments in FeynCalc 9.0. *Computer Physics Communications*, 207:432–444, Oct 2016. 16

[31] G. Passarino and M. J. G. Veltman. One Loop Corrections for e+ e- Annihilation Into mu+ mu- in the Weinberg Model. *Nucl. Phys. B*, 160:151–207, 1979. 16, 20

[32] G. J. van Oldenborgh and J. A. M. Vermaseren. New Algorithms for One Loop Integrals. *Z. Phys. C*, 46:425–438, 1990. 16

[33] T. Hahn and M. Perez-Victoria. Automatized one loop calculations in four-dimensions and D-dimensions. *Comput. Phys. Commun.*, 118:153–165, 1999. 16

[34] Jorge Crispim Romão. Advanced Quantum Field Theory, 9 2020. 20

[35] J. Fleischer and F. Jegerlehner. Radiative corrections to higgs-boson decays in the weinberg-salam model. *Phys. Rev. D*, 23:2001–2026, May 1981. 26

[36] Duarte Fontes. Multi-higgs models: model building, phenomenology and renormalization, 2021. 26

[37] Shinya Kanemura, Yasuhiro Okada, Eibun Senaha, and C.-P. Yuan. Higgs coupling constants as a probe of new physics. *Physical Review D*, 70(11), Dec 2004. 32

[38] Daniele Binosi and Joannis Papavassiliou. Pinch technique: Theory and applications. *Physics Reports*, 479(1-6):1–152, Aug 2009. 34, 67

[39] J. R. Espinosa and Y. Yamada. Scale- and gauge-independent mixing angles for scalar particles. *Physical Review D*, 67(3), Feb 2003. 34

[40] Duarte Azevedo, Pedro Gabriel, Margarete Muhlleitner, Kodai Sakurai, and Rui Santos. One-loop corrections to the Higgs boson invisible decay in the dark doublet phase of the N2HDM. *JHEP*, 10:044, 2021. 36

[41] Nicola Cabibbo. Unitary Symmetry and Leptonic Decays. 10(12):531–533, June 1963. 47

[42] Makoto Kobayashi and Toshihide Maskawa. CP-Violation in the Renormalizable Theory of Weak Interaction. *Progress of Theoretical Physics*, 49(2):652–657, 02 1973. 47

[43] J. H. Christenson, J. W. Cronin, V. L. Fitch, and R. Turlay. Evidence for the 2π decay of the k_2^0 meson. *Phys. Rev. Lett.*, 13:138–140, Jul 1964. 47

[44] Jose Ramon Espinosa and Mariano Quiros. Novel Effects in Electroweak Breaking from a Hidden Sector. *Phys. Rev. D*, 76:076004, 2007. 47

[45] P. Basler, M. Krause, M. Muhlleitner, J. Wittbrodt, and A. Wlotzka. Strong First Order Electroweak Phase Transition in the CP-Conserving 2HDM Revisited. *JHEP*, 02:121, 2017. 47, 50

[46] A. Ashoorioon and T. Konstandin. Strong electroweak phase transitions without collider traces. *JHEP*, 07:086, 2009. 47

[47] Mariano Quiros. Finite temperature field theory and phase transitions. In *ICTP Summer School in High-Energy Physics and Cosmology*, 1 1999. 48, 50

[48] Sidney R. Coleman. The Fate of the False Vacuum. 1. Semiclassical Theory. *Phys. Rev.*, D15:2929–2936, 1977. [Erratum: Phys. Rev.D16,1248(1977)]. 48, 52

[49] A.D. Linde. Decay of the false vacuum at finite temperature. *Nuclear Physics B*, 216(2):421 – 445, 1983. 48, 52

[50] Chiara Caprini et al. Detecting gravitational waves from cosmological phase transitions with LISA: an update. *JCAP*, 2003(03):024, 2020. 48, 53, 54, 55, 63, 64

[51] Andrea Addazi, Antonino Marcianò, António P. Morais, Roman Pasechnik, Rahul Srivastava, and José W.F. Valle. Gravitational footprints of massive neutrinos and lepton number breaking. *Phys. Lett. B*, 807:135577, 2020. 48, 65

[52] Carroll L. Wainwright. Cosmotransitions: Computing cosmological phase transition temperatures and bubble profiles with multiple fields. *Computer Physics Communications*, 183(9):2006–2013, Sep 2012. 48, 55

[53] José Eliel Camargo-Molina, António P. Morais, Roman Pasechnik, Marco O. P. Sampaio, and Jonas Wessén. All one-loop scalar vertices in the effective potential approach. *JHEP*, 08:073, 2016. 50

[54] L. Dolan and R. Jackiw. Symmetry Behavior at Finite Temperature. *Phys. Rev.*, D9:3320–3341, 1974. 51

[55] Rajesh R. Parwani. Resummation in a hot scalar field theory. *Phys. Rev. D*, 45:4695, 1992. [Erratum: Phys.Rev.D 48, 5965 (1993)]. 51

[56] Peter Brockway Arnold and Olivier Espinosa. The Effective potential and first order phase transitions: Beyond leading-order. *Phys. Rev. D*, 47:3546, 1993. [Erratum: Phys.Rev.D 50, 6662 (1994)]. 51

[57] J. R. Espinosa and M. Quiros. Improved metastability bounds on the standard model Higgs mass. *Phys. Lett. B*, 353:257–266, 1995. 51

[58] John Ellis, Marek Lewicki, and José Miguel No. On the Maximal Strength of a First-Order Electroweak Phase Transition and its Gravitational Wave Signal. *JCAP*, 04:003, 2019. 52, 53, 64

[59] John Ellis, Marek Lewicki, and Ville Vaskonen. Updated predictions for gravitational waves produced in a strongly supercooled phase transition. *Journal of Cosmology and Astroparticle Physics*, 2020(11):020–020, Nov 2020. 52, 53

[60] Xiao Wang, Fa Peng Huang, and Xinmin Zhang. Phase transition dynamics and gravitational wave spectra of strong first-order phase transition in supercooled universe. *Journal of Cosmology and Astroparticle Physics*, 2020(05):045–045, May 2020. 52

[61] Mark Hindmarsh, Stephan J. Huber, Kari Rummukainen, and David J. Weir. Numerical simulations of acoustically generated gravitational waves at a first order phase transition. *Phys. Rev.*, D92(12):123009, 2015. 53

[62] Mark Hindmarsh, Stephan J. Huber, Kari Rummukainen, and David J. Weir. Shape of the acoustic gravitational wave power spectrum from a first order phase transition. *Phys. Rev. D*, 96(10):103520, 2017. [Erratum: Phys.Rev.D 101, 089902 (2020)]. 53, 54, 64

[63] Christophe Grojean and Geraldine Servant. Gravitational Waves from Phase Transitions at the Electroweak Scale and Beyond. *Phys. Rev.*, D75:043507, 2007. 53, 54

[64] Leonardo Leitao and Ariel Megevand. Gravitational waves from a very strong electroweak phase transition. *JCAP*, 1605(05):037, 2016. 53, 54

[65] Chiara Caprini et al. Science with the space-based interferometer eLISA. II: Gravitational waves from cosmological phase transitions. *JCAP*, 1604(04):001, 2016. 53

[66] John Ellis, Marek Lewicki, José Miguel No, and Ville Vaskonen. Gravitational wave energy budget in strongly supercooled phase transitions. *JCAP*, 1906(06):024, 2019. 54

[67] Chiara Caprini and Ruth Durrer. Gravitational wave production: A Strong constraint on primordial magnetic fields. *Phys. Rev. D*, 65:023517, 2001. 54

[68] Daniel G. Figueroa, Mark Hindmarsh, and Jon Urrestilla. Exact Scale-Invariant Background of Gravitational Waves from Cosmic Defects. *Phys. Rev. Lett.*, 110(10):101302, 2013. 54

[69] Mark Hindmarsh. Sound shell model for acoustic gravitational wave production at a first-order phase transition in the early Universe. *Phys. Rev. Lett.*, 120(7):071301, 2018. 54

[70] Jose R. Espinosa, Thomas Konstandin, Jose M. No, and Geraldine Servant. Energy Budget of Cosmological First-order Phase Transitions. *JCAP*, 1006:028, 2010. 55

[71] Glauber C. Dorsch, Stephan J. Huber, and Thomas Konstandin. Bubble wall velocities in the Standard Model and beyond. *JCAP*, 12:034, 2018. 55

[72] Guy D. Moore and Tomislav Prokopec. Bubble wall velocity in a first order electroweak phase transition. *Phys. Rev. Lett.*, 75:777–780, 1995. 55

[73] Thibault Vieu, António P. Morais, and Roman Pasechnik. Multi-peaked signatures of primordial gravitational waves from multi-step electroweak phase transition. 2018. 55

[74] António P. Morais and Roman Pasechnik. Probing multi-step electroweak phase transition with multi-peaked primordial gravitational waves spectra. 2019. 55

[75] Admir Greljo, Toby Opferkuch, and Ben A. Stefanek. Gravitational Imprints of Flavor Hierarchies. *Phys. Rev. Lett.*, 124(17):171802, 2020. 55

[76] Mayumi Aoki, Takatoshi Komatsu, and Hiroto Shibuya. Possibility of multi-step electroweak phase transition in the two Higgs doublet models. 6 2021. 55

[77] Kai Schmitz. New Sensitivity Curves for Gravitational-Wave Signals from Cosmological Phase Transitions. *JHEP*, 01:097, 2021. 55

[78] Chiara Caprini, Ruth Durrer, and Geraldine Servant. The stochastic gravitational wave background from turbulence and magnetic fields generated by a first-order phase transition. *JCAP*, 0912:024, 2009. 64

[79] Arthur Kosowsky, Andrew Mack, and Tinatin Kahniashvili. Gravitational radiation from cosmological turbulence. *Phys. Rev. D*, 66:024030, 2002. 64

[80] Grigol Gogoberidze, Tina Kahniashvili, and Arthur Kosowsky. The Spectrum of Gravitational Radiation from Primordial Turbulence. *Phys. Rev. D*, 76:083002, 2007. 64

[81] Peter Niksa, Martin Schlederer, and Günter Sigl. Gravitational Waves produced by Compressible MHD Turbulence from Cosmological Phase Transitions. *Class. Quant. Grav.*, 35(14):144001, 2018. 64

[82] Pasquale Di Bari, Danny Marfatia, and Ye-Ling Zhou. Gravitational waves from first-order phase transitions in Majoron models of neutrino mass. 5 2021. 65

[83] R. N. Mohapatra and J. W. F. Valle. Neutrino mass and baryon-number nonconservation in superstring models. *Phys. Rev. D*, 34:1642–1645, Sep 1986. 77, 78